



---

# Analogue Binaries and Superradiance

---

*Author:*  
Diogo C. Ribeiro

*Supervisor:*  
Vitor Cardoso  
Miguel Zilhão

*Research work performed at*

CENTRA

*to obtain a Master of Science Degree in*

**Engineering Physics**

## **Examination Committee**

Chairperson: Ilídio Lopes  
Supervisor: Miguel Zilhão  
Member of the Committee: Richard Brito

**April 2022**



*"E as pessoas nem sonham que quem acaba uma coisa  
nunca é aquele que a começou,  
mesmo que ambos tenham um nome igual,  
que isso só é que se mantém constante,  
nada mais."*

José Saramago em *O ano da morte de Ricardo Reis*



## Acknowledgments

I have to begin by expressing my gratitude to my supervisors, Miguel and Vitor for their guidance and patience. I couldn't have asked for better mentors. Besides the joy of discussing physics, you have given me invaluable advice on my career and I cannot thank you enough for that.

Over the course of this work I was warmly welcomed in the gravity group (GRIT) of the Center for Astrophysics and Gravitation (CENTRA) in Instituto Superior Técnico. The thrill of being part of such a lively community has pushed me to give my best everyday. You truly are the coolest group.

This thesis bears the mark of my time at MEFT. Besides being the very basis of my academic training, the last 5 years have been an important personal journey. Over the course of these years, I have crossed paths with numerous brilliant people that, in one way or another, have left their mark on me. I have to specially thank a handful of them. I dedicate this thesis to you.

To the Physics student club (NFIST) and the Astronomy Section (ASTRO); the countless stories and episodes will forever stay with me and remind me of the importance of spreading the love for science. Sharing the passion for something usually leads to lasting friendships.

To the friends that came and went, to the ones that stayed; To those that closely shared these last few months, Tomás Cabrito, André Cordeiro, Mariana Silva, Rita Braga, Pedro Cosme, Tânia Machado, Bernardo Barbosa, Thomas Gaehtgens, Francisco Vazão, Francisco Duque – You are part of this thesis work.

To Ricardo Florentino and his wit. You know me too well! I guard our friendship dearly and cherish our countless adventures. Many are still to come. I'll see you in Japan.

To Hugo Terças. As a professor and friend, you have inspired me seek my own path and changed the way I look at science. I owe you a lot.

Last but not least, to my parents and brother; all of this journey would not be possible without your unconditional support. You made me who I am today. I love you dearly.



## Resumo

A natureza difusa de matéria bosônica ultraleve e o seu fraco acoplamento ao modelo standard torna o seu estudo possível quase exclusivamente através dos seus efeitos gravitacionais.

A descoberta do fenómeno da Superradiância em torno de buracos negros faz deles os laboratórios ideais para estudar as propriedades destes possíveis constituintes da Matéria negra.

O fenómeno da superradiância, análogo ao famoso processo de Penrose para ondas, permite que campos escalares extraiam energia rotacional de buracos negros, abrindo a sua rotação, e assim deixando marcas observacionais claras que permitem colocar limites na massa de tais campos.

A superradiância em torno buracos negros tem vindo a ser alvo de extensos estudos na última década. Contrasta esse com o estudo de campos escalares em sistemas binários de buracos negros, onde o nosso conhecimento fica ainda a desejar. O crescente número de detecções de ondas gravitacionais provenientes de sistemas binários de objectos compactos e o desenvolvimento da nova geração de detectores torna imprescindível perceber como podem estes campos escalares moldar evolução e dinâmica de tais sistemas.

Ao preservar as principais características de tais sistemas astrofísicos, o estudo de modelos-análogos oferece-nos uma via para melhor entender a sua dinâmica. Através de resultados quantitativos e qualitativos o estudo de tais modelos permite também perceber como novos dados experimentais podem ser utilizados para entender a natureza e desvendar as propriedades destes campos.

### **Palavras-chave:**

Superradiância; Buracos Negros ; Sistemas binários;  
Campos escalares ultraleves;



## Abstract

The fuzzy nature of ultralight bosonic fields and their weak coupling to the Standard Model makes it extremely hard to probe their properties if not through gravity. The discovery of Superradiance around black holes makes them, with their extreme gravitational fields, the perfect lab to probe the nature of such Dark Matter candidates.

Superradiance, the wave-like analogue of the famous Penrose process, allows a scalar wave (e.g. a bosonic field) to extract rotational energy from a black hole, leaving clear observational signatures that allow the placement of constraints on the mass of such ultralight fields.

Superradiance in black hole spacetimes has been extensively studied over the last decade. By contrast, the dynamics of scalar fields in black holes binary systems has yet a long way to be fully understood. The increasing number of detected gravitational waves from compact object mergers and the development of next generation detectors makes it important to understand how exactly such ultralight fields can shape the dynamics of these binaries.

By retaining the most fundamental aspects behind such astrophysical systems, the study of toy models can give us both qualitative and quantitative results towards a complete understanding of these dynamics and how upcoming data can be better used to probe its fundamental nature and properties.

**Keywords:** Superradiance; Black Holes ; Binary Systems;  
Ultralight scalar fields;



# Contents

Acknowledgments . . . . .	v
Resumo . . . . .	vii
Abstract . . . . .	ix
List of Tables . . . . .	xiii
List of Figures . . . . .	xv
Glossary . . . . .	xxi
<b>1 Introduction</b>	<b>1</b>
<b>2 Superradiance in Curved Spacetimes</b>	<b>7</b>
2.1 General Relativity . . . . .	7
2.1.1 Curved Spaces . . . . .	7
2.1.2 Einstein's Happiest Thought . . . . .	10
2.1.3 Geometrodynamics . . . . .	10
2.2 Energy Extraction and Superradiance . . . . .	12
2.3 Scalar fields in Spacetime . . . . .	13
2.4 The Black hole bomb . . . . .	14
2.4.1 Scattering Amplitudes . . . . .	15
2.4.2 Cavity Modes . . . . .	17
2.4.3 Why Cavities? . . . . .	18
2.5 Binary systems . . . . .	20
<b>3 Toy Model I</b>	<b>21</b>
3.1 The Fluid-GR Analogy . . . . .	21
3.1.1 Fluid Dynamics . . . . .	21
3.1.2 Linear Perturbation Theory . . . . .	22
3.2 A fluid analogue of a binary . . . . .	23
3.2.1 Cylindrical cavity waves . . . . .	25
3.2.2 Boundary Conditions . . . . .	26
3.2.3 Rotating cylinder . . . . .	27
3.3 Uniform Cylinder . . . . .	27
3.3.1 Superradiant scattering is implied . . . . .	28
3.3.2 Scattering factors . . . . .	28
3.3.3 The Acoustic Bomb . . . . .	32

3.4	Non-Uniform Cylinder . . . . .	36
3.4.1	Scattering factors . . . . .	36
3.5	A Numerical approach . . . . .	39
3.5.1	Scattering amplifications for a static cylinder . . . . .	40
3.5.2	Static cylinder inside a cavity . . . . .	41
3.5.3	Rotating cylinder inside a cavity . . . . .	41
3.6	Superradiance in Laboratory . . . . .	42
<b>4</b>	<b>Toy Model II</b>	<b>45</b>
4.1	Modelling absorption in KG equation . . . . .	45
4.2	Problem Setup . . . . .	47
4.3	Isolated objects: scattering and superradiance . . . . .	49
4.3.1	Scattering amplitudes . . . . .	50
4.3.2	Cavity modes . . . . .	51
4.3.3	Numerical Comparison . . . . .	57
4.4	Binaries and cavity resonances . . . . .	59
4.5	Application to black hole physics . . . . .	65
4.6	Outlook and future work . . . . .	67
<b>5</b>	<b>Conclusions</b>	<b>71</b>
<b>A</b>	<b>Mathematica Notebooks</b>	<b>79</b>
<b>B</b>	<b>Bessel and Hankel Functions</b>	<b>81</b>
B.1	Power series solution . . . . .	81
B.2	Transformed Bessel equation . . . . .	82
B.3	Hankel functions . . . . .	83
B.4	Recurrence relation . . . . .	84
<b>C</b>	<b>Numerical Methods and Convergence</b>	<b>85</b>
C.1	The Method of Lines . . . . .	85
C.2	The wave equation . . . . .	87
C.2.1	Impedance Cylinder Model . . . . .	88
C.2.2	Absorption model . . . . .	88
C.3	Convergence analysis . . . . .	89
<b>D</b>	<b>The Toy Model Connection</b>	<b>91</b>
<b>E</b>	<b>Absorbing sphere inside cavity</b>	<b>93</b>
E.1	Spherical wave equation . . . . .	93
E.2	Adding dissipation . . . . .	94
E.3	Cavity eigenfrequencies . . . . .	95
E.4	Scattering Problem . . . . .	95

# List of Tables

3.1	Parameters used for the initial pulse configuration (3.57). . . . .	40
4.1	Initial conditions considered for the gaussian pulse (4.11). For the single rotating absorbing region we always used the same initial conditions (model SA). For the binary scenario we considered two sets of parameters whose main difference is the azimuthal mode $m$ (models BA). . . . .	49
4.2	First few roots of the Bessel function of the first kind $J_m(x)$ . . . . .	53
4.3	Comparison of the $m = 2$ eigenfrequencies for the BA and SA models (with $R_a = 4$ for the latter, intended to describe astrophysical systems with the same total mass) inside a cavity of size $R_c = 57$ , rotating with the same angular speed $\Omega$ . For the binary, $\Omega$ corresponds to $R_0 = 7.15$ . The BA eigenfrequency was obtained numerically while the SA is obtained analytically by solving (3.39). . . . .	61
4.4	The $m = 1$ eigenfrequencies, extracted from late time Fourier analysis for $R_c = 95$ . Compare the real part of the frequencies with the first two cavity eigenfrequencies $j_{1,0}/R_c = 0.040333$ and $j_{1,1}/R_c = 0.738483$ . Note that $R_0 = 7.1, 8.44$ excite the same cavity mode with $j_{1,0}/R_c = 0.040333$ . . . . .	64



# List of Figures

2.1	Imaginary part of the eigenfrequencies of the field as a function of the cavity radius $R_c$ for several values of the rotation parameter $a$ and several field quantum numbers. The left plot corresponds to the $l = m = 1$ while the one on the right to $l = m = 2$ . Each solid line corresponds to a different cavity radial mode ( $n = 1, 2, 3, \dots$ ). Note that for each $n$ there exists a minimal cavity radius for which the mode can be amplified. . . . .	19
3.1	Cartoon of a cylinder made of a non homogeneous material. The dotted area on the surface depicts the magnitude of the impedance $Z$ , which varies with azimuthal angle according to (3.14). The asymmetry mimics that of a binary system. . . . .	24
3.2	Amplification factor (3.36) the two azimuthal modes $m = 1$ (left column) and $m = 2$ (right column) for several rotation speeds and a cylinder impedance $Z = 1 + 0i$ (top row) and $Z = 1 - 1i$ (bottom row). The lack of an imaginary part suppresses the amplification peak (top row). . . . .	29
3.3	Absorption curves (3.40) for several azimuthal modes $m$ . The parametrization path starts at the origin with $\omega = 0$ and ends at $Z = 1 + 0i$ when $\omega \rightarrow \infty$ . . . . .	31
3.4	Absorption and amplification curves (3.40) and (3.41), respectively, for the $m = 2$ azimuthal mode and several rotation speeds. The solid lines correspond to the absorption curves while the dashed lines to amplification ones. For a description of how these curves are parametrized see the main text. . . . .	32
3.5	Acoustic bomb eigenfrequency (3.45) evolution in the complex plane as the rotation of the inner cylinder is increased for the azimuthal mode $m = 1$ . The cylinder has radius $R_i = 1$ and purely real impedance $Z = 1$ . The cavity size is fixed at $R_c = 30$ . . . . .	33
3.6	Maximum growth rate dependence on the angular velocity of the cylinder for the first 3 azimuthal $m$ modes and 2 distinct cavity sizes. The inner cylinder has radius equal to unity and purely real impedance $Z = 1 + 0i$ . . . . .	34

3.7	Motion of the eigenfrequencies of (3.45) corresponding to the 5 lowest energy modes as a function of the cavity radius for a cylinder of radius $R_{\text{BH}} = 1.0$ and real impedance $Z = 1.0 + i0$ for the $m = 1$ case. The observed loop as the cavity is closed upon the cylinder was not presented in [1]. As the rotation of the cylinder is increased, as expected, the growth rate of associated modes increases. In the critical regime $\Omega = 1$ , the lowest energy root never acquires a negative growth-rate. . . . .	35
3.8	Scattering amplitudes for an asymmetric cylinder of size $R = 1$ with $\epsilon = 0.25$ (solid line) and $\epsilon = 0.5$ (dashed line) obtained from the truncation of (3.52) at $m = 8$ . . . . .	38
3.9	Comparison of the scattering amplitudes obtained by solving the matrix equation (3.52) (right plot) with the numerically obtained evolution of the azimuthal fourier components of a reflected pulse (left plot). The inner cylinder has radius $R_i = 1$ , impedance $Z = 0.2$ and asymmetry parameter $\epsilon = 0.25$ . The dashed lines represent the expected scattering amplitudes for $\omega = 0.64$ . . . . .	40
3.10	Fourier components of an initial gaussian wave pulse with parameters S2 (see table 3.1) interacting with a static uniform cylinder (left) and a static asymmetric cylinder (right). The field is confined inside a cavity of size $R_c = 38$ and the cylinder has radius $R_i = 2$ and impedance $Z = 0.2$ . The asymmetric case (right) has $\epsilon = 0.25$ . . . . .	41
3.11	Fourier components of an initial gaussian wave pulse with parameters S2 (see table 3.1) interacting with a static uniform cylinder (left) and a static asymmetric cylinder (right). The field is confined inside a cavity of size $R_c = 38$ and the cylinder has radius $R_i = 2$ , impedance $Z = 0.2$ and angular velocity $\Omega = 0.35$ . The asymmetric case (right) has $\epsilon = 0.25$ . . . . .	43
4.1	Absorbing region model of a BBH . . . . .	48
4.2	Amplification factor $\mathcal{A}_{\omega m} =  \mathcal{A}_+/\mathcal{A}_- ^2 - 1$ for the SA model for two azimuthal modes $m = 1$ (left column) and $m = 2$ (right column), absorption parameter $\alpha = 5.0$ (top row) and $\alpha = 10.0$ (bottom row) for several rotation speeds. The curves are presented in terms of the frequency parameter $\varpi = \omega/m\Omega$ . . . . .	51
4.3	2D plot of cavity resonances (Bessel functions). On the upper left corner of each plot we have indicated $(m, k)$ where $m$ is the azimuthal mode and $k$ is the order of the frequency that satisfies the boundary conditions. . . . .	54
4.4	(Left) Parametric curves (4.32) for the first 6 bessel roots and $m = 1$ as a function of the absorption parameter $\alpha$ . The curves start at the bessel zeros (solid points). (Right) The evolution of the real (dashed lines) and imaginary (solid lines) of the allowed frequencies shown on the left-most plot. . . . .	55

4.5	Root finding procedure illustration for the case of a maximally rotating cylinder $R_{BH}\Omega = 1$ with absorption parameter $\alpha = 1$ in a cavity of size $R_c = 30$ . (Left) Root behaviour as the absorption parameter is increased from 0 to 1. All roots acquire a negative part, corresponding to absorption on a timescale of the order $1/\omega_l$ . (Right) Behaviour of previously found roots as the rotation of the cylinder is increased. Roots whose real part satisfied the superradiant condition (2.23) have a positive imaginary component. . . . .	56
4.6	Maximum growth rate dependence on the absorption parameter $\alpha$ for the azimuthal modes $m = 1$ and $m = 2$ and several cavity sizes. For small $\alpha$ , the relation is close to linear, in agreement to what was observed for stars [2]. . . . .	56
4.8	Snapshots of field configuration for three distinct simulation times for an initial Gaussian pulse of the form presented in (4.11) with the initial conditions presented in Table 4.1 (SA model). The cavity has a radius $R_c = 38$ and the absorbing cylinder is rotating with constant angular velocity $\Omega = 0.35$ . As explained in the text, the angular pattern corresponds to that of a quadrupolar $m = 2$ mode, and the rotation of the cylinder excites predominantly a radial mode with overtone $k = 5$ ( $k = 0$ is the fundamental mode), hence with six nodes, as can be seen in the radial profile. . . . .	58
4.9	Mode decomposition of the field at a radius of $r = 30$ for an initial Gaussian pulse of the form (4.11) with the parameters presented in Table 4.1 (SA model) in a cavity with radius $R_c = 38$ . The absorbing cylinder is rotating with angular velocity $\Omega = 0.35$ . The dashed black line depicts the analytically obtained growth rate of the fastest growing mode. The numerically obtained frequency of the field is $\omega = 0.5560 + 0.000677i$ . See also figure 4.10. . . . .	59
4.10	Comparison of the real part of the SA model eigenfrequencies with the numerical data for the simulation whose parameters are presented in Table 4.1 (SA model). The top plot represents the analytical eigenfrequencies in the complex plane. The bottom one depicts the Fourier analysis of the field displacement at $r = 20$ for the time interval $\Delta t = [3000, 4000]$ . Note that all roots with positive imaginary part lie below the superradiant threshold (red solid line). . . . .	60
4.11	Snapshots of field configuration for three distinct simulation times for an initial Gaussian pulse of the form presented in (4.11) with the initial conditions presented in Table 4.1 (BA1). The cavity has $R_c = 57$ and the two absorbing cylinders are in a circular orbit of radius $R_0 = 7.15$ . The orbital period is $T \approx 85$ . Note that one could expect frequencies close to $\lesssim m\Omega$ to be excited and hence – based on figure 4.10 – that the fundamental mode is excited to higher amplitude. This expectation seems to be supported by the radial profile of the scalar field. See also the main text and Table 4.3. . . . .	61

4.12	Mode decomposition of the field at a radius of $r = 20.0$ for the simulation depicted in figure 4.11 (see Table 4.1 for initial configuration parameters). The initial field azimuthal mode is $m = 2$ . The generation of higher, even-parity harmonics is observed from the first interaction with the binary. The dashed black is a linear fit to the $m = 2$ curve at late times (shifted upwards). The initial interaction generates other harmonics with the same parity ( $m = 0, 4, \dots$ ) that seem to follow the same growth rate. Odd parity modes ( $m = 1, 3, \dots$ ) are also present but grow from the numerical noise and have growth rates larger than even modes. . . . .	62
4.13	Fourier analysis of the field displacement at a radius of $r = 20.0$ for the simulation of depicted in figure 4.11 (see Table 4.1 for initial configuration parameters). The initial field azimuthal mode is $m = 2$ . The left panel depicts the spectrogram of the field while the right one represents the averaged power spectrum. The dashed lines represent the natural frequencies of the cavity $j_{k,m}/R_c$ with $m = 2$ . The blue region represents the frequencies above the superradiant threshold $\omega > m\Omega$ with $\Omega$ being the orbital Kepler frequency. The dominant mode corresponds to the lowest energetic mode of the cavity, but higher frequencies (above the usual threshold value) are also excited. . . . .	63
4.14	Energy growth rate dependence on the orbital radius of the two equal mass binary in a cavity of radius $R_c = 57$ (note the factor two in the axis, since the growth rate should be twice as large as that of the field itself). Dots represent the numerically obtained energy growth rates, while the dashed line corresponds to a quadratic spline. The vertical lines represent the radii defined by Eq. (4.38). The initial pulse parameters are presented in Table 4.1. We used the BA1 (BA2) initial pulse parameters for the bottom (top) plot. . . . .	64
4.15	Energy growth rate dependence on the cavity radius for the BA with $R_0 = 7.1$ . The vertical dashed lines correspond to the resonant cavity (4.39). The initial pulse parameters are given in Table 4.1. The envelope of the local peaks scale approximately as $\sim 1/R_c$ . The local behavior has a steeper dependence. For example, around the first local peak, we find $\gamma \propto R_c^{-5}$ . The initial pulse considered has the BA1 set of parameters presented in Table 4.1. . . . .	67
C.1	Convergence analysis of the simulation shown in figure. 3.11. The left plot displays analysis of the energy density inside the cavity according to expression (C.23). The right panel shows the same analysis for the energy growth rate averaged over $\Delta t = 20$ . The multiplying factor corresponds to the $Q$ -factor. The results are consistent with 2nd order convergence. . . . .	90
C.2	Convergence analysis of the simulation shown in figure. 4.11. The left plot displays analysis of the energy density inside the cavity according to expression (C.23). The right panel shows the same analysis for the energy growth rate. Results are consistent with 2nd order convergence. . . . .	90

E.1 Amplification factor  $\mathcal{A}_{\omega ml} = |\mathcal{A}_+/\mathcal{A}_-|^2 - 1$  for the absorbing sphere for  $l = m = 1$  (left plot) and  $l = m = 2$  (right plot), absorption parameter  $\alpha = 10.0$  and several rotation speeds. The curves are presented in terms of the frequency parameter  $\varpi = \omega/m\Omega$ . Compare with the 2D equivalent results in figure 4.2. . . . . 96



# Glossary

**BH** Black Hole.

**BHB** Black Hole Binary.

**CDM** Cold Dark Matter.

**DM** Dark Matter.

**GR** General Relativity.

**GW** Gravitational Wave.

**MACHO** Massive Compact Halo Object.

**WIMP** Weakly Interacting Massive Particle.



# Chapter 1

## Introduction

First published in 1915, Einstein's Theory of General Relativity (GR) is undoubtedly one of the greatest achievements of modern scientific thinking [3]. Having overthrown the Newtonian view of the Universe, GR is the most accurate and complete description of gravity developed to date. Besides having changed the way we perceive and think about reality, Einstein's vision of the universe has shown itself prolific at describing and predicting a plethora of observable phenomena [4].

Over the past century, GR has made its way into every astrophysicist's toolbox and the recent detection of Gravitational Waves (GWs) [5] is just another example that ratifies how crucial a tool GR is. It is, however, not a perfect theory. If on one hand it breaks down at quantum scales, it shows a bigger problem when looking at cosmological ones. If the theory is correct at very large scales, there must exist large quantities of non-visible, self gravitating type of matter in the universe - Dark Matter (DM). The DM Problem is one of the most interesting and deep open questions in today's scientific paradigm and has driven research for the past 100 years in experimental and fundamental physics [6]. But even so, the nature and properties of this exotic type of matter remain a mystery.

### The Dark Matter Problem

The idea that non-visible, gravitating matter can permeate our universe is not a recent one. It dates back prior to the development of Einstein's theory of General Relativity and has a fascinating history behind it. In fact, although the first use of the term *Dark Matter* is commonly attributed to Fritz Zwicky in his 1933 work [7], the idea that non luminous bodies (dark stars, planets or clouds) could permeate our galaxy was discussed amongst astronomers already in the 19th century [8].

One of the first examples of what one may call Dark Matter dates back to 1846 when the anomalies in the orbit of Uranus led to the proposal of the existence of an 8th planet. The knowledge of the acclaimed universal law of gravitation published by Newton more than 150 years before [9] allowed le Verrier to predict the existence of this invisible planet (later to be called Neptune) that could explain the erratic motions of Uranus.

Although seemingly unrelated with today's notion of DM, the underlying reasoning for the postulation of this planet is not unlike the one behind today's reasoning for the existence

---

of large amounts of DM in our universe. The knowledge of how things should gravitate and the observational fact that they do not do so as expected points at the existence of matter that we simply cannot directly observe.

On a galactic scale, the first evidence for dark matter came to light at the beginning of the 20th century, when Lord Kelvin, with a very crude model of the Milky Way, was able to put forward the first quantitative limits on the number of dark bodies in our galaxy [10]. In the following 30 years, kinematic studies and the development of several galactic models allowed ever better estimates of the matter density in the vicinity of the solar system. Most of these studies pointed out to a larger density than what was expected from the amount of luminous matter we could observe.

In 1933, the truly pioneering paper by Zwicky [7] showed that this discrepancy was not only present in the vicinity of our solar system but also at much larger scales. Building on the work of Hubble and Humason [11], Zwicky showed that the mass of galactic clusters inferred from the Virial theorem was much larger than what one could observe. Although contested by many of his peers, the results strongly suggested that the amount of matter, we could detect was not enough to keep the cluster from flying apart. In the following years, building on these works, this type of discrepancy was found in many other astrophysical objects but a number of questions regarding the assumptions made by these studies (namely that such clusters were in equilibrium - a necessary condition for the usage of the Virial theorem) kept the scepticism among most of the scientific community. It was not until the 1970's that while studying the rotation curves of galaxies, Rubin, Ford and Freeman found clear and irrefutable evidence that our understanding was flawed [12, 13].

Rubin's results shifted the scientific community vision on the DM problem from being a fight among astronomers and their observational measurements to being the biggest unresolved problem in 20th century physics.

## Dark Matter Today

Even though the idea that great amounts of matter were missing in cosmological significance became broadly accepted by the seventies, it remained to determine the nature, properties and how to detect this large amount of missing matter.

One of the first proposed ideas was that DM could be composed of very faint compact objects such as late stage dwarf stars, neutron stars or black holes. These Massive Compact Halo Objects (MACHOs) would account for the missing matter without easily being observed. Although MACHOs are not the final solution, we know today that they can represent up to 20% of the DM content of our galaxy [14].

The remaining viable options come from the joint efforts of cosmologists, astronomers and particle physicists and all come in the form of some new fundamental particle. The accidental discovery of the Cosmic Microwave Background (CMB) in 1965 by Penzias and Wilson [15] and the subsequent development of precision cosmology [6] allowed the development of physically motivated particle models that could explain the observed discrepancies.

Over the years, a great number of proposed models were excluded from observational data. Baryonic like matter was early discarded because it could not account for the observed

anisotropies in the CMB [16]. The neutrino, a very acclaimed early proposal, was also discarded. It satisfies all the criteria, but, being relativistic particles (or in cosmologist's terms, *hot*), cannot have accounted for the clumping of matter in the early stages of the universe necessary for the formation of structures such as galaxies [17].

The current most promising possibilities fall in the category of what is commonly called cold dark matter (CDM). In this category, the most well known contenders are weakly interacting massive particles (WIMPs) and Axions. WIMPs appear as extensions to the Standard model of particle physics and represent themselves a large category of DM candidates. Axions are very light particles that naturally arise when solving the strong CP problem in quantum chromodynamics [18, 19].

In the CDM paradigm, these are not the only viable options and a great number of other possible candidates exist.

### The Fuzzy Solution

Among the CDM models, those that consider very light bosons represent the current best effort at tackling the DM problem. They allow the correct description of the observed large scale structures in the universe while avoiding some of the problems that arise when more massive particles are considered [20, 21, 22]. These short scale problems appear when one tries to model baryonic physics (e.g. star formation) and can be linked to the typically short De Broglie wavelengths of such models. For a particle of mass  $m$  with a typical velocity  $v$ , its De Broglie wavelength is given by

$$\lambda_B = \frac{2\pi\hbar}{mv}, \quad (1.1)$$

where  $\hbar$  is the reduced Planck constant.  $\lambda_B$  marks the scale at which the wavelike behaviour of a particle becomes relevant. When considering lighter particles, this scale can be pushed to sub-galactic lengths and hence avoid the small scale problems [23] previously mentioned.

Candidates that fall in this particular subset of CDM models are usually referred to as Fuzzy or Ultralight DM models. They are characterized by having a mass of  $\sim 10^{-22}$  eV and, for typical velocities in galactic halos [20], have a De Broglie wavelength of

$$\lambda_B \sim 0.5 \text{ kpc} \left( \frac{10^{-22} \text{ eV}}{m} \right) \left( \frac{250 \text{ km/s}}{v} \right). \quad (1.2)$$

Knowing the typical density of DM in the vicinity of our solar system to be  $\sim 0.5$  GeV, we can estimate the total number of DM particles in a De Broglie volume  $\lambda_B^3$  to be

$$N \sim 10^{96} \left( \frac{10^{-22} \text{ eV}}{m} \right)^4 \left( \frac{250 \text{ km/s}}{v} \right)^3 \quad (1.3)$$

The occupancy number  $N$  is so large that the individuality of particles can be neglected and the modelling of such fuzzy matter can be made resorting to classical waves, much like electromagnetic fields with a large number of photons can be described by classical electric and magnetic fields. This behaviour represents the main motivation for the study of classical

---

scalar fields in astrophysical contexts.

## **Black Holes as Detectors**

The fuzzy nature of ultralight fields and their weak coupling to the SM makes it extremely hard to probe their properties on sub-galactic scales. Their coupling to gravity, however, makes them prone to create, shape and interact with gravitational fields. BHs, with their extreme fields are present themselves as the perfect laboratory to probe the nature of such CDM candidates.

Although BHs have had the tendency to be overlooked as cosmic vacuum cleaners, the last decade has shown that they are anything but that. In the particular effort to probe the nature of DM, the discovery of superradiance in BH physics boosted the research interest in the interaction of scalar fields with BHs [24]. Superradiance can be thought as the wavelike analogue of the famous Penrose process [25] whereby particles interacting with a rotating black hole can be scattered off and ejected with a greater energy than the one they had initially. In the wave analogue, an incident scalar wave (e.g. a bosonic field) can extract rotational energy from the BH and be amplified.

The extensive study of superradiance around isolated BHs has not only allowed a better understanding of Einstein's field equations, but also to place real constraints on the mass of very light bosonic fields [26, 27].

By contrast, the dynamics of scalar fields in Black Holes Binary (BHB) systems have yet a long way to be fully understood. The reason falls mainly on the lack of analytical solutions to Einstein's field equations describing such astrophysical setups. Numerical relativity has allowed the study of such systems in an empirical way [28, 29], but the vastness of parameter space and the growing number of possible DM alternatives poses us with an ever growing list of unanswered questions.

The increasing number of detected GWs [30] from compact object mergers and the increased sensitivity towards detecting such signals projected for the next generation GW detectors [31, 32, 33] makes it important to understand how exactly such ultralight fields can shape the dynamics of these systems and how upcoming data can be better used to probe its fundamental nature and properties.

## **Objectives and Structure of Master Thesis**

This Master Thesis aims at tackling concrete steps towards understanding the dynamics of scalar fields in binary systems of compact objects.

It is known that energy can be extracted from isolated BHs moving through a scalar cloud of DM [34] and that BHBs can exchange energy with ultralight fields [35, 36], but few works have tackled the problem in a systematic way. The lack of analytical tools and the expensive computational alternatives to tackle the problem in its full generality force us to seek for alternative descriptions.

To this end, we consider throughout the following chapters several distinct toy models that retain the most fundamental characteristics of binary systems and allow us to study the

problem in a more consistent way.

Besides serving the general scientific community with new and interesting results, however, this document also aims at serving younger students taking their first steps in the amazingly rich field of gravitational physics with a clear exposition of fundamental concepts in the field.

Chapter 2 serves as a pedagogical introduction to the theory of GR, BHs and Superradiance phenomena. It is intended to give a broad idea behind some of the more mathematical concepts of GR and can be skimmed over by more experienced readers. Section 2.4, however, presents some previously unseen behaviour regarding the Press and Teukolky BH bomb [37].

Chapter 3 presents the first toy model considered. The study builds on the work presented in [1]. Besides containing a more extensive study of the original uniform rotating cylinder model, the chapter extends the analysis to the case of an asymmetric rotating cylinder that better mimics the geometric properties of binary systems.

Chapter 4 presents the second toy model. It represents a more physically motivated toy model that better models a binary system of compact objects. The work presented is mostly based on the publication [38], done in collaboration with Prof. Vitor Cardoso and Dr. Miguel Zilhão, but contains several important results that did not make it to the published manuscript.

---

---

## Chapter 2

# Superradiance in Curved Spacetimes

### 2.1 General Relativity

When first reading about General Relativity, an undergraduate rapidly realizes that the language in which the theory is written is very different from what he learned when studying Classical Mechanics. That is because GR presents us with a completely new way of looking at the world. It challenges our deep rooted notion of space and time as independent and very distinct concepts and recasts our mathematical description of the universe in a new language. This conceptual jump allowed GR to become an important tool in every physicist's arsenal and to take a very special place in many of our hearts. Many have tried to encapsulate the mathematical rigour and the physical reasoning behind GR in just a few pages. I will not try to accomplish such a feat and instead fall back on briefly describing the theory with the aim of giving the young students the intuition behind some of the fundamental concepts of the theory.

#### 2.1.1 Curved Spaces

Consider some path in  $\mathbb{R}^2$  described by the parametric curve  $\mathbf{q}(t) = [x(t), y(t)]$ . If we take a very small portion of this curve, its length will be given by

$$ds = |d\mathbf{q}| = \sqrt{\langle d\mathbf{q}, d\mathbf{q} \rangle} = \sqrt{\langle \dot{\mathbf{q}}, \dot{\mathbf{q}} \rangle} dt, \quad (2.1)$$

where  $\dot{\mathbf{q}}$  can be interpreted as the tangent vector to the curve at a specific point and  $\langle \cdot, \cdot \rangle$  represents the inner product. The complete length of the path can then be calculated by adding up all the little pieces together. In Cartesian coordinates  $(x, y)$  this length is given by

$$l = \int_t \sqrt{\left(\frac{dx}{dt}\right)^2 + \left(\frac{dy}{dt}\right)^2} dt. \quad (2.2)$$

There is nothing special about using this particular set of coordinates. Take for example, the polar coordinates  $(r, \theta)$  that relate to the Cartesian ones as

$$\begin{aligned} x &= r \cos \theta \\ y &= r \sin \theta . \end{aligned} \tag{2.3}$$

By using the chain rule and (2.2) we find that in this new set of coordinates the length of our curve is given by

$$l = \int_t \sqrt{\left(\frac{dr}{dt}\right)^2 + r^2 \left(\frac{d\theta}{dt}\right)^2} dt . \tag{2.4}$$

Both equations represent the length of the same curve but in different coordinate systems. Notice that the only difference between the two equations is the prefactor in the  $(d\theta/dt)^2$  term.

As a very simple application of both equations, we can calculate the length of a circular trajectory in the plane. In Cartesian coordinates, this path is parametrized as  $\mathbf{q}(t) = [R \cos(t), R \sin(t)]$  and using (2.2) we get the usual expression for the circumference of a circle  $l = 2\pi R$ . In polar coordinates, the same path gets parametrized as  $\mathbf{q}(t) = [R, t]$  and using the appropriate expression in (2.4) we obtain the expected result.

If we move up one dimension, the length of a path  $\mathbf{q}(t) = [x(t), y(t), z(t)]$  in  $\mathbb{R}^3$  is analogously given by

$$l = \int ds = \int_t \sqrt{\left(\frac{dx}{dt}\right)^2 + \left(\frac{dy}{dt}\right)^2 + \left(\frac{dz}{dt}\right)^2} dt . \tag{2.5}$$

The 2-dimensional expression (2.2) is retrieved if we restrict the path to be contained in some plane ( $x + y + z = \text{constant}$ ). We can also consider more interesting bidimensional surfaces to confine our path to. Take for example a sphere ( $x^2 + y^2 + z^2 = \text{constant}$ ) where each point on its surface can be pinned by its azimuthal and zenith angles,  $\phi$  and  $\theta$  respectively. These new coordinates relate to the Cartesian ones as

$$\begin{aligned} x &= R \sin \theta \cos \phi \\ y &= R \sin \theta \sin \phi \\ z &= R \cos \theta . \end{aligned} \tag{2.6}$$

Using again the chain rule and (2.5), the length of a curve on the surface of the sphere (whose coordinates on the sphere are parametrized by  $\theta(t)$  and  $\phi(t)$ ) can then be calculated by

$$l = \int_t \sqrt{R^2 \left(\frac{d\theta}{dt}\right)^2 + R^2 \sin^2 \theta \left(\frac{d\phi}{dt}\right)^2} dt . \tag{2.7}$$

Although representing curves on a more complicated surface, this equation takes the same form as equations (2.2) and (2.4) with the clear difference being the distinct prefactors for each of the tangent vector components.

When we write the above equations, what we are actually doing is defining a specific inner product to use in (2.1). Given two vectors  $\mathbf{v}$  and  $\mathbf{w}$ , we can define a generic inner product as

$$\langle \mathbf{v}, \mathbf{w} \rangle = \mathbf{g}(\mathbf{v}, \mathbf{w}) = \sum_{\mu\nu} g_{\mu\nu} v^\mu w^\nu . \quad (2.8)$$

The object  $\mathbf{g}$  is called the metric tensor. In a very simplistic way, it is a *machine* that takes any two vectors and returns a scalar quantity - the inner product. The metric is an abstract object that exists regardless of the coordinates we chose to describe our vectors, i.e, regardless of whether we choose Cartesian or Polar coordinates, the inner product of two vectors always gives the same result.

To perform calculations, however, we must choose a specific coordinate system. When we do this, we specify not only the way we express the components of our vectors  $v^i$  and  $w^j$  but also how we express the components of the metric tensor  $g_{ij}$ . In the  $(x, y)$  Cartesian coordinates, we get by (2.1) that the size of an infinitesimal displacement is

$$ds^2 = dx^2 + dy^2 \quad (2.9)$$

from where we see that the metric components are  $g_{xx} = g_{yy} = 1$  with all other components equal to zero. If instead we consider the  $(r, \theta)$  polar coordinates we have instead

$$ds^2 = dr^2 + r^2 d\theta^2 \quad (2.10)$$

where the only non vanishing metric components are now  $g_{rr} = 1$  and  $g_{\theta\theta} = r^2$ . Both expressions refer to distances on a plane but the fact that we choose a specific set of coordinates made the metric components take a particular form.

Albeit the different coordinates, both (2.9) and (2.10) describe the metric of a 2 dimensional plane. The metric of the sphere one can infer from (2.7) describes distances on a very different bidimensional surface.

To understand the difference let's consider a simple example. Take two close points along the equator of a sphere and make them move in a perpendicular direction to it. While the lines begin parallel, it is easy to see that the point's trajectories will eventually cross at the pole. This convergence of parallel lines tells us that we are not on a plane but instead on a curved space. The details of how one defines parallelism and curvature are filled with subtleties but the main idea behind the concept of curvature can be grasped with this simple example. The important aspect to retain is that the metric tensor holds the information about the geometry of our space - a sphere is intrinsically different from a plane.

Moreover, although we have a clear picture of a 2 dimensional spherical surface, the space exists regardless of whether we can visualize it or not. If some random stranger in the street handed you the metric

$$ds^2 = (R + r \cos \nu)^2 du^2 + r^2 d\nu^2 \quad (2.11)$$

it would not be clear that you could visualize this as a doughnut-shaped surface embedded in 3-dimensional space!

### 2.1.2 Einstein's Happiest Thought

In 1905, Einstein introduced the world to the Theory of special relativity, overthrowing the Newtonian view of time as static and independent from space. In Einstein's picture of the universe, space and time are part of one and the same thing - spacetime - in which all objects move. Just like the trajectory of points on the surface of a sphere are governed by its geometry, the motion of any body in our universe is described by its metric.

The fact that the velocity of light should be constant to every observer places strong constraints on the geometry of our universe and allowed Einstein to state that spacetime's metric takes the form

$$ds^2 = -c^2 dt^2 + dx^2 + dy^2 + dz^2 \quad (2.12)$$

where  $t$  is the time coordinate and  $(x, y, z)$  the usual Cartesian ones. The minus sign in the time component of the metric is the crucial part that makes relativity work. This metric describes a flat universe in the sense that, like in the plane, parallel lines never cross. Einstein's genius was to understand exactly how to incorporate gravity in this picture.

Imagine you are in an elevator that goes straight to the centre of the earth when suddenly the cables that sustain the cabin break and you, along with everything else that might be in the elevator, start to free fall towards the centre of the earth. In the time you have until you meet your inevitable fate <sup>1</sup>, you decide to conduct a very simple experiment. You take two small objects and place them floating at a certain distance from each other. Since all bodies are falling towards the geometric centre of the earth, you will observe that the objects will approach each other as time passes, meeting just as the centre of the planet is reached. While free falling, however, you do not feel the pull of gravity. Nothing feels different from floating in deep space. However, in outer space, the objects inside the cabin would not move at all - their trajectories in spacetime would never cross. The conclusion reached by Einstein is that the presence of matter (like planet earth) makes spacetime curve as to change the way all bodies move in it, effectively making locally straight trajectories not globally so. The idea that gravity is nothing but a geometric property of spacetime was, as he himself said, his happiest thought.

### 2.1.3 Geometrodynamics

From having his happiest thought to putting the theory on paper, it took Einstein almost 10 years to really understand the mathematics required to make his theory work. In 1915 he finally published his findings.

In GR's framework, gravity is described as the distortion (curvature) of space time. The movement of any body is dictated by how spacetime is curved and the way in which spacetime is distorted is dictated by how matter and energy are distributed in it. This dynamical interaction between spacetime and matter/energy is encapsulated in Einstein's field equations:

$$G_{\mu\nu} = \frac{8\pi G}{c^4} T_{\mu\nu} \quad (2.13)$$

---

<sup>1</sup>Approximately 23 minutes

The left hand side term  $G_{\mu\nu}$  is called Einstein's tensor and describes the geometry of spacetime.  $G_{\mu\nu}$  is a function of the metric  $g_{\mu\nu}$  and its first and second derivatives. The right hand side  $T_{\mu\nu}$  is called the Energy momentum tensor and dictates the distribution of matter and energy in space time. As John Wheeler put it:

*"Spacetime tells matter how to move and matter tells spacetime how to curve"*

Although Einstein's field equations can be cast in the very simple form, equation (2.13) comprises in fact a set of 10 non-linear partial differential equations in 4 independent variables (our coordinates). Solving this equation encompasses specifying a particular matter and energy distribution (i.e, defining  $T_{\mu\nu}$ ) and finding a metric  $g_{\mu\nu}$  that satisfies the set of differential equations.

When our spacetime is devoid of any matter ( $T_{\mu\nu} = 0$ ) we can obtain what are called vacuum solutions. A trivial example is the Minkowski flat metric (2.12) but this is not the only vacuum spacetime that solves Einstein's equations.

After just a month of the publication of Einstein's results, the German physicist Karl Schwarzschild found an exact solution to the vacuum equations by assuming the spacetime to be static and spherically symmetric. The metric that now bears his name describes the spacetime around a point-like body of mass  $M$  and is usually written as

$$ds^2 = - \left(1 - \frac{2M}{r}\right) dt^2 + \left(1 - \frac{2M}{r}\right)^{-1} dr^2 + r^2 d\theta^2 + r^2 \sin^2 \theta d\phi^2 \quad (2.14)$$

where  $(r, \theta, \phi)$  are the Schwarzschild coordinates. The interpretation that this metric describes a point-like mass does not clash with the vacuum nature of the solution. In fact, at any point but the very central point (where the solution breaks down) no matter or energy exist.

A key feature of this solution is the existence of a spherical surface at radius  $R = 2M$  that divides the spacetime in two regions. This surface, called an *event horizon*, is what defines a Black Hole. Any point on the inside of this surface cannot be causally connected to any point on the outside. In other words, what happens/is inside a black hole, stays inside a black hole. As soon as one crosses this surface, it is doomed to eventually end up at the central point of the solution - the *Singularity*.

If one considers the central mass to be rotating, the geometry of spacetime is no longer described by the Schwarzschild metric but instead by the Kerr solution. For a point-like mass  $M$  rotating with angular momentum  $J$  this metric can be written as

$$ds^2 = - \left(1 - \frac{2Mr}{\rho}\right) dt^2 - \frac{4Mr a \sin^2 \theta}{\rho} dt d\phi + \frac{\rho}{\Delta} dr^2 + \rho^2 d\theta^2 + \left(r^2 + a^2 + \frac{2Mr a^2 \sin^2 \theta}{\rho}\right) \sin^2 \theta d\phi^2 \quad (2.15)$$

where for simplicity the scale parameters  $a$ ,  $\rho$  and  $\Delta$  are defined as

$$\begin{aligned} a &= J/M \\ \rho &= r^2 + a^2 \cos^2 \theta \\ \Delta &= r^2 - 2Mr + a^2 . \end{aligned} \tag{2.16}$$

This metric is written in terms of the Boyer–Lindquist coordinates  $(r, \theta, \phi)$  that are related to the usual Cartesian ones by

$$\begin{aligned} x &= \sqrt{r^2 + a^2} \sin \theta \cos \phi \\ y &= \sqrt{r^2 + a^2} \sin \theta \sin \phi \\ z &= r \sin \theta \end{aligned} \tag{2.17}$$

and should not be confused with the coordinates used to write down the Schwarzschild solution (2.14). It is not hard to show that this metric reduces to the static case when  $a \rightarrow 0$  and to the flat one when  $M \rightarrow 0$ .

Just like in the Schwarzschild solution, here too we have an event horizon. In fact, this time, we have two distinct horizons located at

$$r_{\pm} = M \pm \sqrt{M^2 - a^2} . \tag{2.18}$$

that separate the spacetime in 3 distinct solutions. The use of spheroidal coordinates makes the event horizons appear at a constant  $r$ -coordinate value but using the appropriate transformation (2.17) we can see that in fact it appears as an oblate surface (similarly to the bulging in rotating bodies). Unlike in the Schwarzschild, however, we have another important surface at

$$r_E = M + \sqrt{M^2 - a^2 \cos^2 \theta} \tag{2.19}$$

that corresponds to where the  $g_{tt}$  component of the Kerr metric vanishes. The region between the outer horizon and this outer surface ( $r_+ < r < r_E$ ) is called the ergoregion and plays a very important role in the interaction of the BH with its surroundings. In fact, the existence of an ergoregion is what allows the extraction of energy and mass from a rotating BH [24].

## 2.2 Energy Extraction and Superradiance

Penrose was the first to exactly determine how particles interacting with a rotating BH can be scattered off it with a greater energy than what they initially had [25]. The Penrose process, as it became known, allows BHs to exchange energy with their surroundings, making them dynamical astrophysical bodies.

Penrose's discovery (as well as other seminal works by Hawking [39] and Zeldovich [40]) played a crucial role in the discovery of rotational superradiance in BH spacetimes.

In the context of GR, superradiance can be thought of as the wave-like analogue of the Penrose process, allowing waves to extract rotational energy from a BH.

As first pointed out by Bekenstein [41], superradiance is actually implied when one considers BH spacetimes. According to the second classical law of BHs [42], the change in energy  $\delta M$  of a BH is related to the change in its angular momentum  $\delta J$  through

$$\delta M - \Omega_H \delta J \geq 0 \quad (2.20)$$

where  $\Omega_H$  is the angular velocity of the event horizon. If we consider a wave of frequency  $\omega$  and azimuthal number  $m$ , the ratio between its angular momentum and its energy is given by [24]

$$\frac{\delta M}{\delta J} = \frac{\omega}{m} \quad (2.21)$$

so that inequality (2.20) reads

$$\delta M(\omega - m\Omega_H) \geq 0 \quad (2.22)$$

this means that, when  $\omega < m\Omega_H$ , the BH energy change must be negative  $\delta M < 0$  and thus the incident wave extracts energy from the BH. The threshold relation is so ever present that we shall box it

$$\boxed{\omega < m\Omega_H} \quad (2.23)$$

In very crude terms, if the oscillating frequency of the field is smaller than the rotational frequency of the BH, then it gets amplified. Besides the azimuthal number  $m$  present in (2.23), the reasoning is not unlike our daily experience - it is just a statement of how energy flows from one system to another.

### 2.3 Scalar fields in Spacetime

To understand how ultralight scalar fields come into the picture we must take a step back and understand how Einstein field equations are obtained.

Just like in classical mechanics we can obtain the equations of motion of a theory by applying the variational principle to an appropriate action  $S$ . Einstein's equations are obtained from the Einstein-Hilbert action

$$S = \int dx^4 \sqrt{-g} \left[ \frac{R}{2\kappa} + \mathcal{L}_{\text{matter}} \right] \quad (2.24)$$

by varying it with respect to its degrees of freedom. In the above equation  $g = \det(g_{\mu\nu})$  is the determinant of the metric,  $R$  is the Ricci scalar (a function of the metric and its derivatives) and  $\kappa = 8\pi G/c^4$ . The  $\mathcal{L}_{\text{matter}}$  term represents the Lagrangian density associated with any matter in our theory and defines the contents of the stress energy tensor  $T_{\mu\nu}$ .

The fact that ultralight bosonic matter is very well described by classical fields, makes a particular set of Lagrangian densities relevant to us. If we consider a scalar field  $\Psi$  minimally coupled to gravity our action reads

$$S = \int dx^4 \sqrt{-g} \left[ \frac{R}{2\kappa} - \frac{1}{2} g^{\mu\nu} \partial_\mu \Psi \partial_\nu \Psi - \frac{\mu^2}{2} \Psi^2 \right] \quad (2.25)$$

where  $\hbar\mu$  is the mass of the field. This action has two degrees of freedom: the metric  $g_{\mu\nu}$  and the scalar field  $\Psi$ . Varying the action with respect to both we obtain two equations of motion:

$$\begin{aligned} G_{\mu\nu} &= \kappa(T_{\text{Scalar}})_{\mu\nu} \\ (\square - \mu^2)\Psi &= 0 \end{aligned}, \quad (2.26)$$

where  $T_{\text{Scalar}}$  is the Energy momentum tensor of the field

$$T_{\text{Scalar}}^{\mu\nu} = (g^{\mu\alpha}g^{\nu\beta} + g^{\mu\beta}g^{\nu\alpha} - g^{\mu\nu}g^{\alpha\beta})\partial_\alpha\Psi\partial_\beta\Psi - g^{\mu\nu}\mu^2\Psi^2, \quad (2.27)$$

and the second equation, known as the Klein Gordon (KG) equation, reads

$$(\square - \mu^2)\psi = \frac{1}{\sqrt{-g}}\partial_\mu(\sqrt{-g}g^{\mu\nu}\partial_\nu\psi) - \mu^2\psi. \quad (2.28)$$

The system of equations (2.26) describes the complete dynamics of our system. The first equation relates how the spacetime metric responds to the presence of the scalar field while the second one tells us how the it evolves in the particular background metric itself helps create. The remarkable non-linearity of this coupled system is as daunting as appealing to an astrophysicist looking for highly rich phenomenology.

Most times, however, we consider the field to have a small amplitude. This physically based approximation, allows terms proportional to  $\Psi^2$  to be dropped. Since the stress energy tensor is quadratic in the field, the first equation in (2.26) reduces to the vacuum Einstein field equations. This allows us to use known vacuum solutions (like Kerr or Schwarzschild) in the second equation to study the dynamics of a field  $\Psi$  on a fixed background spacetime.

## 2.4 The Black hole bomb

The formalism of last section allows us to analytically study the interaction of scalar fields with BHs. The linearization procedure presented is an extremely powerful solution and can be used to show that, under the right conditions, scalar fields can be amplified when interacting with a Kerr BH and lead to superradiant instabilities when confined to repeatedly interact with it.

The content of this section is heavily inspired in references [43, 44] and thus some of the more technical details are left out of our discussion. We focus on massless scalar fields ( $\mu = 0$ ).

### 2.4.1 Scattering Amplitudes

In the linearized approach, the Kerr solution (2.15) describes the fixed background spacetime where the scalar field propagates. Explicitly, the KG equation (2.28) reads

$$\begin{aligned} \left[ \frac{(r^2 + a^2)}{\Delta} - a^2 \sin^2 \theta \right] \frac{\partial^2 \Psi}{\partial t^2} + \frac{4Mar}{\Delta} \frac{\partial^2 \Psi}{\partial t \partial \varphi} + \left[ \frac{a^2}{\Delta} - \frac{1}{\sin^2 \theta} \right] \frac{\partial^2 \Psi}{\partial \varphi^2} + \\ - \frac{\partial}{\partial r} \left( \Delta \frac{\partial \Psi}{\partial r} \right) - \frac{1}{\sin \theta} \frac{\partial}{\partial \theta} \left( \sin \theta \frac{\partial \Psi}{\partial \theta} \right) = 0. \end{aligned} \quad (2.29)$$

The procedure to solve this equation has become widely known due to Teukolsky who tackled not only the behaviour of scalar perturbations but as well of electromagnetic and gravitational ones [44]. Considering the field ansatz

$$\Psi = e^{-i\omega t + im\varphi} S_l^m(\theta) R(r), \quad (2.30)$$

we can separate the KG equation into a radial for  $R(r)$  and a angular one for  $S_l^m(\theta)$

$$\frac{1}{\sin \theta} \frac{\partial}{\partial \theta} \left[ \sin \theta \frac{\partial S_l^m(\theta)}{\partial \theta} \right] + \left[ a^2 \omega^2 \cos^2 \theta - \frac{m^2}{\sin^2 \theta} + A_{lm} \right] S_l^m(\theta) = 0 \quad (2.31)$$

$$\frac{\partial}{\partial r} \left[ \Delta \frac{\partial R}{\partial r} \right] + \left[ \frac{K^2}{\Delta} - \lambda \right] R = 0 \quad (2.32)$$

where  $K = (r^2 + a^2)\omega - am$  and  $\lambda = A_{lm} + a^2\omega^2 - 2am\omega$ . The separation constant  $A_{lm}$  can be obtained from solving the angular equation (2.31) with the appropriate boundary conditions. It is usually represented as a power series in  $(a\omega)$

$$A_{lm} = \sum_n f_n (a\omega)^n. \quad (2.33)$$

The coefficients  $f_n$  are tabulated in the literature [45] and can also be obtained from software like *Mathematica*. In the case of a static BH ( $a = 0$ ) the solutions to the angular equation (2.31) are the spherical harmonics which we now have eigenvalues  $A_{lm} = l(l+1)$ . This is the  $f_0$  term in the  $A_{lm}$  expansion. This approximation of the separation constant is actually quite good for low field frequencies. In fact, it is exact to first order in  $a\omega$

$$A_{lm} = l(l+1) + \mathcal{O}(a^2\omega^2). \quad (2.34)$$

The correct determination of the separation constant is extremely important to solve the radial equation with high precision. Once known, the solutions to equation (2.32) can be found. The procedure followed by Teukolsky starts by rewriting our equations through the definition of an altered radial function  $Y$

$$Y = (r^2 + a^2)^{1/2} R, \quad (2.35)$$

as well as the tortoise coordinate  $r_*$  defined through the differential relation

$$\frac{dr_*}{dr} = \frac{r^2 + a^2}{\Delta} = \left[ 1 - \frac{2Mr}{r^2 + a^2} \right]^{-1}. \quad (2.36)$$

In terms of  $r_*$ , the radial equation (2.32) then takes the form

$$\frac{d^2Y}{dr_*^2} + \left[ \frac{K^2 - \lambda\Delta}{(r^2 + a^2)^2} - G^2 - \frac{dG}{dr_*} \right] Y = 0, \quad (2.37)$$

with  $G = r\Delta/(r^2 + a^2)^2$ . The advantage of using (2.37) is that its asymptotic behaviour can be better understood. For example, when  $r \rightarrow \infty$  ( $r_* \rightarrow \infty$ ) the differential equation reduces to

$$\frac{d^2Y}{dr_*^2} + \omega^2 Y = 0, \quad (2.38)$$

and our the solution becomes simply

$$Y(r_* \rightarrow \infty) \sim \mathcal{A}_+ e^{i\omega r_*} + \mathcal{A}_- e^{-i\omega r_*} \quad (2.39)$$

which translates into a sum of outgoing and incoming waves. In the opposite scenario, when we approach the event horizon  $r \rightarrow r_+$  ( $r_* \rightarrow -\infty$ ), since  $r_+$  is a root of  $\Delta$ , our equation becomes

$$\frac{d^2Y}{dr_*^2} + \left[ \frac{K}{r^2 + a^2} \right]^2 Y = 0, \quad (2.40)$$

near that point. The term inside square brackets can actually be simplified further by noting that

$$\frac{K}{r^2 + a^2} = \omega - \frac{am}{r^2 + a^2} = \omega - \frac{am}{\Delta + 2Mr} \approx \omega - m \frac{a}{2Mr_+} = \omega - m\Omega_H \quad (2.41)$$

where  $\Omega_H = a/(2Mr_+)$  is the angular velocity of the event horizon. We see then that our equation reads

$$\frac{d^2Y}{dr_*^2} + [\omega - m\Omega_H]^2 Y = 0, \quad (2.42)$$

which has a similar form as the one for spatial infinity. We may write the field near the horizon as

$$Y(r_* \rightarrow -\infty) \sim \mathcal{B}_+ e^{i(\omega - m\Omega_H)r_*} + \mathcal{B}_- e^{-i(\omega - m\Omega_H)r_*}. \quad (2.43)$$

As pointed out by Teukolsky [44], the outgoing solution cannot be considered since physically, no signal can come out of the BH. We thus have that

$$Y(r_* \rightarrow -\infty) \sim \mathcal{B}_- e^{-i(\omega - m\Omega_H)r_*}. \quad (2.44)$$

With the two asymptotic solutions (2.44) , (2.39) we can use the Wronskian of our function (a constant throughout the whole domain)

$$W = Y \frac{\partial Y^*}{\partial r^*} - Y^* \frac{\partial Y}{\partial r^*} = 2i \operatorname{Im} \left[ Y^* \frac{\partial Y}{\partial r^*} \right]. \quad (2.45)$$

to prove that scattered waves get amplified by the rotation of the BH. Equating the value of the Wronskian at infinity and at the BH radius we can obtain the following relation between the amplitudes of the fields

$$|\mathcal{A}_+|^2 - |\mathcal{A}_-|^2 = -|\mathcal{B}_-|^2 \left( 1 - \frac{m\Omega_H}{\omega} \right), \quad (2.46)$$

meaning that when the superradiant condition (2.23) is satisfied, the amplitude of the outgoing wave is larger than that of the incoming one.

### 2.4.2 Cavity Modes

If we force our field to be inside a cavity, it must vanish at a certain radius  $R_c$ . This boundary condition forces our field to have some specific frequency  $\omega$  - the ones that allow the boundary conditions to be satisfied. The procedure to find these eigenfrequencies is rather straightforward but we outline it here.

We begin by pointing out that near the horizon, equation (2.36) can be simplified to

$$\frac{dr_*}{dr} = \frac{r^2 + a^2}{\Delta} = \frac{r^2 + a^2}{(r - r_+)(r - r_-)} \approx \frac{1}{(r - r_+)} \left( \frac{r_+^2 + a^2}{r_+ - r_-} \right) \quad (2.47)$$

and so, the tortoise coordinate  $r_*$  can be easily integrated to

$$r_* = \left( \frac{r_+^2 + a^2}{r_+ - r_-} \right) \log(r - r_+) \equiv \eta \log(r - r_+). \quad (2.48)$$

The solution near the horizon (2.44) then reads

$$Y(r) \sim (r - r_+)^{-i(\omega - m\Omega_H)\eta}. \quad (2.49)$$

The reason for such approximations becomes clear when we look at the tortoise coordinate behaviour near the horizon. Since no analytical solution exists for the radial equation we must resort to numerical methods. The expansion (2.49) makes it easy to numerically implement a simple shooting method that avoids the coordinate singularity at the horizon.

To obtain the proper solutions the shooting method integrates equation (2.37) from a point close to the horizon  $r_0 = r_+(1 + \epsilon)$  up until the cavity radius  $R_c$  and evaluates the value of  $Y(r = R_c)$ . If it lies inside a specific tolerance of 0, it satisfies the boundary conditions and we accept it as a solution. If not, we tweak the field frequency  $\omega$  so that it give a better field configuration.

The field frequencies found this way are, in general complex valued. The real part corresponds to the oscillatory behaviour of the field in time while the imaginary part corresponds to

either damping or amplification of the field. If  $\text{Im}[\omega] > 0$  we have superradiant amplification and the field grows in time exponentially.

Besides providing numerical results using the methods above described, the thorough study of the BH bomb done in [43] contained analytical predictions for the case where  $M\omega \ll 1$ , i.e, when the wavelength of the field is much larger than the size of the BH. In this scenario, the authors showed that the eigenfrequencies of the field inside the cavity are approximately given by

$$\omega \sim \frac{j_{l+1/2,n}}{R_c} - i \frac{k}{R_c^{2(l+1)}} \left( \frac{j_{l+1/2,n}}{R_c} - m\Omega_H \right), \quad (2.50)$$

where  $j_{l+1/2,n}$  represents the n-th zero of the Bessel function of the first kind  $J_{l+1/2,n}(x)$  and  $k$  is a constant independent of the cavity radius  $R_c$ . In this approximation, the allowed frequencies sit very close to those natural to an empty cavity given by  $\text{Re}[\omega] = j_{l+1/2,n}/R_c$ . The associated imaginary part is usually very small when compared to the real one but, as expected from the superradiant threshold, becomes positive when  $\text{Re}[\omega] < m\Omega_H$ . When the condition is met, the amplitude of the field grows exponentially on a timescale  $\tau = 1/\text{Im}[\omega]$ .

Both these analytical results were seen to agree very well with the numerical data at the time and in our simulations. However, an important feature seemed to go unnoticed in the original analysis. Figure 2.1 depicts the imaginary part of the eigenfrequencies as a function of the cavity radius for several values of the rotation parameter  $a$  and azimuthal mode  $m$ . Each solid line represents an overtone root of the system and follows the expected behaviour. For cavity radii larger than the threshold value  $R_{l,n} = j_{l+1/2,n}/(m\Omega_H)$ ,  $\text{Im}[\omega]$  increases very quickly, reaches a maximum and then falls as  $\text{Im}[\omega] \propto R_c^{-2(l+1)}$ .

As the initial authors put it, this decrease is expected on physical grounds if we regard the amplification process as a product of the successive amplifications of a pulse travelling between the BH horizon and the cavity walls. Adopting this view, however, one should expect the dependence on  $R_c$  to be proportional to the average time between interactions, i.e, the amplification rate should go as  $\text{Im}[\omega] \propto R_c^{-1}$  instead of having an explicit dependence on the azimuthal number  $l$ . It is only when one considers the behaviour of the distinct roots together that such physical picture appears.

In figure 2.1 the  $\propto R_c^{-1}$  behaviour is shown by the dashed lines. Although each root follows the predicted analytical behaviour, the envelope produced by the several overtones displays the physically expected  $\propto R_c^{-1}$  dependence. We should emphasize however that the dashed lines serve only as visual guides and are not obtained by direct calculation. The dependence seems, nonetheless, to be present for all parameters.

### 2.4.3 Why Cavities?

At first sight, placing a BH inside a cavity might seem like an unrealistic thing to consider but good reasons beside the intellectual challenge of solving an interesting mathematical problem exist.

A reason of practical nature arises when numerically solving the full non-linear set of equations (2.26) we linearized. When doing so, it is impossible to simulate the whole domain

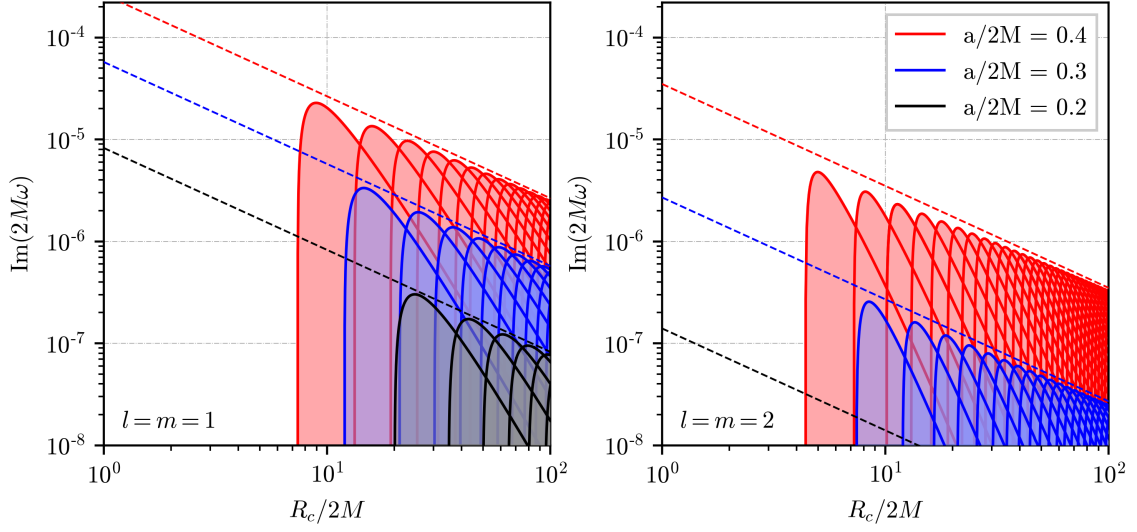


Figure 2.1: Imaginary part of the eigenfrequencies of the field as a function of the cavity radius  $R_c$  for several values of the rotation parameter  $a$  and several field quantum numbers. The left plot corresponds to the  $l = m = 1$  while the one on the right to  $l = m = 2$ . Each solid line corresponds to a different cavity radial mode ( $n = 1, 2, 3, \dots$ ). Note that for each  $n$  there exists a minimal cavity radius for which the mode can be amplified.

of the Kerr solution. Although conformal techniques allow the mapping of the infinite domain to a finite one [24], it is often easier to just impose reflecting boundary conditions at a certain radius and integrate the equations in this finite set. The analytical knowledge of the expected solutions allows the comparison with such numerical results before considering more extreme cases for which no calculations can be easily performed.

The field confinement is also thought to model the effect of considering a massive field. Recall that throughout our analysis we considered a massless ( $\mu = 0$ ) scalar field. The connection between the two models is, however, still unclear. One possible way to close the gap is to study the massive field eigenfrequencies in a similar way to what was done in the previous section. Although the imaginary part of the massive eigenfrequencies is known to be distinctly different from the ones of a cavity [24], their global behaviour may be similar to the  $R_c^{-1}$  and thus justify more clearly the connection of the two descriptions.

Besides this, actual confining mechanisms may exist in nature and resemble the BH bomb model [46, 47]. On the not so natural mechanisms, the authors of [43] went as far as to postulate the possibility of constructing a black hole power plant.

The timescales associated with the amplification of the field vary a lot depending on the parameters chosen. The fundamental  $l = m = 1$  mode seems to always have the largest growth rate. For the  $a = 0.8M$  scenario presented in figure 2.1, the envelope points are approximately given by

$$\omega_l \approx (2.6 \times 10^{-4}) \left( \frac{c}{R_c} \right) \quad (2.51)$$

For BH of solar mass  $M_\odot$ , the associated timescales given by  $\tau = 1/\text{Im}[\omega]$  can range from a

few fractions of a second  $\tau \sim 0.4$  s for cavities with<sup>2</sup>  $R_c \sim 20M \sim 30$  km to a few months  $\tau \sim 10$  Months for a cavity the size of the outermost planetary orbit in the solar system ( $R_c \sim 30$  AU  $\sim 3 \times 10^9$  km). When one considers the BH at the center of our galaxy, these timescales scale by a factor of  $10^8$ . On cosmological (or even galactic) scales, these values represent very short timescales. The probing of BH characteristics as spin and mass can thus hint at the properties of ultralight bosonic fields.

## 2.5 Binary systems

The calculations above presented rely on the assumption that the field has a small amplitude. This allowed us to neglect the stress energy tensor associated with the scalar field and use an already known solution for the homogeneous field equations – the Kerr metric. To study the dynamics of scalar fields in binary systems under the same assumptions one would need to know an exact solution to Einstein’s equations that describes a binary system. To this day, however, no exact solution exists to describe such system.

Exact solutions describing two or more static BHs exist [48] but their application to actual astrophysical scenarios is limited. Almost all of our understanding regarding binaries comes from full numerical simulations or from post Newtonian techniques [49, 50]. In the latter, approach the individual binary components are stationary vacuum BHs, slightly (tidally) deformed in response to the companion’s gravitational field. Such techniques allow the study of binaries at large separations and, along with the numerical methods employed to study tighter orbits, we can in principle know the dynamics at all stages of evolution [29].

For the above reasons, the analytical study of scalar field interactions with binaries presets it as a challenging problem for which no clear solution exists. The increasing number of detected gravitational waves from compact object mergers [30] and the development of next generation detectors makes it important to understand how exactly such ultralight fields can shape the dynamics of these binaries and how upcoming data can be better used to probe its fundamental nature and properties.

The following chapters aim at paving the way towards a more complete understanding of such dynamics by considering physically based toy models that retain the most fundamental aspects behind such astrophysical systems.

---

<sup>2</sup>In geometrized units the mass of the sun reads  $M_\odot = 1.5$  km

## Chapter 3

# Toy Model I

The main limitation to gaining a deeper understanding of the dynamics of scalar fields in BHB spacetimes is the lack of an analytical metric describing such systems. As pointed out in chapter 2, the D’Alambertian operator  $\square$  dependence on the metric makes it unfeasible to study these systems in a completely analytical way. The lack of a metric points at the fact that, either no analytical metric exists or, if one does, it will not be appropriate for any feasible calculation. It is then important to trace new paths about how one can gain deeper insight into these systems.

### 3.1 The Fluid-GR Analogy

One very remarkable result put forward by Uhnru in 1981 is the existence of a connection between the study of perturbations in fluids and that of scalar fields in curved spacetimes [51]. This connection between fluid mechanics and the framework of GR not only allows (as has) the development of simple theoretical models to study, among other phenomena, superradiance in BH spacetimes [52], but also to shed light on this same type of physical processes by actual experiments [53]. Our first model relies heavily on Uhnru’s formalism for which we will briefly overview.

#### 3.1.1 Fluid Dynamics

In fluid dynamics, a compressible fluid (such as a gas or a liquid) for which the effect of viscous stresses and heat fluxes are neglected can be described by a velocity field  $\vec{v}$ , and two scalar quantities  $p$  and  $\rho$ , respectively denoting the pressure and density of the fluid at a certain point. The dynamics of these quantities are governed by a set of two equations: the continuity equation

$$\frac{\partial \rho}{\partial t} + \nabla \cdot (\rho \vec{v}) = 0 , \quad (3.1)$$

and the momentum equation

$$\rho \left[ \frac{\partial}{\partial t} + \vec{v} \cdot \nabla \right] \vec{v} = \vec{F} . \quad (3.2)$$

Both equations, usually referred to as Euler equations, describe local conservation of mass and momentum respectively. The RHS of the latter encapsulates all the forces acting upon the fluid. In the absence of dissipative forces, the force term can only depend on pressure gradients and conservative forces and can thus be written as

$$\vec{F} = -\nabla p - \rho \nabla \Phi , \quad (3.3)$$

where  $\Phi$  is a potential encapsulating all external conservative forces (e.g gravity). Equations (3.1) and (3.2) are, however, insufficient to completely describe the physical system since the number of unknowns is larger than that of equations. The third equation one must provide is an equation of state relating, for example, the pressure and the density at any given point. In the case of a barotropic fluid, i.e where the density is solely a function of pressure, we can define the pressure potential

$$h(p) = \int_0^p \frac{dp'}{\rho(p')} \quad \text{such that} \quad \nabla h = \frac{\nabla p}{\rho} . \quad (3.4)$$

This provides us with a way of writing the force given by (3.3) as the gradient of a single combined potential  $\vec{F} = -\rho \nabla(h + \Phi)$  and the Euler equation as

$$\left[ \frac{\partial}{\partial t} + \vec{v} \cdot \nabla \right] \vec{v} = -\nabla(h + \Phi) . \quad (3.5)$$

In the case of a locally irrotational fluid ( $\nabla \times \vec{v} = 0$ ) this equation is equivalent to an altered form of Bernoulli's equation,

$$\frac{\partial \vec{v}}{\partial t} = -\nabla \left( h + \phi + \frac{v^2}{2} \right) , \quad (3.6)$$

where the vector relation  $\nabla(\vec{v} \cdot \vec{v}) = 2(\vec{v} \cdot \nabla)\vec{v}$  was used. The irrotational nature of the fluid allows us as well to write the velocity field as a gradient of a scalar velocity potential  $\vec{v} = -\nabla\psi$ , turning our vectorial equation into the scalar one

$$\frac{\partial \psi}{\partial t} = \frac{1}{2}(\nabla\psi)^2 - (h + \Phi) . \quad (3.7)$$

We thus conclude that the dynamics of a compressible, irrotational, inviscid and barotropic fluid are governed by the two scalar equations (3.1) and (3.7).

### 3.1.2 Linear Perturbation Theory

If a particular set of configurations  $(\rho_0, p_0, \psi_0)$ , for the density, pressure and velocity potential of the fluid satisfies equations (3.1) and (3.7), the system is said to be in equilibrium. The stability of such solution can be understood by studying the behaviour of small perturbations around these equilibrium configuration:

$$\rho = \rho_0 + \epsilon \rho_1 \quad p = p_0 + \epsilon p_1 \quad \psi = \psi_0 + \epsilon \psi_1 . \quad (3.8)$$

The equations governing the behaviour of the perturbations quantities can be obtained by direct substitution of (3.8) in the original governing equations. The result to first order in  $\epsilon$  of the equation describing the velocity field perturbation  $\psi_1$  is

$$\frac{\partial}{\partial t} \left( \frac{\rho_0}{c^2} \left[ \frac{\partial \psi_1}{\partial t} + \vec{v}_0 \cdot (\nabla \psi_1) \right] \right) + \nabla \cdot \left( -\rho_0 \nabla \psi_1 + \frac{\rho_0}{c^2} \left[ \frac{\partial \psi_1}{\partial t} + \vec{v}_0 \cdot (\nabla \psi_1) \right] \vec{v}_0 \right) = 0, \quad (3.9)$$

where the local sound speed was defined as  $c^{-2} = \partial \rho / \partial p$ .

Although not clear in plain sight, Uhnru realized that this equation can be written as

$$\square \psi_1 = \frac{1}{\sqrt{-g}} \partial_\mu (\sqrt{-g} g^{\mu\nu} \partial_\nu \psi_1) \quad (3.10)$$

with the associated metric tensor being:

$$g_{\mu\nu} = \frac{\rho_0}{c} \begin{pmatrix} -(c^2 - |\vec{v}_0|^2) & -\vec{v}_0^T \\ -\vec{v}_0^i & \vec{I} \end{pmatrix} \quad (3.11)$$

Equation (3.10) states that linear perturbations of a velocity potential in a fluid behave as scalar field perturbations in certain curved spacetimes (compare with equation (2.28)). The casting of this problem in the same language of general relativity - that of differential geometry - allows the bridge to be made between the two scenarios, making it evident that, although not immediate, concepts of GR such as those of event horizons and ergo-regions translate directly to fluid analogous ones. With this, not only can one conceive physical setups to experimentally study the dynamics of scalar fields in (certain) curved spacetimes, but also conceive theoretical fluid analogous models, to understand more complex astrophysical scenarios.

It is not without saying that the analogy is limited and cannot account for all the complexity of GR. One clear indicator is the number of degrees of freedom of the effective metric (3.11). Since at any one point the metric is completely defined by 3 scalar quantities ( $\psi_0$ ,  $\rho_0$  and  $c$ ), it has at most 3 degrees of freedom. A solution to Einstein's field equations (2.13) will have 6 degrees of freedom [54] and thus the fluid analogy can only effectively be equivalent to a subset of spacetimes (that may or may not satisfy the field equations).

It is nonetheless remarkable that, even though the governing equations of our fluid are derived from Newtonian, non-relativistic postulates, the dynamics of perturbations can be described by the same mathematical formalism that underlies scalar field in GR.

For a more complete derivation and discussion of this formalism as well as some concrete examples of how it can actually be used, we refer the reader to [55], [56] and [52].

## 3.2 A fluid analogue of a binary

The Unruh formalism does not solve the problem of not having an appropriate metric for a binary system, but the connection with fluid mechanics allows one to consider physically meaningful setups that have the same symmetries of binary systems. Taking a static fluid of

constant density, the effective metric (3.11) reduces to that of flat Minkowski space

$$\eta_{\mu\nu} = \text{diag}(-1, 1, 1, 1) , \quad (3.12)$$

where we set  $\rho_0 = c = 1$ . The fluid perturbations are thus governed by the usual wave equation

$$\square\psi = 0 \longrightarrow \partial_t^2\psi = \nabla^2\psi . \quad (3.13)$$

The main geometrical feature of a binary is the two fold symmetry present in the system. In astrophysical binaries this is evident from the existence of two absorbing regions of spacetime (be it BHs, stars or other compact objects) that gravitate around the common centre of mass. The geometry of such problems can be mimicked in a simple experimental setup by considering a rotating cylinder immersed in a fluid whose surface impedance (modelling dissipation) has an angular dependence on the azimuthal angle  $\varphi$

$$Z = Z_0 [1 + \epsilon \cos^2(\varphi)] . \quad (3.14)$$

A simple depiction of the impedance dependence of this cylinder is depicted in figure 3.1.

Although the spacetime curvature effects associated with any massive body are not mimicked in this simple model, it can give us some insight into how exactly the twofold symmetry affects interacting fields. It is thus not our goal to completely describe the interaction of scalar fields with binaries of compact objects, but instead understand the geometric signatures left on interacting fields.

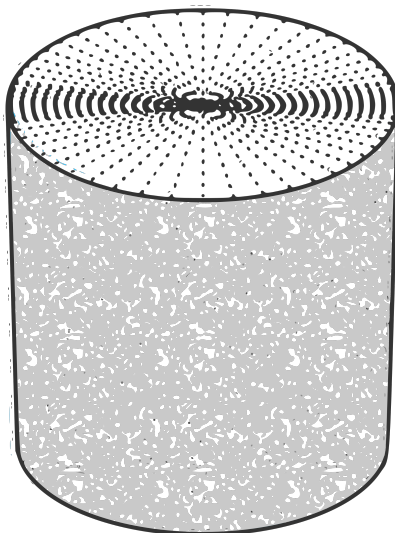


Figure 3.1: Cartoon of a cylinder made of a non homogeneous material. The dotted area on the surface depicts the magnitude of the impedance  $Z$ , which varies with azimuthal angle according to (3.14). The asymmetry mimics that of a binary system.

### 3.2.1 Cylindrical cavity waves

The symmetry of the cylinder model makes the choice of cylindrical coordinates  $(t, r, \varphi, z)$  appropriate for our calculations. In this coordinate frame the wave equation explicitly reads

$$\frac{\partial^2 \psi}{\partial t^2} = c^2 \left[ \frac{1}{r} \frac{\partial}{\partial r} \left( r \frac{\partial \psi}{\partial r} \right) + \frac{1}{r^2} \frac{\partial^2 \psi}{\partial \varphi^2} + \frac{\partial^2 \psi}{\partial z^2} \right], \quad (3.15)$$

that can be solved in a very standard procedure. Namely, by taking the field ansatz

$$\psi(t, r, \varphi, z) = \frac{\phi(r)}{\sqrt{r}} e^{-i\omega t + im\varphi}, \quad (3.16)$$

the wave equation is replaced by a solely radial equation

$$\frac{d^2 \phi}{dr^2} + \left( \frac{\omega^2}{c^2} - \frac{m^2}{r^2} + \frac{1}{4r^2} \right) \phi = 0, \quad (3.17)$$

which is a transformed version of the Bessel equation. For a fixed  $m$ , the solutions can be written in terms of the usual Bessel functions of the first and second kind,  $J_m$  and  $Y_m$  respectively, as

$$\phi_m(r) = \sqrt{r} \left[ C_1 J_m \left( \frac{\omega r}{c} \right) + C_2 Y_m \left( \frac{\omega r}{c} \right) \right], \quad (3.18)$$

or in terms of the Hankel functions of the first and second kind,  $\phi_m^+$  and  $\phi_m^-$  respectively, as <sup>1</sup>

$$\phi_m(r) = \sqrt{r} \left[ \mathcal{A}_+ \phi_m^+ \left( \frac{\omega r}{c} \right) + \mathcal{A}_- \phi_m^- \left( \frac{\omega r}{c} \right) \right]. \quad (3.19)$$

In the above equation, the choice of notation becomes evident when the asymptotic behaviour of these solutions is considered since when  $r \rightarrow \infty$ ,

$$\begin{aligned} \sqrt{r} \phi_m^+ (\omega r/c) &\sim e^{i\omega r/c} && \text{Outgoing Wave} \\ \sqrt{r} \phi_m^- (\omega r/c) &\sim e^{-i\omega r/c} && \text{Incoming Wave} \end{aligned} \quad (3.20)$$

allowing us to associate  $\mathcal{A}_+$  with the amplitude of an outgoing wave and  $\mathcal{A}_-$  with an incoming one.

As we shall see, form (3.19) is most useful when studying scattering problems while (3.18) is most useful in bound state (eigenvalue) problems. In any case, if we require our field to behave as incoming and outgoing waves very far away from the cylinder, i.e.,

$$\phi_m(r)|_{r \rightarrow \infty} = \mathcal{A}_+ e^{+i\omega r/c} + \mathcal{A}_- e^{-i\omega r/c}, \quad (3.21)$$

then the amplitudes of the two solutions (3.18) and (3.19) must be related through (see appendix B)

$$\mathcal{A}_{\pm} = \sqrt{\frac{c}{2\pi\omega}} (C_1 \mp iC_2) e^{\mp i(m\pi/2 + \pi/4)}. \quad (3.22)$$

---

<sup>1</sup>In the literature Hankel functions are commonly denoted by  $H_m^{(1)}$  and  $H_m^{(2)}$ . Our particular notation was chosen as to make our calculations cleaner.

The general solution is thus obtained by summing over all azimuthal numbers  $m$

$$\psi(t, r, \varphi, z) = \sum_m \left[ \mathcal{A}_+ \phi_m^+ \left( \frac{\omega r}{c} \right) + \mathcal{A}_- \phi_m^- \left( \frac{\omega r}{c} \right) \right] e^{-i\omega t + im\varphi} \quad (3.23)$$

It is particularly useful to think of these functions in terms of the dimensionless variable

$$y = \frac{\omega r}{c} \quad (3.24)$$

which takes into account the typical wavelength of our wave-like solution  $\lambda = \omega/c$ .

### 3.2.2 Boundary Conditions

The presence of the cylinder will impose boundary conditions (BC) on the field at its surface, allowing us to find the required relation between incoming and outgoing amplitudes. To understand how this boundary condition is defined we must look back at the fluid description and the physical meaning of impedance.

All physical quantities associated with our fluid can be directly obtained from the scalar velocity potential  $\psi$ . Namely, the pressure perturbation  $p$  and the velocity of the fluid in the radial direction  $v_r$  at a given point are given by

$$p = -\rho_0 \left( \frac{\partial \psi}{\partial t} \right) \quad \text{and} \quad v_r = - \left( \frac{\partial \psi}{\partial r} \right), \quad (3.25)$$

respectively. In the above expression, both  $\psi$  and  $p$  refer to the linear perturbations in equation (3.8)  $\psi_1$  and  $p_1$ , respectively.

At the cylinder's surface, the pressure of the fluid will tend to make it move. To first order, we can take the motion of a point on the cylinder to be independent of all others, depending solely on the pressure of the fluid at that point. For small enough wave amplitudes, this dependence will be linear, meaning that the perpendicular motion of the surface will be proportional to the pressure at that point. The proportionality constant is defined as the inverse impedance  $Z$  (or admittance). Physically, if a surface does not budge when acted upon by the fluid's pressure, it has zero admittance (infinite impedance). The linear relation can thus be written as

$$Z = \frac{\text{pressure}}{\text{surface radial velocity}} = - \frac{p}{v_r}, \quad (3.26)$$

where the minus sign takes into account the normal direction of the surface.

The proportionality constant  $Z$  can take on complex values. In fact, for most materials, the measured impedance has both a real and imaginary part [57].

The real part describes the resistivity of the surface to budge under the applied pressure and takes into account the fact that energy can be dumped into the surface. We shall always consider  $\text{Re}[Z] > 0$  since we wish our cylinder to absorb and not spontaneously emit energy when interacting with the fluid. The imaginary part of the impedance, usually called reactance, accounts for the possibility of a de-phasing between the pressure wave and the

motion of the surface. If the frequency of the perturbation resonates with the cylinder, its reactance will vanish  $\text{Im}[Z] \sim 0$ .

In terms of the dimensionless variable defined in (3.24) and the definitions (3.25), the BC reads

$$\left(\frac{\partial\psi}{\partial t}\right) = -\frac{Z\omega}{\rho c} \left(\frac{\partial\psi}{\partial y}\right), \quad (3.27)$$

and defines the field's behaviour at the cylinder's surface. From the above equation we can define another variable  $\tilde{Z}$  as

$$\tilde{Z} = \frac{Z}{\rho c} = \frac{\text{Impedance of Cylinder}}{\text{Characteristic Impedance of the fluid}}, \quad (3.28)$$

that characterizes the relative impedance of the interacting media.

### 3.2.3 Rotating cylinder

The boundary condition (3.27) is only valid in a frame where the cylinder is static. The rotation of the cylinder can be taken into account by explicitly making the impedance time dependent. If the azimuthal coordinate in the lab frame is  $\bar{\varphi}$  and the cylinder is rotating with angular velocity  $\Omega$ , the impedance at a point on the cylinder's surface is given by

$$\tilde{Z} = \tilde{Z}_0 [1 + \epsilon \cos^2(\bar{\varphi} - \Omega t)], \quad (3.29)$$

In the frame corotating with the cylinder (where the boundary condition is valid), the azimuthal coordinate  $\varphi$  relates to  $\bar{\varphi}$  as

$$\varphi = \bar{\varphi} - \Omega t, \quad (3.30)$$

implying that, in the lab frame, the boundary condition reads

$$\left(\frac{\partial\psi}{\partial t}\right) = -\tilde{Z} \left(\frac{\partial\psi}{\partial y}\right) \pm \Omega \frac{\partial\psi}{\partial\bar{\varphi}}, \quad (3.31)$$

where  $\tilde{Z}$  is given by (3.14).

Placing the explicit dependence in the boundary condition is mostly useful when solving the problem numerically. For an analytical treatment of the problem, however, it is easier to account for the cylinder's rotation by writing all our equations in the frame rotating with the cylinder. By using the coordinate transformation then, we can simply write our solutions as

$$\psi^m(t, y, \varphi, z) = \left[ \mathcal{A}_+ \phi_m^+ \left(\frac{\omega r}{c}\right) + \mathcal{A}_- \phi_m^- \left(\frac{\omega r}{c}\right) \right] e^{-i(\omega - m\Omega)t + im\varphi}. \quad (3.32)$$

## 3.3 Uniform Cylinder

The case of a uniform cylinder ( $\epsilon = 0$  in (3.29)) was extensively studied in [1]. The derivations in this section take a slightly different approach from the article cited, complementing the study of the authors and displaying some new behaviour that was just skimmed over in the

original manuscript. We will study both the scattering off the rotating cylinder as well as the dynamics of the scalar field when confined inside a cavity and bridge this results with feasible experimental setups.

### 3.3.1 Superradiant scattering is implied

Before performing any quantitative calculation one can infer that the amplification of perturbations is implied by evaluating the the Wronskian of the field  $\psi$

$$W = \psi \frac{\partial \psi^*}{\partial r} - \psi^* \frac{\partial \psi}{\partial r} = 2i \operatorname{Im} (\psi^* \partial_r \psi) . \quad (3.33)$$

This quantity is constant at every point and thus relates the value of the function at infinity with its value at the surface of the cylinder. Taking a single  $m$ -mode solution (3.32), we can evaluate the value of the Wronskian at spatial infinity to be

$$W|_{r=\infty} = \frac{2i\omega}{c} [|\mathcal{A}_+|^2 - |\mathcal{A}_-|^2] . \quad (3.34)$$

Similarly, using the same solution and boundary condition (3.27), the wronskian at the cylinder's surface reads

$$W|_{r=R} = 2i \operatorname{Im} \left[ \frac{i\rho(\omega - m\Omega)}{Z} |\psi^m|^2 \right] = -\frac{2i\rho(\omega - m\Omega) \operatorname{Re}(Z)}{|Z|^2} |\psi^m|^2 . \quad (3.35)$$

where  $\psi^m$  is to be evaluated at the cylinder radius. Equating (3.34) and (3.35) we can define the amplification factor

$$\mathcal{A}_{\omega m} = \frac{|\mathcal{A}_+|^2}{|\mathcal{A}_-|^2} - 1 = -\frac{\rho}{c} \left( 1 - \frac{m\Omega}{\omega} \right) \frac{\operatorname{Re}(Z) |\psi^m|^2}{|Z|^2 |\mathcal{A}_-|^2} , \quad (3.36)$$

representing the difference between the total reflection case and the observed amplitude ratio. It is then clear that, for resistive materials ( $\operatorname{Re}[Z] > 0$ ) amplification of the incoming signal is expected when the superradiant threshold condition  $\omega < m\Omega$  is verified.

Although the above equation does not allow us to obtain a concrete relation between the value of incoming and outgoing waves it shows that superradiance is implied in this particular setup.

### 3.3.2 Scattering factors

To calculate the amplification factor defined in (3.36) we need to take the full solution (3.23) and plug it in the boundary condition (3.27). Doing so, the relation between the outgoing/ingoing coefficients is encapsulated in the equation

$$\sum_m \left( \mathcal{A}_+^m \left[ (1 - 1/\sigma) \phi_m^+ + i\tilde{Z} (\phi_m^+)' \right] + \mathcal{A}_-^m \left[ (1 - 1/\sigma) \phi_m^- + i\tilde{Z} (\phi_m^-)' \right] \right) e^{-i(\omega - m\Omega)t + im\bar{\varphi}} = 0 \quad (3.37)$$

where  $\sigma = \omega/m\Omega$ . In the above expression, all the derivatives are taken with respect to the dimensionless parameter  $y$  defined in (3.24) and all functions are evaluated at

$$y_0 = \frac{\omega R}{c} = m \left( \frac{\omega}{m\Omega} \right) \left( \frac{\Omega R}{c} \right) = m\sigma\alpha. \quad (3.38)$$

Note that  $\sigma$  parametrizes the superradiant threshold so that amplification of the signal occurs when  $\sigma < 1$ . The parameter  $\alpha$  introduced is a measure of the cylinder's surface velocity. For  $\alpha$  smaller (larger) than unity we are in the subcritical (supercritical) regime. Since the impedance has no azimuthal dependence, the ratio of the outgoing and incoming amplitudes can immediately be read off to be

$$\frac{|\mathcal{A}_+|^2}{|\mathcal{A}_-|^2} = \left| \frac{(1 - 1/\sigma)\phi_m^- - iZ(\phi_m^-)'}{(1 - 1/\sigma)\phi_m^+ - iZ(\phi_m^+)'} \right|^2. \quad (3.39)$$

In figure 3.2 we have plotted the amplification factor as a function of the threshold parameter  $\sigma$  for two distinct cylinders and several rotation speeds. The bottom-left plot is a more complete version of figure 1 of [1].

As expected by equation (3.36), amplification is always observed. Interestingly, the existence of an imaginary part in the impedance value of the cylinder leads to a peak value around certain frequencies.

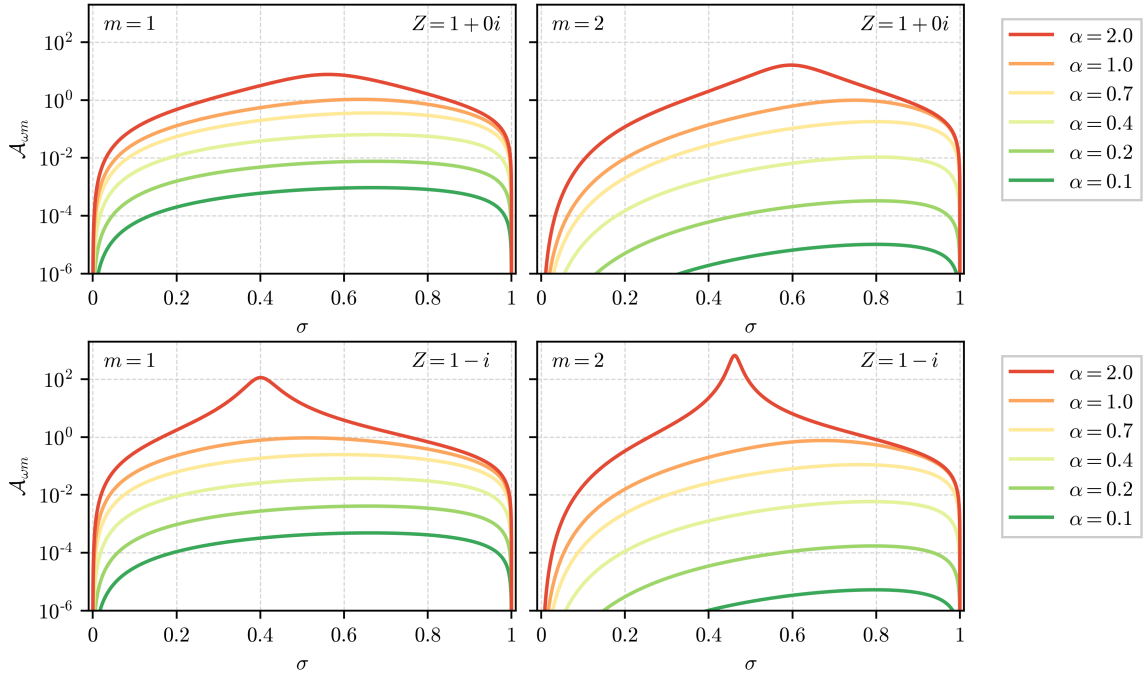


Figure 3.2: Amplification factor (3.36) the two azimuthal modes  $m = 1$  (left column) and  $m = 2$  (right column) for several rotation speeds and a cylinder impedance  $Z = 1 + 0i$  (top row) and  $Z = 1 - 1i$  (bottom row). The lack of an imaginary part suppresses the amplification peak (top row).

For certain parameters, the scattering ratio can become singular or completely vanish. These two limits correspond to the poles and zeros of the equation (3.39) and are associated with scenarios where an incoming pulse is completely absorbed or infinitely amplified, respectively. The corresponding set of parameters can be obtained by equating the numerator and denominator to zero. For the former, the associated impedances are given by

$$Z_m^{abs}(\omega) = \frac{2(1 - 1/\sigma)\phi_m^-}{i(\phi_{m-1}^- - \phi_{m+1}^-)}, \quad (3.40)$$

where again all quantities are evaluated at (3.38). If we focus on purely oscillating frequencies ( $\text{Im}(\omega) = 0$ ) we can think of this equation as parametrically defining a curve in the  $\text{Re}(Z)$  vs  $\text{Im}(Z)$  space, depicting values of impedance for which an incoming wave is completely absorbed.

For the static case ( $\sigma \rightarrow \infty$ ) the curves parametrized by (3.40) are presented in figure 3.3 for several values of the azimuthal mode  $m$ . The increase of  $m$  is accompanied by a “stretching” of the absorption curve towards higher impedance values. The parametrization is done in terms of the field frequency  $\omega \in [0, \infty]$  and the curve is traced from the origin  $Z = 0$  to the point  $Z = 1 + 0i$ .

If one wishes to absorb all the radiation with a specific frequency  $\omega$ , designing a cylinder with impedance given by (3.40) will get the job done. Similarly, the impedances for which the field gets infinitely amplified are given by

$$Z_m^{amp}(\omega) = \frac{2(1 - 1/\sigma)\phi_m^+}{i(\phi_{m-1}^+ - \phi_{m+1}^+)}, \quad (3.41)$$

that has the exact same form as (3.40) but with Hankel functions of the first kind replaced by second kind ones. This implies that both curves are related through

$$Z_{abs} = -(Z_{amp})^*, \quad (3.42)$$

corresponding to a reflection of the curves on the complex plane with respect to the  $\text{Re}[Z] = 0$  line.

For the static case then, we have no impedances with real part for which the field gets infinitely amplified (see figure 3.3). In contrast, for all  $m$  modes but the  $m = 0$  one, solutions with a real impedance start to exist. An example of how the parametric curves change as the rotation of the cylinder is increased can be seen in figure 3.4 for the  $m = 2$  mode.

The parametrization of these curves is very similar to what was stated before. Like then the absorption curve (solid line) point  $Z = 1 + 0i$  corresponds to the high frequency limit  $\omega \rightarrow \infty$ . As the frequency is lowered, the curve is traced until the origin is reached for the critical frequency  $\omega = m\Omega$ .

For frequencies below this threshold, the total absorption lines are parametrized in the  $\text{Re}[Z] < 0$  region and hence stop having an appropriate physical meaning. Due to relation (3.42), however, this part of the curve corresponds to the reflected form of the amplification with respect to the  $\text{Re}[Z] = 0$  line (dashed lines), that are traced from the origin (with

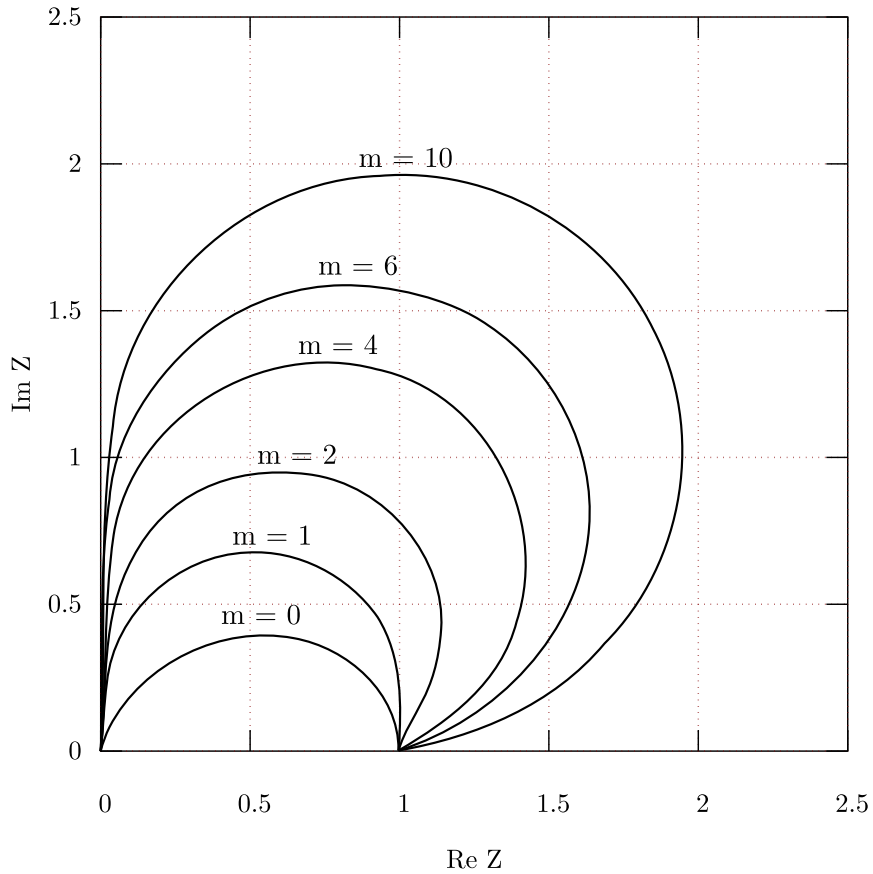


Figure 3.3: Absorption curves (3.40) for several azimuthal modes  $m$ . The parametrization path starts at the origin with  $\omega = 0$  and ends at  $Z = 1 + 0i$  when  $\omega \rightarrow \infty$ .

$\omega = m\Omega$ ) to a point in the imaginary axis (corresponding to  $\omega = 0$ ) whose coordinates are

$$\lim_{\omega \rightarrow 0} Z_m^{amp}(\omega) = -i\Omega. \quad (3.43)$$

If we drop the restriction of considering purely real frequencies and allow either growing modes ( $\text{Re}[\omega] > 0$ ) or damped ones ( $\text{Re}[\omega] < 0$ ), the curves traced will be different. Regarding this fact, a correction to [1] must be made. In the article, the authors claim that the curves (3.41) (dashed lines in figure 3.4) divide the complex plane into impedances for which the poles of (3.39) are unstable (region contained between the  $\text{Re}[Z] = 0$  line and the parametric amplification curve) or stable (outside region). Using (3.41), however, it is easy to show that there exist stable modes in the first region. Take for example a frequency  $\omega = 0.2 - 0.5i$  (a stable mode). The associated impedance for a cylinder rotating with angular velocity  $\Omega = 2$  is, by (3.41),  $Z \approx 0.16 - 1.76i$  - clearly inside region I (see figure 3.4).

The key point to retain from this section is that the scattering amplitudes off fluid waves from rotating (uniform) cylinders is very easily described mathematically. Amongst the most

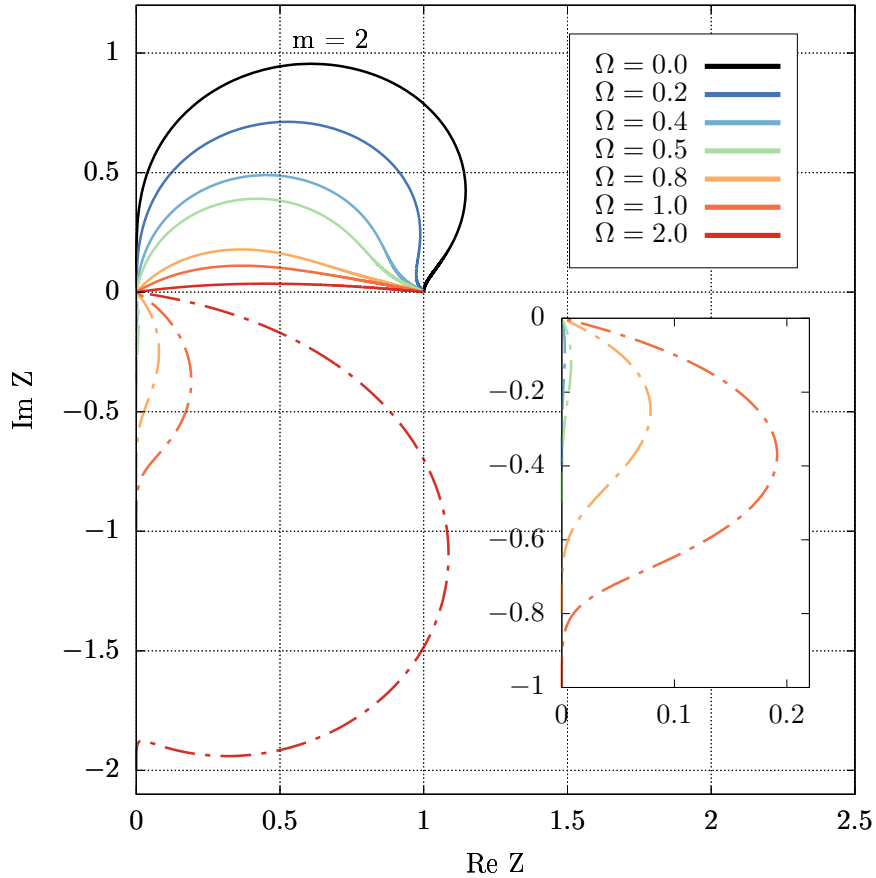


Figure 3.4: Absorption and amplification curves (3.40) and (3.41), respectively, for the  $m = 2$  azimuthal mode and several rotation speeds. The solid lines correspond to the absorption curves while the dashed lines to amplification ones. For a description of how these curves are parametrized see the main text.

particular features of this system, one has the observation of superradiant scattering for both subcritical and supercritical rotating cylinders and the existence of characteristic impedances for which waves are totally absorbed or infinitely reflected.

### 3.3.3 The Acoustic Bomb

The repeated scattering of waves can give rise to instabilities. It is thus particularly interesting to consider our fluid to be confined near the rotating cylinder by means of a reflective wall at a certain distance from it.

Besides being easier to setup such system in a lab, the imposed boundary conditions may correctly model the dynamics of massive scalar fields in astrophysical scenarios (as reasoned in chapter 2).

Mathematically, imposing a new boundary condition at a certain radius  $R_c$ , turns the scattering problem of last section into an eigenvalue one. To find the eigenfrequencies we

take the general solution written in terms of the Bessel functions

$$\psi(t, r, \varphi, z) = \sum_m \left[ \mathcal{C}_1 J_m \left( \frac{\omega r}{c} \right) + \mathcal{C}_2 Y_m \left( \frac{\omega r}{c} \right) \right] e^{-i\omega t + im\varphi}, \quad (3.44)$$

and force the solution to vanish at the cavity radius  $\Psi(r = R_c) = 0$ . This new boundary condition, along side with the one at the cylinder's surface, allows us to write an eigenvalue equation

$$\frac{(1 - 1/\sigma)J_m + iZJ'_m}{(1 - 1/\sigma)Y_m + iZY'_m} = \frac{\hat{J}_m}{\hat{Y}_m} \quad (3.45)$$

where  $\sigma = \omega/m\Omega$  is defined as before and the primes represent derivatives with respect to the dimensionless parameter  $y$  (see equation (3.24)). The functions on the LHS are to be evaluated at the cylinder's radius  $R_i$  and the hats on the RHS mean that these functions must be evaluated at the cavity radius  $R_c$ .

The solutions to this last equation (i.e., the frequencies  $\omega$  for which the relation (3.45) is satisfied) will generically be complex values

$$\omega = \omega_R + i\omega_I, \quad (3.46)$$

where the real part is associated with the field oscillation in time and the imaginary one with either its growth ( $\omega_I > 0$ ) or decay ( $\omega_I < 0$ ). No direct analytical way of finding these frequencies exists so we must resort to numerical methods. The methods employed are thoroughly explained in the *Mathematica* notebooks associated with this document (see appendix A) and thus we only summarize the procedure here.

Given any set of parameters ( $R_{BH}, R_c, \Omega, Z$ ), one can find the eigenfrequencies by considering a set of uniformly spaced frequencies in the complex plane that serve as initial seeds for *Mathematica*'s internal root finding algorithm. In most scenarios, this procedure gives us the natural frequencies sought with great accuracy.

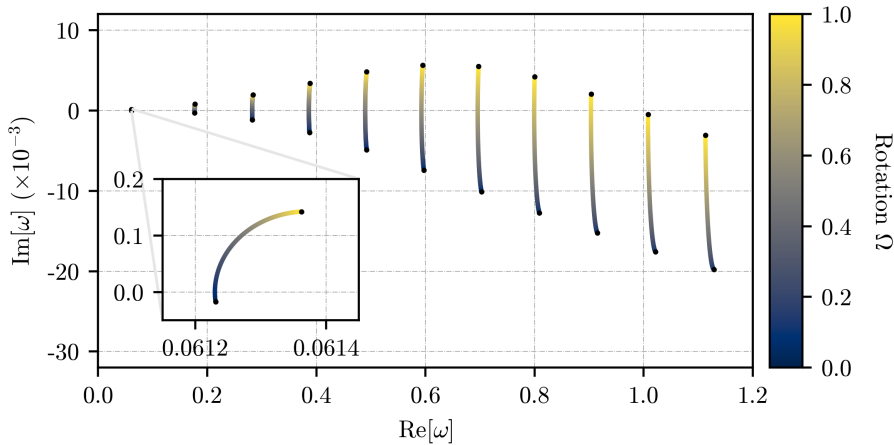


Figure 3.5: Acoustic bomb eigenfrequency (3.45) evolution in the complex plane as the rotation of the inner cylinder is increased for the azimuthal mode  $m = 1$ . The cylinder has radius  $R_i = 1$  and purely real impedance  $Z = 1$ . The cavity size is fixed at  $R_c = 30$ .

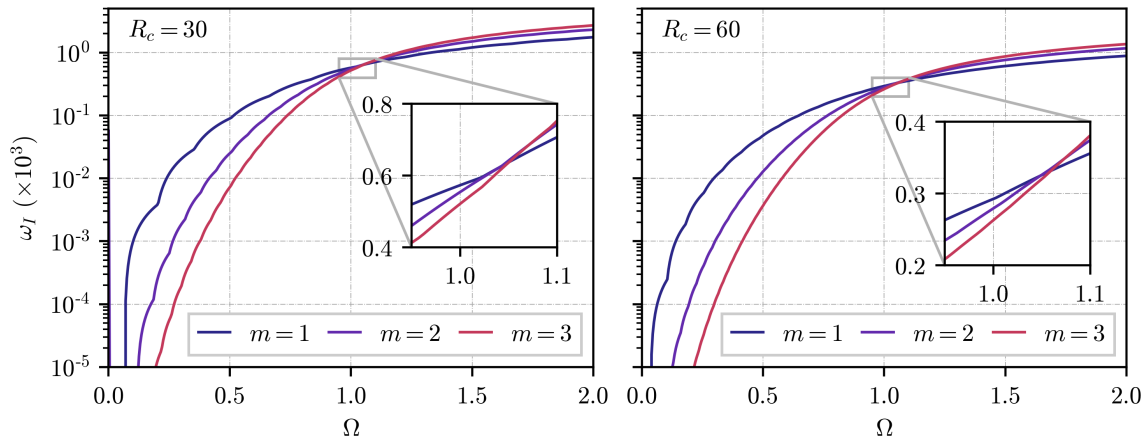


Figure 3.6: Maximum growth rate dependence on the angular velocity of the cylinder for the first 3 azimuthal  $m$  modes and 2 distinct cavity sizes. The inner cylinder has radius equal to unity and purely real impedance  $Z = 1 + 0i$ .

To study the parameter space efficiently, however, the repeated application of this last procedure is very inefficient. It is thus preferential to run it once, find a particular set of roots, and then use them as the new seeds as the parameters are slowly changed.

In this manner, the motion of the eigenfrequencies in the complex plane can be traced. A typical example of this method is displayed in figure 3.5. The initially found roots are marked as black dots with negative imaginary part. As the rotation  $\Omega$  is increased, they move up until they cross the  $\text{Im}[\omega] = 0$  line. This occurs precisely when the real part of that same solution obeys the superradiant threshold condition  $\text{Re}[\omega] = m\Omega$ , separating the growing modes from the non-growing ones.

An important aspect of the root structure of (3.45) is that, in general, the fastest growing mode (corresponding to the root with larger imaginary part) is not the one whose real part is closer to the superradiant threshold. This is mostly dependent on the real part of the impedance as one can make the faster growing mode approach the superradiant limit by increasing  $\text{Re}[Z]$ .

Note that in (3.45) the cylinder's radius  $R_i$  and the cavity size  $R_c$  enter the arguments of two distinct Bessel functions and so one cannot use the variable  $R_i/R_c$  to probe all possible problem scales. The vastness of parameter space makes it hard to get a complete and generic picture of the behaviour of the system and thus we shall restrict our analysis by fixing  $R_i = 1$  and changing the cavity radius as needed. We also restrict the results presented a cylinder with purely real impedance since no significant difference exists by considering a complex impedance.

Figure 3.6 shows how the maximum growth rate  $\omega_I^{max}$  changes as the cylinder's angular velocity increases. The wiggly behaviour of  $\omega_I^{max}$  is due to the change in the real part of the associated root (see figure 3.5). For the subcritical case ( $\Omega < 1$ ) the larger the azimuthal mode  $m$ , the smaller the instability growth rate. However, for most supercritical cases ( $\Omega > 1$ ), the inverse is observed. The insets show the points at which the transition occurs, making it evident that it is not coincident with the critical value of  $\Omega = 1$ .

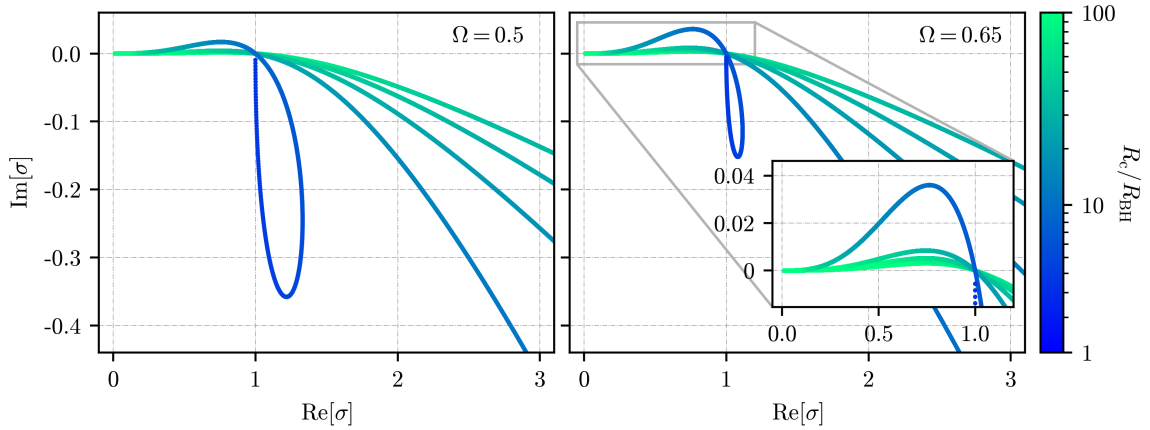


Figure 3.7: Motion of the eigenfrequencies of (3.45) corresponding to the 5 lowest energy modes as a function of the cavity radius for a cylinder of radius  $R_{\text{BH}} = 1.0$  and real impedance  $Z = 1.0 + i0$  for the  $m = 1$  case. The observed loop as the cavity is closed upon the cylinder was not presented in [1]. As the rotation of the cylinder is increased, as expected, the growth rate of associated modes increases. In the critical regime  $\Omega = 1$ , the lowest energy root never acquires a negative growth-rate.

Another evident feature observed in figure 3.6 is that having a larger cavity quenches the instability growth rate. The interpretation of this result as product of the time taken by a radially travelling pulse inside the cavity, leads to the conclusion that the typical timescales of the instability should behave as  $\sim 1/R_c$ . For large cavities, just like what was seen for BHs in chapter 2, this behaviour is also observed (see figure 3 of [1]).

There is, however, a limit to how small the cavity can be before the instability is completely quenched. To understand how exactly the size of the cavity affects the system's eigenfrequencies, we considered the five roots with smallest real part for a given set of parameters (see figure 3.5) and traced their path in the complex plane as the cavity size was varied. The results are presented in figure 3.7. The parameter  $\sigma = \omega/\sigma\Omega$  was used once more to ease the comparison with our previous results and with reference [1].

Comparing the left plot of figure 3.7 with figure 4 of [1] we see a rather interesting feature that went unnoticed previously. Generally, for small cavity sizes, all roots present both large oscillating frequencies as well as large, negative growth rates, meaning that, for sufficiently small cavities, all modes are damped in time and no instability is expected. As the size of the cavity is increased, the roots approach the superradiant threshold value  $\text{Re}[\sigma] = 1$  and start having a positive growth rate from that point onward. It is interesting that this generic behaviour is not observed for the lowest energy mode. Unlike the remaining roots, as the cavity size is decreased, it reaches a minimum amplification coefficient (maximizing the damping of the mode) and starts increasing again. As the cavity wall approaches the cylinder's surface, the eigenfrequency of the lower energy mode approaches the superradiant value  $\omega = m\Omega$ . From the parameters probed, this feature seems to be generic to other azimuthal modes and cylinder impedances.

The above behaviour of the eigenfrequencies seems to remain true as the angular velocity of the cylinder is changed, hinting at a fundamental feature of the system.

The above analysis, complementing the previous results of [1], puts superradiance of such a simple setup on firm grounds. We will return to how exactly this could be observed in earth-based experiments at the end of this chapter.

## 3.4 Non-Uniform Cylinder

As the last section showed, the dynamics of a fluid perturbations interacting with a rotating uniform cylinder are rich and not trivially probed. Our main objective, however, is to understand how adding an asymmetry to the systems, affects our previous results. This is done by considering a non vanishing asymmetry parameter  $\epsilon$  in (3.14) and extract how the geometry of such systems shape the dynamics of the perturbations.

### 3.4.1 Scattering factors

Just like before, we can consider the travelling wave solution (3.23) and try to relate the amplitudes of the incoming and outgoing waves. In fact, the relation between the coefficients is the same as (3.37) only now the impedance has a non trivial angular dependence that explicitly reads

$$\tilde{Z} = \tilde{Z}_0 [1 + \epsilon \cos^2(\varphi)] = \tilde{Z}_0 \left[ 1 + \epsilon \left( \frac{1}{2} + \frac{e^{i2\varphi} + e^{-i2\varphi}}{4} \right) \right]. \quad (3.47)$$

The dependence on the azimuthal angle  $\varphi$ , has the effect of coupling different  $m$ -modes. Considering the case of a static cylinder ( $\Omega = 0$ ) and using the rewritten form of the impedance (3.47), the equation relating the coefficients (3.37) now reads

$$\begin{aligned} \sum_m \mathcal{A}_+^m [\phi_m^+ - i\tilde{Z}_0 (\phi_m^+)' ] + \mathcal{A}_-^m [\phi_m^- - i\tilde{Z}_0 (\phi_m^-)' ] = \\ = \sum_m \epsilon \left( \frac{i\tilde{Z}}{2} \right) \left[ \mathcal{A}_+^m (\phi_m^+)' + \mathcal{A}_+^{m+2} (\phi_{m+2}^+)' + \mathcal{A}_+^{m-2} (\phi_{m-2}^+)' \right] + \\ + \sum_m \epsilon \left( \frac{i\tilde{Z}}{2} \right) \left[ \mathcal{A}_-^m (\phi_m^-)' + \mathcal{A}_-^{m+2} (\phi_{m+2}^-)' + \mathcal{A}_-^{m-2} (\phi_{m-2}^-)' \right], \end{aligned} \quad (3.48)$$

where again all functions are to be evaluated at the cylinder's radius. This infinite set of algebraic equations relates all incoming and outgoing amplitudes. Note that, in the symmetric case ( $\epsilon = 0$ ) the system reduces to the already studied equation (3.39). A better way of understanding the effect of the asymmetry is to write (3.48) in the matrix form

$$\mathbf{M}_+ \psi_+ + \mathbf{M}_- \psi_- = 0 \quad (3.49)$$



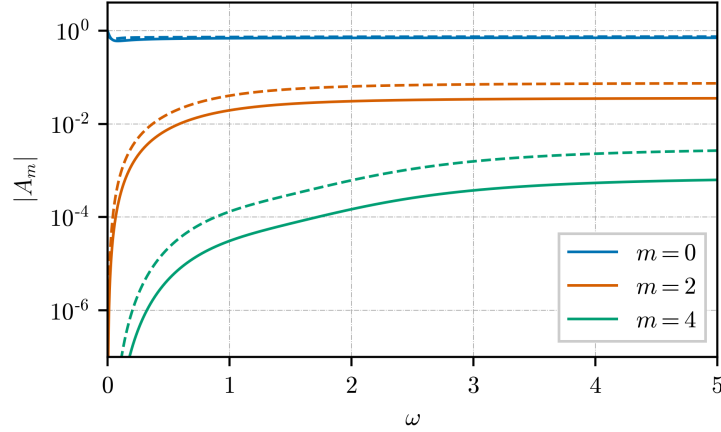


Figure 3.8: Scattering amplitudes for an asymmetric cylinder of size  $R = 1$  with  $\epsilon = 0.25$  (solid line) and  $\epsilon = 0.5$  (dashed line) obtained from the truncation of (3.52) at  $m = 8$ .

the presented case), with a contribution of higher modes of equal parity. The most evident feature is that an increase in the asymmetry parameter, translates itself into larger reflected amplitudes of all coupled modes. This is in accordance with our physical picture since a larger asymmetry is expected to enhance mode coupling.

The mode mixing observed seems to be most prominent for high frequency fields and that low frequency waves are essentially reflected. This is also evident from the definition of matrix elements (3.51) since in the low frequency limit, the off diagonal parameters in the matrix equation (3.52) can be seen to vanish.

Since the initial mode is an  $m = 0$  pulse, the coupling is most important for the  $m = \pm 2$  modes. This is also evident from the RHS of (3.52). Considering only this coupling, i.e., ignoring higher  $|m| > 2$  modes, we can find the explicit amplitudes for the  $m = 0$  and  $m = 2$  scattered waves

$$|\mathcal{A}_+^0|^2 = \left| \frac{\Lambda_-^0 \Lambda_+^2 - 2\beta_-^0 \beta_+^2}{\Lambda_+^0 \Lambda_+^2 - 2\beta_+^0 \beta_+^2} \right|^2, \quad (3.53)$$

$$|\mathcal{A}_+^{\pm 2}|^2 = \left| \frac{\Lambda_+^0 \beta_-^0 + \Lambda_-^0 \beta_+^0}{\Lambda_+^0 \Lambda_+^2 - 2\beta_+^0 \beta_+^2} \right|^2.$$

Note that the above expressions give the scattering amplitudes of a static uniform cylinder (3.39) when  $\epsilon \rightarrow 0$ .

The scattering amplitudes here obtained concern a static asymmetric cylinder. Taking into account the rotation of such cylinder makes it extremely hard to find an analytical relation between the amplitudes from equation (3.48). The mode mixing here observed should, however, also be present in such case, allowing the amplification of higher modes by the repeated scattering of such perturbations.

### 3.5 A Numerical approach

Since no clear analytical results can be obtained for the case of an asymmetric rotating cylinder, one is forced to take a numerical approach to the problem. By numerically integrating the Klein-Gordon equation (3.13) with the appropriate boundary conditions, we can study the cylinder model in its generality and confirm the previously obtained analytical predictions.

The KG equation was numerically integrated using the `Zilindroa` numerical package. This specifically designed code was written in the Julia Programming language [58] and is freely available in [59]. The code solves an altered version of the 2 dimensional wave equation in polar coordinates  $(r, \varphi)$

$$\frac{\partial^2 \psi}{\partial t^2} = c^2 \left[ \frac{1}{r} \frac{\partial}{\partial r} \left( r \frac{\partial \psi}{\partial r} \right) + \frac{1}{r^2} \frac{\partial^2 \psi}{\partial \varphi^2} \right]. \quad (3.54)$$

By using  $\psi(r, \varphi) = \phi(r, \varphi)/\sqrt{r}$  the wave equation becomes

$$\frac{\partial^2 \phi}{\partial t^2} = \frac{\partial^2 \phi}{\partial r^2} + \frac{1}{r^2} \frac{\partial^2 \phi}{\partial \varphi^2} + \frac{\phi}{4r^2}. \quad (3.55)$$

and the boundary condition (3.31) imposed at the cylinder's radius reads

$$\frac{\partial \phi}{\partial t} = Z \left[ \frac{\partial \phi}{\partial r} - \frac{\phi}{2r} \right] - \Omega \frac{\partial \phi}{\partial \varphi}. \quad (3.56)$$

To consider the system enclosed in a cavity, the field is forced to zero  $\psi = 0$  at the cavity radius.

The code integrates the above equation by using the method of lines on a polar grid with second-order accurate operators for the discretization of the spatial derivatives and a fourth order Runge-kutta scheme provided by the `DifferentialEquations.jl` Julia package [60]. For a detailed discussion of the numerical methods and the convergence of our code, we refer the reader to appendix C.

For all simulations, the initial conditions are of an inward travelling gaussian pulse

$$\begin{aligned} \phi(t = 0, \mathbf{r}) &= \phi_0 = A \cos(m\varphi) \sin(\omega r) e^{-\frac{1}{2} \left( \frac{r-r_0}{\sigma} \right)^2}, \\ \partial_t \phi(t = 0, \mathbf{r}) &= \partial_r \phi_0, \end{aligned} \quad (3.57)$$

where  $r_0$ ,  $\sigma$ ,  $\omega$  represent the initial radius, width and frequency of the pulse, respectively.

The lack of mode mixing in the case of a uniform cylinder and its inevitability in the assymmetric scenario can be numerically confirmed by decomposing the field in azimuthal modes at a specific radial coordinate

$$\phi(t, r, \varphi) = \sum_m \phi_m(t, r) \cos(m\varphi), \quad (3.58)$$

Table 3.1: Parameters used for the initial pulse configuration (3.57).

ID	$A$	$r_0$	$\sigma$	$\omega$	$m$
S1	3.5	40.0	4.0	1.28	0
S2	3.5	15.0	2.0	0.1	2

where the coefficients  $\psi_m$  are given by

$$\phi_m(t, r) = \frac{1}{\pi} \int_0^{2\pi} \phi(t, r, \varphi') \cos(m\varphi') d\varphi'. \quad (3.59)$$

We performed an extensive set of simulations with distinct initial conditions. Since no clear dependence seems to exist on the initial pulse shape (apart from the azimuthal mode  $m$ ) we present here the simulations for a pulse with the parameters shown in table 3.1. The set labelled S1 was considered to study the scattering amplitudes of a monochromatic pulse of an asymmetric cylinder while the S2 set was used to study the natural modes of a cavity of size  $R_c = 38$ .

### 3.5.1 Scattering amplifications for a static cylinder

The numerical setup allows the scattering amplitudes obtained from the matrix equation (3.52) to be compared against the numerical simulations. To do so, we considered a travelling pulse with the S1 set of parameters (see table 3.1) and evaluate its Fourier components before and after a single interaction with an asymmetric cylinder.

The comparison between the numerical data and the analytical calculations can be seen in figure 3.9. The cylinder considered has radius  $R_1 = 1$ , impedance  $Z = 0.2$  and asymmetry parameter  $\epsilon = 0.25$ . The left plot represents the Fourier components of the field at  $r = 20$ .

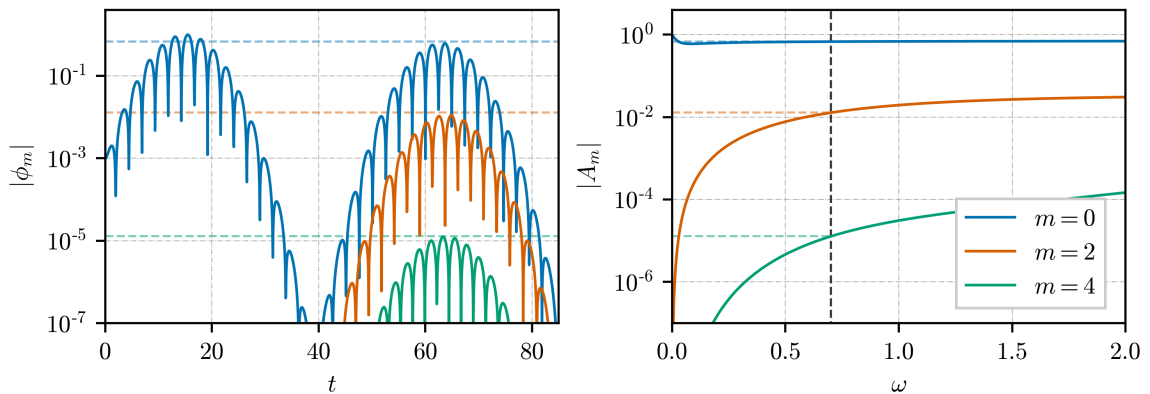


Figure 3.9: Comparison of the scattering amplitudes obtained by solving the matrix equation (3.52) (right plot) with the numerically obtained evolution of the azimuthal Fourier components of a reflected pulse (left plot). The inner cylinder has radius  $R_i = 1$ , impedance  $Z = 0.2$  and asymmetry parameter  $\epsilon = 0.25$ . The dashed lines represent the expected scattering amplitudes for  $\omega = 0.64$ .

After interacting with the cylinder, the initially  $m = 0$  pulse acquires higher mode components of equal parity ( $m = 2, 4, \dots$ ). The right plot displays the scattering amplitude ratios obtained by solving the matrix equation (3.52). The reflected pulse components seem to agree quite well with the amplitude ratios associated with half the frequency of the initial pulse  $\omega/2 = 0.64$ .

### 3.5.2 Static cylinder inside a cavity

Studying repeated reflections of the initial pulse inside the cavity, we can compare our results with the analytically obtained cavity eigenfrequencies. The procedure is the same as before, but the governing equations are evolved over a much longer time period. We considered the pulse with the S2 set of parameters (see table 3.1) inside a cavity of size  $R_c = 38$  with a static cylinder  $\Omega = 0$  with impedance  $Z = 0.2$ .

The Fourier components of the field at  $r = 20$  are displayed in Figure 3.10 for the case of a uniform (left plot) and non-uniform cylinder with  $\epsilon = 0.25$  (right plot).

The feature that stands out comparing the two simulations is the observation of mode mixing in the asymmetric case. Like in the single scattering simulations, we see the excitation of higher field modes of equal parity. Note that in this case we considered an initial  $m = 2$  pulse.

Regardless of the asymmetry, both pulses decay in time with small decay rates, allowing the pulse to live inside the cavity for long simulation times.

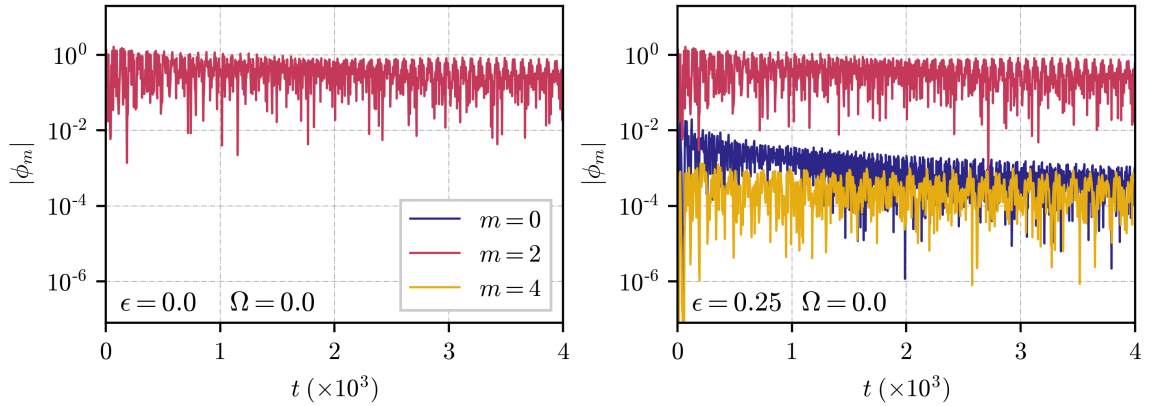


Figure 3.10: Fourier components of an initial gaussian wave pulse with parameters S2 (see table 3.1) interacting with a static uniform cylinder (left) and a static asymmetric cylinder (right). The field is confined inside a cavity of size  $R_c = 38$  and the cylinder has radius  $R_i = 2$  and impedance  $Z = 0.2$ . The asymmetric case (right) has  $\epsilon = 0.25$ .

### 3.5.3 Rotating cylinder inside a cavity

The same analysis can be performed when the cylinder is rotating. The Fourier components of the field in this scenario is presented in figure 3.11. The dashed line corresponds to the growth rate obtained by solving equation (3.45). Like before, the comparison of this growth

rate with the numerical results is only possible for the uniform cylinder case (left plot). The agreement displayed was verified for all simulations performed.

The asymmetric case displays several interesting features that should be pointed out. Firstly, like in the static case (see right plot of figure 3.10), the presence of higher equal parity modes is observed. These modes are seen to have growth rates similar to that of the initial  $m = 2$  mode that dominates the simulation throughout. Secondly, the dominant mode grows slower in the case of an asymmetric cylinder when compared with that of a uniform one. On physical grounds, this is expected since energy is being distributed amongst higher  $m$  modes.

The difference between the two scenarios is, however, small and the field is expected to grow on similar timescales in both scenarios. The growth rates for the simulations shown are presented in table 3.2.

The growth rate for the non-uniform cylinder were obtained by a late time linear fit of the field Fourier components shown in figure 3.11. The growth rates of the individual modes are all of comparable magnitude but smaller than the growth rate of the pulse when a symmetric cylinder is considered.

Table 3.2: Growth rate comparison for the simulations presented in figure 3.11 for a pulse interacting with a rotating cylinder  $\Omega = 0.35$ . The uniform cylinder roots were obtained from the eigenvalue equation (3.39), while the non-uniform scenario were obtained from a late fit to the field components at  $r = 20$ .

mode	$\epsilon = 0$ (analytical)	$\epsilon = 0.25$ (numerical)
0	0	$3.17420 \times 10^{-3}$
2	$3.36746 \times 10^{-3}$	$2.94818 \times 10^{-3}$
4	0	$3.07155 \times 10^{-3}$

## 3.6 Superradiance in Laboratory

As pointed out by the authors of [1], the relatively simple model of a uniform cylinder and the analytical calculations performed in the original manuscript made clear that superradiance could be observed experimentally in carefully crafted setups using surface waves as the perturbations.

Amongst the reasons to consider surface waves, lies the fact that these are not dispersive. In particular, if one takes a tank of water of depth  $h$ , we have

$$\frac{\omega}{k} = \sqrt{gh}, \quad (3.60)$$

where  $g$  is the gravitational acceleration. If one considers a tank with  $h = 0.5$  m, one has  $c = \omega/k = 2$  ms<sup>-1</sup>. Considering then a inner cylinder of size  $R_1 = 0.2$  m inside a cavity of size  $R_c = 3.8$  m, the growth rates presented in table 3.2, tell us that the instability timescale

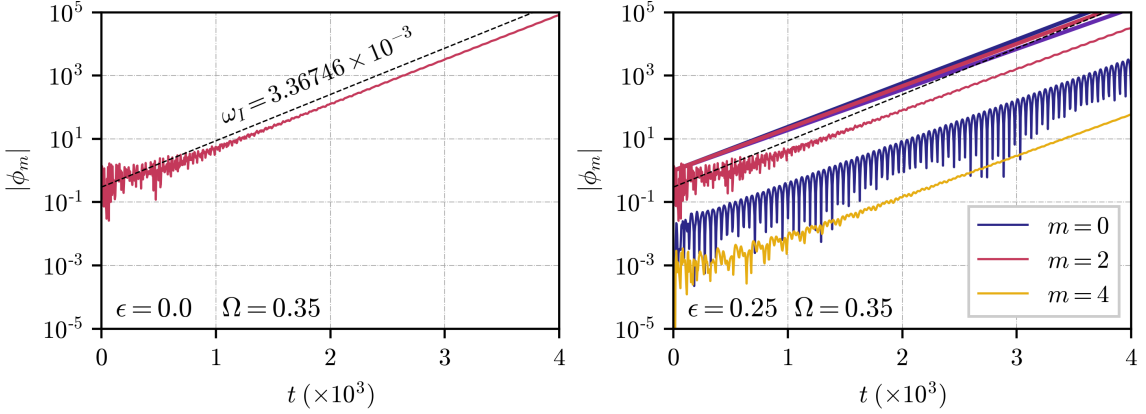


Figure 3.11: Fourier components of an initial gaussian wave pulse with parameters S2 (see table 3.1 interacting with a static uniform cylinder (left) and a static asymmetric cylinder (right). The field is confined inside a cavity of size  $R_c = 38$  and the cylinder has radius  $R_i = 2$ , impedance  $Z = 0.2$  and angular velocity  $\Omega = 0.35$ . The asymmetric case (right) has  $\epsilon = 0.25$ .

of the order of

$$\tau = \frac{R_c}{\omega_I c} \sim 400 \text{ s} \sim 6 \text{ minutes} . \quad (3.61)$$

The velocity of the cylinder in this case would be  $v/c = \Omega R_1/c \sim 0.02$  - below the subsonic regime. The above timescale, however, is only expected for a specific cylinder impedance.

The remarkable feature to point out is that these timescales do not change enormously by considering an asymmetric cylinder, pointing to the fact that the mode-mixing expected on theoretical (and numerical) grounds is also expected to be observed in actual experimental setups.

In fact, shortly after the publication of [1], superradiance was detected in a laboratory [61]. Using surface waves, it was shown that perturbations on the surface of the water were scattered off a water vortex in a superradiant fashion. Despite the different experimental setup, the observable amplification of waves by rotating bodies brought superradiance from being a theoretical curiosity to a subject viable for experimental study. More recent experiments have observed superradiant scattering in acoustic and optical mediums [53, 62] corroborating the universality of the phenomenon.

It should be mentioned that our analysis does not aim at exploring the feasibility of an experimental setup to study the effects of a asymmetry in superradiant setups but instead to understand what are the main features that distinguish the two systems and what signatures does it leave on the interacting field.

The most evident feature, found in the case of a static asymmetric cylinder and translated to the rotating scenario, is the mixing of field azimuthal modes with the same parity of the initial pulse.

Remarkably, the asymmetry parameter does not strongly quench the instability rate of the acoustic bomb setup and that the associated timescales are of similar magnitude. Although the initial mode in the cavity dominates the dynamics throughout, the equal parity modes

grow in similar timescales.

Besides extending the work of [1] (making it easy to extend the experimentally envisioned setup), the simple model here considered points to the remarkable feature that asymmetric setups are also prone to superradiant scattering and instabilities.

## Chapter 4

# Toy Model II

In chapter 3 we saw that, adding an asymmetry to a system where superradiance is known to occur, does not quench the appearance of instabilities. Such system is, however, not easily mapped to that of an actual astrophysical scenario – our ultimate goal.

On one hand, no clear connection between the toy model parameter (impedance, density,...) and those characteristic of astrophysical objects. On the other, unlike in binary systems, the cylinder model represents a single connected body.

A plethora of physical setups are, however, composed of disconnected bodies. This includes not only astrophysical binaries bound by the gravitational interaction and evolving via gravitational-wave emission, but also Earth-bound systems, such as spinning blades encountered in a variety of machinery [63].

Can superradiant instabilities occur in such non axisymmetric binary systems? If so, on which timescales? In this chapter we push our understanding of superradiance in asymmetric systems by considering a toy model that more closely represents the structure of actual binary systems.

The chapter is based on the publication [64] with Prof. Vitor Cardoso and Dr. Miguel Zilhão, containing some results that did not make it to the final manuscript.

### 4.1 Modelling absorption in KG equation

All systems where superradiance has been observed have one important aspect in common - they possess internal degrees of freedom where energy can be dumped into. In a BH, this dissipation is intrinsically built in by means of the one-way null-surface that is the event horizon.

In the cylinder model of chapter 3 the dissipation was modelled directly by the existence of a impedance with positive real part.

Modelling dissipation can be done in several distinct ways. Like in the BH case, it can be done directly through the coupling of the scalar field with space-time or indirectly by considering instead its coupling with microscopic degrees of freedom of the medium where the field propagates. Zeldovich's seminal work [65] presents us with a simple model of the

latter kind by adding a dissipative term to the KG equation

$$(\square - \mu^2)\Psi = \alpha \frac{\partial \Psi}{\partial t}, \quad (4.1)$$

where  $\alpha > 0$  describes dissipation on a timescale  $\tau \sim 1/\alpha$  in the frame where the absorbing region is static. In connection with particle physics, we can associate the parameter with the mean free path of the particle our field described in a given medium (e.g. a star)

$$\alpha = \frac{1}{l} = n\sigma, \quad (4.2)$$

where  $n$  is the number of particles per unit volume of the star and  $\sigma$  the cross-section associated with the interaction. By using the star mass  $M$ , density  $\rho$  and nucleon mass  $m_N$ , we can write

$$M\alpha = \frac{GM\rho\sigma}{c^2 m_N} \sim 0.92 \frac{\rho}{1 \times 10^{15} \text{ Kg m}^{-3}} \frac{M}{M_\odot} \frac{\sigma}{1 \times 10^{-41} \text{ cm}^2}, \quad (4.3)$$

that can be of order 1 for certain dark matter candidates [66].

As an example, solar mass neutron stars ( $M = 3 - 10 M_\odot$ ) have typical densities of order  $\rho \sim 1 \times 10^{17} \text{ kgm}^{-3}$ , leading to absorption timescales for such candidates of

$$\tau = \frac{1}{\alpha} \sim M \approx (15 \text{ km}) \xrightarrow{\times c^{-1}} \tau \approx 1 \times 10^{-5} \text{ s}. \quad (4.4)$$

This phenomenological approach to model absorption has in fact been used successfully to show that superradiance is likely to occur in stars [2]. Neglecting the backreaction of the scalar field on the spacetime, the authors took the metric for a spherically symmetric rotating star in the LHS of equation (4.1) and added, for the region inside the star, the RHS with  $\alpha > 0$ . The results showed not only that superradiance is bound to occur, but also that it does so in the superradiant regime  $\omega < m\Omega$ , where  $\Omega$  is the angular velocity of the star.

The connection with particle physics breaks down when a BH is considered since no meaningful notion of free path exists for a particle inside a BH. Nonetheless, the existence of an absorbing membrane (and hence an effective cross section), allows us to say that the use of such system to model BH absorption implies that  $M\alpha$  should be of order unity [67].

The altered version of the KG equation (4.1) is not, unlike the homogeneous case, Lorentz invariant. By performing a local Lorentz transformation, the dissipative term becomes

$$\alpha \frac{\partial \Psi}{\partial t} \rightarrow \alpha \gamma \left( \frac{\partial \Psi}{\partial t} - \beta \frac{\partial \Psi}{\partial x} \right) \quad (4.5)$$

where  $\beta = v/c$  is the relative velocity of the moving frame and  $\gamma = \sqrt{1 - \beta^2}$ . In cylindrical coordinates we can take the field decomposition

$$\Psi = \phi(r) e^{i\omega t + im\varphi} \quad (4.6)$$

and make the Lorentz transformation to a frame rotating with angular velocity  $\Omega$ . This is

---

achieved by letting  $\beta = \Omega r/c$  and  $x = r\varphi$  in (4.5). With this the dissipative term becomes

$$\alpha \frac{\partial \Psi}{\partial t} \rightarrow i\alpha\gamma (\omega - m\Omega) \Psi, \quad (4.7)$$

meaning that, when  $\omega < m\Omega$ , the effective absorption parameter becomes negative, leading instead to amplification of the field.

## 4.2 Problem Setup

To model the binary, we consider two absorbing cylinders revolving around each other at frequency  $\Omega$  and at an orbital separation  $R_0$ . Mathematically, we can model the problem via Eq. (4.1) by assigning the absorption  $\alpha$  the values,

$$\alpha(t, \mathbf{r}) = \begin{cases} \alpha_0 & \text{if } (\mathbf{r} - \mathbf{R}_{\text{orbit}})^2 < R_a^2 \\ \alpha_0 & \text{if } (\mathbf{r} + \mathbf{R}_{\text{orbit}})^2 < R_a^2 \\ 0 & \text{otherwise} \end{cases}, \quad (4.8)$$

where  $\mathbf{R}_{\text{orbit}}$  defines the orbital radius of the two bodies and  $R_a = 2M$  is taken to be their radius (for definiteness, with a view on astrophysical compact binaries).

Because we eventually would like to extrapolate to gravitational systems, we take the  $\Omega$  and the orbital radius to be related through Kepler's law. We take the orbital radius to be given by  $\mathbf{R}_{\text{orbit}} = R_0 \cos(\Omega t)\mathbf{e}_x + R_0 \sin(\Omega t)\mathbf{e}_y$ , where  $\Omega$  is taken to be the nonrelativistic orbital period

$$\Omega = \sqrt{\frac{2M}{R_0^3}}. \quad (4.9)$$

In the above equation, like throughout our discussion, we have used geometrized units  $G = c = 1$ .

A schematic diagram of our setup is shown in figure 4.1. Although we focus on equal mass binaries, the model can easily be generalized.

Note also that the previous results concerning a single rotating cylinder can be accommodated setting  $R_0 = 0$  (with  $\Omega$  a free parameter). In this scenario, not only can we obtain analytical predictions, but a connection with previously studied models (including the one of chapter 3) can be made. This connection is presented in appendix D.

For the binary scenario ( $R_0 \neq 0$ ) the setup does not allow analytical predictions to be easily made and we must resort to numerical evolutions of the system. Even with a simple model as this it is computationally expensive to explore the problem in  $(3 + 1)$  dimensions so we focus on a  $(2 + 1)$  scenario. Since nothing intrinsic exists about lower dimensional spacetimes, we expect our results to have a counterpart in higher dimensions. We cannot, however, exclude the possibility that the confining geometry here considered plays a role in the dynamics of our system. Secondly, the generality of the model allows us to draw conclusions about a broader type of systems where the main feature is the clear lack of axial symmetry and thus understand the signature of the system's geometry in a confined field.

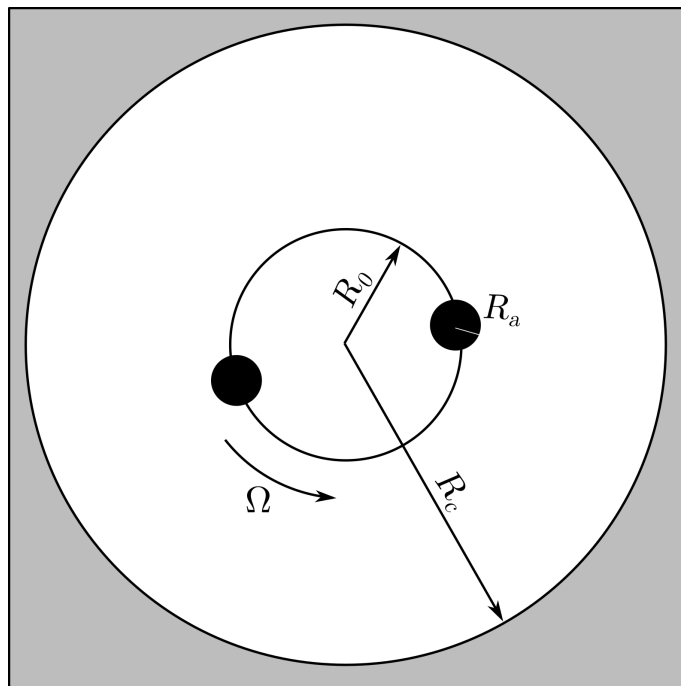


Figure 4.1: Schematic view of our computational domain, with the respective absorption regions (in black) and reflecting boundary condition at the cavity location,  $r = R_c$ . Thus, we consider a binary of equal objects, each with the same radius  $R_a = 2$ . They revolve around the geometric center on a circular orbit of radius  $R_0$  with frequency  $\Omega$  given by (4.9).

To ease our discussion, we will refer to the single absorption region scenario ( $R_0 = 0$ ) as the SA model while the general binary system ( $R_0 \neq 0$ ) as the BA model.

The governing Eq. (4.1) was numerically integrated with the aid of `BhAbs` (Black Hole Absorption Solver) numerical package. This specifically designed code was written in the Julia Programming language [58] and is freely available in Ref. [64].

Equation (4.1) is only valid in the frame where the absorbing regions are static so that one needs to perform a coordinate change to the lab frame. This is easily done through the coordinate change  $\varphi \rightarrow \varphi - \Omega t$ . This leads to the transformation of the time derivative as  $\partial_t \rightarrow \partial_t - \Omega \partial_\varphi$ , making our equation take instead the form

$$(\square - \mu^2)\Psi = \alpha \left[ \frac{\partial \Psi}{\partial t} + \Omega \frac{\partial \Psi}{\partial \phi} \right]. \quad (4.10)$$

For the time integration, our code implements the method of lines on a Cartesian grid with second-order accurate operators for the discretization of the spatial derivatives, and time integration performed with a fourth order Runge-Kutta scheme provided by the `DifferentialEquations.jl` Julia package [60]. For a detailed discussion of the numerical methods and the convergence of our code, we refer the reader to appendix C.

For all simulations presented, we take as the initial field configuration a purely ingoing Gaussian wave pulse,

Table 4.1: Initial conditions considered for the gaussian pulse (4.11). For the single rotating absorbing region we always used the same initial conditions (model SA). For the binary scenario we considered two sets of parameters whose main difference is the azimuthal mode  $m$  (models BA).

Model	$A$	$r_0$	$\sigma$	$\omega$	$m$
SA	3.5	15	2.0	0.1	2
BA1	3.5	15	2.0	0.045	2
BA2	5.0	35	3.5	0.045	1

$$\Psi(t = 0, \mathbf{r}) = \Psi_0 = A \cos(m\varphi) \sin(\omega r) e^{-\frac{1}{2}\left(\frac{r-r_0}{\sigma}\right)^2}, \quad (4.11)$$

$$\partial_t \Psi(t = 0, \mathbf{r}) = \partial_r \Psi_0,$$

where  $r_0$ ,  $\sigma$ ,  $\omega$  represent the initial radius, width and frequency of the pulse, respectively. For our simulations we considered the three distinct values for these quantities shown in Table 4.1. Due to the linearity of Eq. (4.1), the overall amplitude is irrelevant.

The energy density of the field inside the cavity

$$\epsilon = \frac{1}{V} \int [(\partial_t \Psi)^2 + |\nabla \Psi|^2] d\mathbf{x}, \quad (4.12)$$

was calculated using standard cubic interpolation (Simpson's 3/8 rule).

The single cylinder scenario allows us to obtain analytical expressions for the growth rate of a field confined inside the cavity so that a comparison with the numerical simulations is possible. This comparison is presented in section 4.3. The binary case does not gift us with such grace and we restrict ourselves to a purely numerical analysis of the simulations. These results are presented in Sec. 4.4.

Throughout this manuscript we take

$$M = 1, \quad R_a = 2, \quad \alpha = 10. \quad (4.13)$$

The first is a choice of scale. The second is chosen with an eye on astrophysical compact binaries (and as we said we will focus exclusively on setups with  $R_a = 2M$ ) and the third is an arbitrary choice (inspired again by BH physics [2]). These are only meant to be representative and to ease the discussion of our numerical results.

### 4.3 Isolated objects: scattering and superradiance

When there is a single spinning cylinder (i.e.,  $R_0 = 0$ ), an analytical solution of Eq. (4.1) can be obtained in terms of Bessel functions. In polar coordinates  $(t, r, \varphi)$ , we can use the usual field ansatz

$$\Psi(t, r, \varphi) = \frac{\phi(r)}{\sqrt{r}} e^{-i\omega t + im\varphi}, \quad (4.14)$$

to write the governing equation for the radial field  $\phi(r)$  as

$$\frac{\partial^2 \phi}{\partial r^2} + \left( \omega^2 + i\alpha(\omega - m\Omega) - \frac{m^2}{r^2} + \frac{1}{4r^2} \right) \phi = 0. \quad (4.15)$$

The above equation is a transformed version of the Bessel equation (compare with (3.17)) and hence allows us to write the general solution as

$$\Psi(t, r, \varphi) = [AJ_m(\beta_\alpha r) + BY_m(\beta_\alpha r)] e^{-i\omega t + im\varphi} \quad (4.16)$$

where  $J_m$  and  $Y_m$  denote the Bessel functions of the first and second kind, respectively, and  $\beta$  is defined as

$$\beta_\alpha^2 = \omega^2 + i\alpha(\omega - m\Omega). \quad (4.17)$$

The whole domain solution consists then of two separate versions of (4.16), one for each region defined that satisfy the appropriate boundary conditions. Explicitly we have

$$\Psi(r) = \begin{cases} [AJ_m(\beta_\alpha r) + BY_m(\beta_\alpha r)] e^{-i\omega t + im\varphi}, & \text{for } 0 \leq r \leq R_a \\ [CJ_m(\beta_0 r) + DY_m(\beta_0 r)] e^{-i\omega t + im\varphi}, & \text{for } R_a < r \leq R_c \end{cases} \quad (4.18)$$

The general solution must be regular at the origin, be continuously differentiable on the whole domain, and vanish at the cavity radius. The first constraint implies  $B = 0$  since the Bessel function of the second kind  $Y_m$  blows up at the origin. The last constraint will force our field to be confined inside the cavity and hence take a particular set of natural frequencies. If, however, we remove this last condition, we are able to study how waves are scattered off the absorbing region.

### 4.3.1 Scattering amplitudes

Having no outer boundary means that the field is not confined near the absorbing region. We are thus interested in finding solutions that take the form of a scattering problem,

$$\Psi(r \rightarrow \infty) \sim \mathcal{A}_+ e^{i\omega r} + \mathcal{A}_- e^{-i\omega r}, \quad (4.19)$$

at spatial infinity, with  $\mathcal{A}_\pm$  the amplitude of the outgoing and incoming waves, respectively. To satisfy this condition our solution outside the absorbing region should be written as

$$\Psi(t, r, \varphi) = [\mathcal{A}_+ \phi_m^+(\omega r) + \mathcal{A}_- \phi_m^-(\omega r)] e^{-i\omega t + im\varphi}, \quad (4.20)$$

where  $\phi_m^+ = J_m + iY_m$  and  $\phi_m^- = J_m - iY_m$  are the Hankel functions of the first and second kind respectively.

Using the two solutions forms (4.16) and (4.20) for the respective regions and requiring

continuity at the absorbing region surface we find,

$$\left| \frac{\mathcal{A}_+}{\mathcal{A}_-} \right|^2 = \left| \frac{(\phi_m^-)(J_m^\alpha)' - (\phi_m^-)'(J_m^\alpha)}{(\phi_m^+)(J_m^\alpha)' - (\phi_m^+)'(J_m^\alpha)} \right|^2, \quad (4.21)$$

where primes stand for derivative with respect to the radial coordinate and the functions  $J_m^\alpha = J_m(\beta_\alpha r)$  and  $\phi_m^\pm = \phi_m^\pm(\omega r)$  are evaluated at the boundary radius  $R_a$ .

Figure 4.2 displays the amplification factor  $\mathcal{A}_{\omega m} = |\mathcal{A}_+/\mathcal{A}_-|^2 - 1$  in terms of the parameter  $\varpi = \omega/m\Omega$  for a specific set of parameters. For all frequencies below the superradiant condition ( $\varpi < 1$ ) this amplification factor is positive. The frequency at which  $\mathcal{A}_{\omega m}$  peaks is usually close to the threshold frequency  $m\Omega$ , becoming ever so close to this value as the absorption parameter  $\alpha$  is increased. Note that some of the curves correspond to superluminal regimes ( $\Omega R_a > 1$ ).

The behaviour of the scattering amplitudes is very similar to that of sound waves scattering off a uniform cylinder of a given impedance (see figure 3.2).

### 4.3.2 Cavity modes

When the reflecting boundary condition ( $\Psi = 0$ ) is imposed at the cavity radius  $R_c$ , our scattering problem turns into an eigenvalue one.

Taking the general solution (4.18), the regularity of the field at the origin tells us imme-

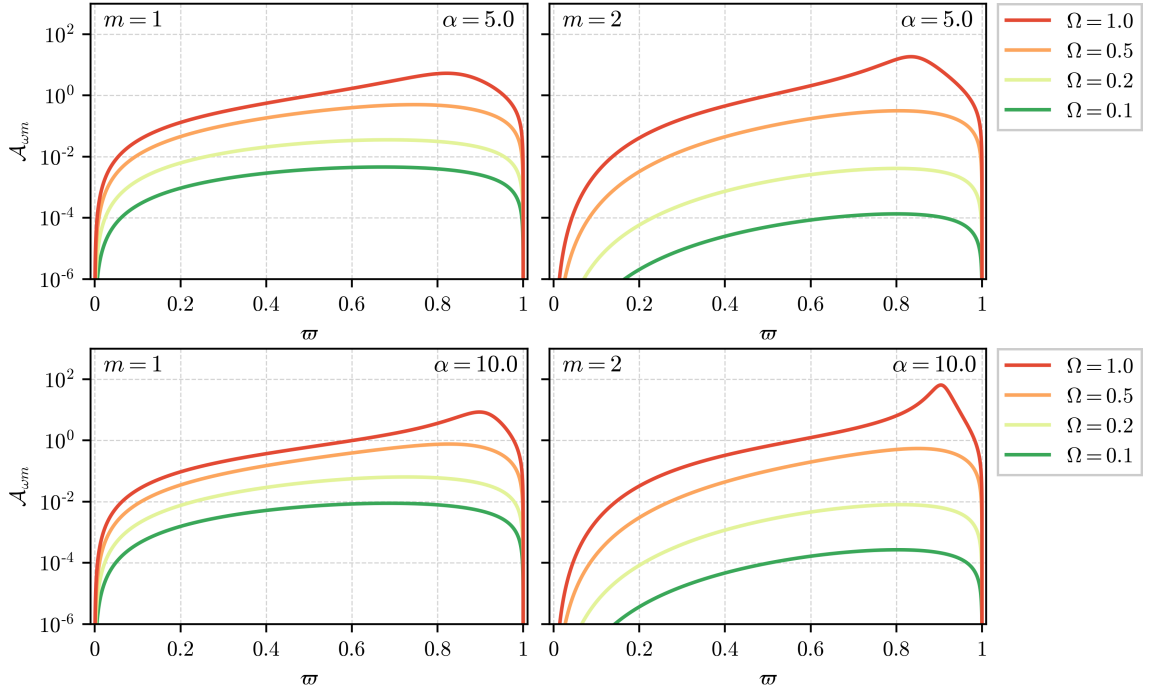


Figure 4.2: Amplification factor  $\mathcal{A}_{\omega m} = |\mathcal{A}_+/\mathcal{A}_-|^2 - 1$  for the SA model for two azimuthal modes  $m = 1$  (left column) and  $m = 2$  (right column), absorption parameter  $\alpha = 5.0$  (top row) and  $\alpha = 10.0$  (bottom row) for several rotation speeds. The curves are presented in terms of the frequency parameter  $\varpi = \omega/m\Omega$ .

diately that  $B = 0$  since all Bessel functions of the second kind  $Y_m$  diverge at the origin. The vanishing condition at the cavity radius  $\Psi(R_c) = 0$  also allows us to write a simple expression for the amplitude ratio  $D/C$  as

$$\frac{D}{C} = -\frac{J_m(\beta_0 R_c)}{Y_m(\beta_0 R_c)}. \quad (4.22)$$

The condition at the interface, however, is a bit more complicated. The matching of the field  $\Psi(R_a^-) = \Psi(R_a^+)$  tells us that

$$AJ_m(\beta_\alpha R_a) = CJ_m(\beta_0 R_a) + DY_m(\beta_0 R_a), \quad (4.23)$$

from where we can extract the ratio  $A/C$  to be

$$\frac{A}{C} = \frac{J_m(\beta_0 R_a)}{J_m(\beta_\alpha R_a)} + \left(\frac{D}{C}\right) \frac{Y_m(\beta_0 R_a)}{J_m(\beta_\alpha R_a)}. \quad (4.24)$$

Similarly, matching the field derivatives we have that

$$\frac{A}{C} = \frac{J'_m(\beta_0 R_a)}{J'_m(\beta_\alpha R_a)} + \left(\frac{D}{C}\right) \frac{Y'_m(\beta_0 R_a)}{J'_m(\beta_\alpha R_a)}, \quad (4.25)$$

where the primes denote derivative with respect to the radial coordinate  $r$ . Equating equation (4.24) and (4.25) we obtain

$$\frac{J_m(\beta_0 R_a)}{J_m(\beta_\alpha R_a)} + \left(\frac{D}{C}\right) \frac{Y_m(\beta_0 R_a)}{J_m(\beta_\alpha R_a)} - \frac{J'_m(\beta_0 R_a)}{J'_m(\beta_\alpha R_a)} - \left(\frac{D}{C}\right) \frac{Y'_m(\beta_0 R_a)}{J'_m(\beta_\alpha R_a)} = 0 \quad (4.26)$$

with  $D/C$  given by (4.22). Simply put, the solutions to our problem are the ones for which the oscillating frequency  $\omega$ , satisfy the above equation. In other words, if we define the LHS of this equality as  $G_m(\omega)$ , we have an eigenvalue equation

$$G_m(\omega) = 0. \quad (4.27)$$

For a given set of parameters  $(R_a, R_c, \Omega, \alpha, m)$ , the roots of  $G_m$  correspond to the allowed eigenfrequencies

$$\omega = \omega_R + i\omega_I, \quad (4.28)$$

that are in general complex-valued. The growing modes are characterized by a positive imaginary part  $\omega_I > 0$ , corresponding to field configurations that grow exponentially in time  $\Psi \sim e^{\omega_I t}$ . Roots whose imaginary part is negative ( $\omega_I < 0$ ) correspond to modes damped in time.

For a given set of parameters,  $(R_{BH}, R_C, \alpha)$ , the allowed frequencies for our solution correspond to the zeros of  $G_m(\omega)$ . Our work now falls back on finding solutions to equation (4.27). These solutions have no clear way of being found analytically but are rather easy to find with the help of numerical methods (see below). The solutions will, in general be complex valued with a real and imaginary part:

$$\omega = \omega_R + i\gamma \quad (4.29)$$


---

Where  $\omega_R = \text{Re}[\omega]$  is the part responsible for the oscillation of our solution in time and  $\gamma = \text{Im}[\omega]$  is the growth rate associated with that same oscillation. If  $\gamma > 0$  the field will grow in time while if  $\gamma < 0$ , the oscillation will be exponentially damped.

The search for solutions of (4.27) is not a trivial task so we shall take a small detour into the method employed since it is generic enough to be applied to similar problems.

If we remove the absorbing region from inside the cavity (equal to setting  $\alpha = 0$ ) the solution will reduce to a simple bessel function describing the normal oscillating modes with frequencies given by the solutions of

$$J_m(\beta_0 R_c) = 0 . \quad (4.30)$$

There is an infinite number of natural frequencies, usually denoted by  $j_{m,k}$ , where  $k$  is the order of the zero. The first few zeros for several  $m$ -values are presented in table 4.2, and the associated solutions in figure 4.3. In the complex  $\omega$ -plane, all these solutions lay on the real axis, describing purely oscillating solutions that satisfy the boundary conditions.

Table 4.2: First few roots of the Bessel function of the first kind  $J_m(x)$

$k$	$J_0(x)$	$J_1(x)$	$J_2(x)$	$J_3(x)$	$J_4(x)$	$J_5(x)$
1	2.4048	3.8317	5.1356	6.3802	7.5883	8.7715
2	5.5201	7.0156	8.4172	9.7610	11.0647	12.3386
3	8.6537	10.1735	11.6198	13.0152	14.3725	15.7002
4	11.7915	13.3237	14.7960	16.2235	17.6160	18.9801

If we now consider the absorbing region with radius  $R_a$  and a given  $\alpha$ , we can slowly increase this absorption parameter from zero up to the desired value and follow the trajectory of the roots on the complex plane. Numerically, this is done by considering a discrete set of absorption parameters and, starting from the Bessel zeros, find iteratively, the new allowed frequencies. If we consider the case of a totally absorbing region, we can actually describe the track of the zeros analytically. In this case, the eigenvalue problem reads

$$J_m(\beta_\alpha R_c) = 0 \quad (4.31)$$

and the eigenfrequencies are easily obtained by equating the argument with the bessel zeros  $j_{m,k}$

$$(\omega R_c) = -i \left( \frac{\alpha R_c}{2} \right) \pm \sqrt{(j_{k,m})^2 - \left( \frac{\alpha R_c}{2} \right)^2} . \quad (4.32)$$

The above equation is in close analogy with the eigenfrequencies of a damped harmonic oscillator (DHO) of mass  $m$ , damping coefficient  $\mu$  and natural frequency  $\omega_0$

$$\omega = -i \left( \frac{\mu}{2m} \right) \pm \sqrt{\omega_0^2 - \left( \frac{\mu}{2m} \right)^2} . \quad (4.33)$$

In a similar way to what is observed between the underdamped, critically damped and over-

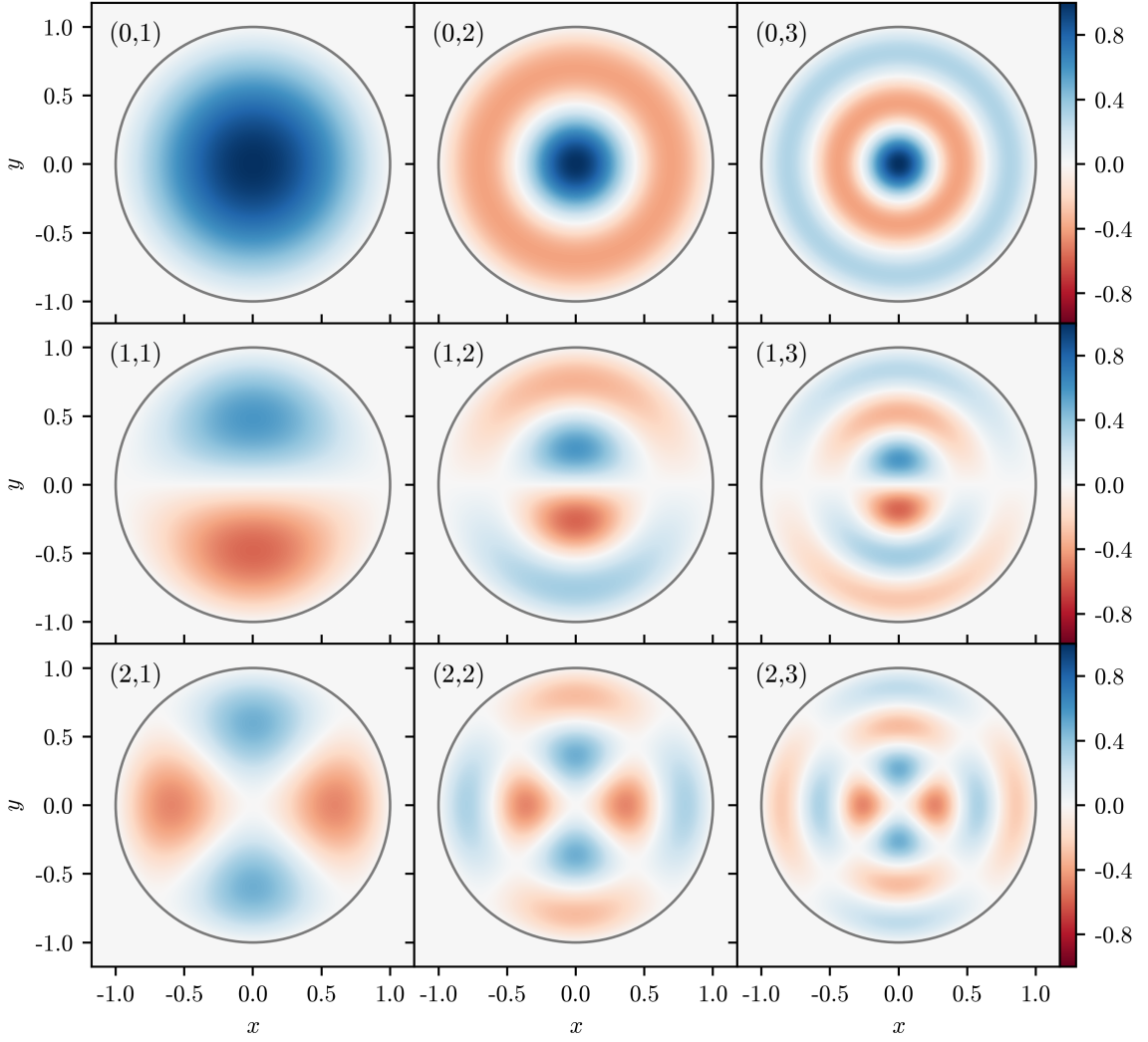


Figure 4.3: 2D plot of cavity resonances (Bessel functions). On the upper left corner of each plot we have indicated  $(m, k)$  where  $m$  is the azimuthal mode and  $k$  is the order of the frequency that satisfies the boundary conditions.

damped scenarios, we have that, as long as  $\alpha R_c < 2 j_{k,m}$ , the solutions for the cavity are oscillating but decay in time with growth rate  $\gamma = -\alpha R_c/2$ . If  $\alpha R_c > 2 j_{k,m}$ , however, the solutions are critically damped and don't oscillate at all. The damping coefficient in this case is given by

$$\gamma = \left( \frac{\alpha R_c}{2} \right) \left[ 1 \mp \sqrt{1 - \left( \frac{2 j_{k,m}}{\alpha R_c} \right)^2} \right]. \quad (4.34)$$

A crucial difference between the two scenarios is that, while for the DHO case we have a single natural frequency, in the cavity, there is an infinite number of natural frequencies that can be excited. In figure 4.4 we have a detailed plot of the parametric curves (4.32) in the complex plot for the  $m = 1$  case. We see that, after the appropriate threshold, the solution becomes critically damped.

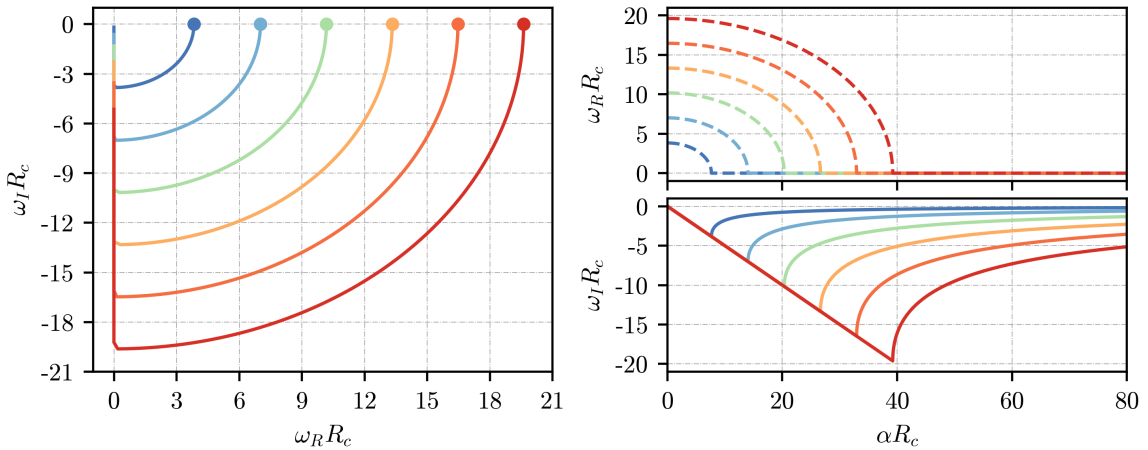


Figure 4.4: (Left) Parametric curves (4.32) for the first 6 Bessel roots and  $m = 1$  as a function of the absorption parameter  $\alpha$ . The curves start at the Bessel zeros (solid points). (Right) The evolution of the real (dashed lines) and imaginary (solid lines) of the allowed frequencies shown on the left-most plot.

Onto the generic case, no closed form equation exists for describing the path of the roots in the complex plane. Just like what was observed for the *Acoustic bomb* of chapter 3, the variable  $R_{\text{BH}}/R_c$  cannot be used as an independent quantity to probe the root behaviour of  $G_m(\omega)$ . Like then, we shall restrict our analysis by fixing  $R_a = 2M$  with  $M = 1$  and study the system by varying the remaining parameters ( $\Omega$ ,  $R_c$ ,  $\alpha$ ).

As already pointed out, the roots location on the complex plane will drift away from the Bessel zeros as we increase the absorption and rotation parameter. The numerical procedure is summarized in figure 4.5 for a specific set of parameters.

The left plot displays the procedure of slowly increasing the absorption parameter  $\alpha$  and, as expected, all roots acquire a negative imaginary part as all cavity modes get dampened in time. Note that, the lower energy modes (small  $k$ ) are much longer lived than the high energy ones, as one should expect since longer wavelength fields will not 'see' the small cylinder.

The plot on the right depicts the effect of increasing the absorption region rotation on the roots found after the first iteration procedure. The roots *rise* in the complex plane with the particularity that, roots whose real part satisfy the superradiant condition ( $\omega < m\Omega$ ) acquire a positive imaginary part, meaning that these modes get amplified by the rotating absorbing region.

Of main interest to us is the location of the eigenfrequency corresponding to the fastest growing mode. This corresponds to the root with largest imaginary part,  $\max(\omega_I) \equiv \omega_I^{\text{max}}$  and will thus dominate the dynamics of the system over large timescales.

The dependence of the maximum growth rate on  $\alpha$  for two distinct azimuthal modes and several cavity sizes is depicted in figure 4.6. For both azimuthal modes, the maximum growth rate curve behaves similarly. The main difference between the two is seen in the real part of the eigenfrequencies since higher  $m$  modes have larger (faster) oscillating frequencies. As the absorption parameter is increased, the real part of the fastest growing mode tends to the superradiant threshold value  $m\Omega$ .

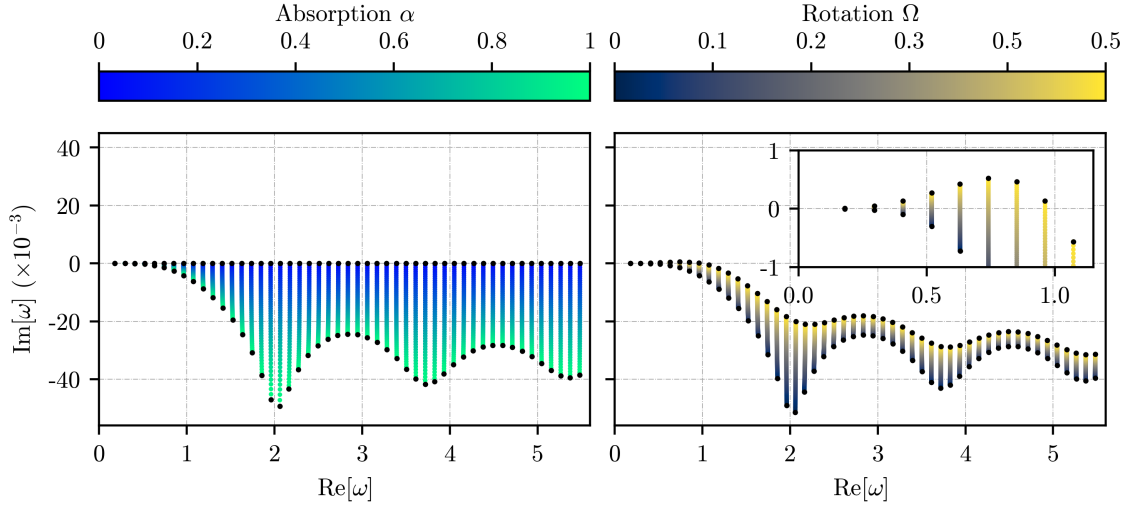


Figure 4.5: Root finding procedure illustration for the case of a maximally rotating cylinder  $R_{BH}\Omega = 1$  with absorption parameter  $\alpha = 1$  in a cavity of size  $R_c = 30$ . (Left) Root behaviour as the absorption parameter is increased from 0 to 1. All roots acquire a negative part, corresponding to absorption on a timescale of the order  $1/\omega_I$ . (Right) Behaviour of previously found roots as the rotation of the cylinder is increased. Roots whose real part satisfied the superradiant condition (2.23) have a positive imaginary component.

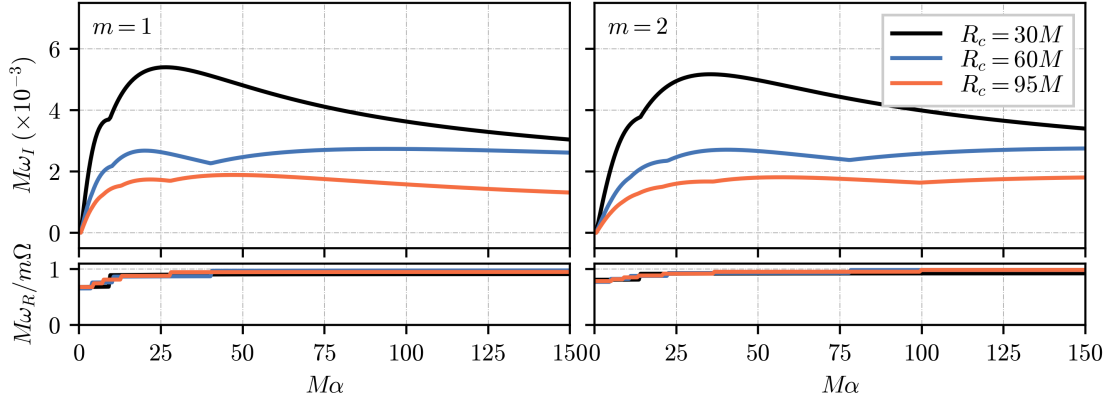


Figure 4.6: Maximum growth rate dependence on the absorption parameter  $\alpha$  for the azimuthal modes  $m = 1$  and  $m = 2$  and several cavity sizes. For small  $\alpha$ , the relation is close to linear, in agreement to what was observed for stars [2].

The most important feature to remark, however, is that the dependence of  $\omega_I^{\max}$  on  $\alpha$  is roughly linear for  $\alpha \sim 0 - 20$ . This is in accordance with what is observed for slowly rotating stars and seems to be a universal behaviour of systems with such geometry [2].

The dependence of the instability rate on the cavity size is also interesting and is depicted in figure 4.7 for several azimuthal modes. The dashed line represents the curve proportional to the travel time of a pulse inside the cavity  $\tau = (R_c - R_a)^{-1}$ . For large cavities, the maximum amplitude seems to follow this behaviour. On physical grounds this is expected since the growth rate of the field should be proportional to how often the pulse interacts with the inner region; nevertheless this overall behavior is interesting, as each individual mode must

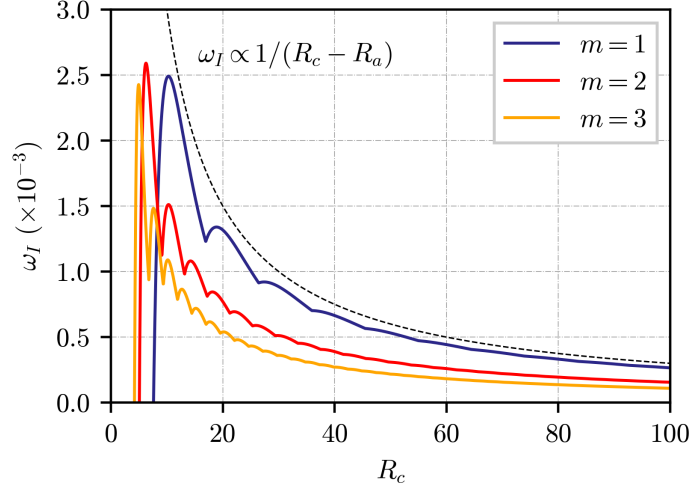


Figure 4.7: Dependence of the maximum growth rate on the size  $R_c$  of the cavity for the SA model with  $\alpha = 10$ ,  $R_a = 2$  and  $\Omega = 0.5$ . Each individual concave region of the curve corresponds to a different radial mode. The dashed line depicts the frequency of the traveling pulse inside the cavity. Notice that lower  $m$  modes having higher instability rates, at fixed cavity size. For each mode, the threshold is very close to the associated fundamental cavity mode  $j_{m,0}/(m\Omega)$ .

also be sensitive to the amplifying region itself [24]. Interestingly, as was shown in chapter 2, this behaviour is also observed in the case of an actual BH enclosed in a cavity in (3+1) dimensions.

### 4.3.3 Numerical Comparison

Our analytical findings can be corroborated by comparison against the numerical time integration of the governing equation (4.10). Considering a single absorbing region ( $R_0 = 0$ ) we can do an extensive study of the field behaviour inside the cavity by varying  $R_c$  and  $\Omega$ .

Figure 4.8 features snapshots of the field configuration at three distinct instants of the numerical evolution for a particular simulation where instability of the cavity against superradiance is observed. As time goes by the amplitude of the scalar field increases exponentially. Notice that on the rightmost panel the system evolved for  $\sim 200$  revolutions, still a modest number.

The lack of mode mixing in the case of a uniform cylinder and its inevitability in the asymmetric scenario can be numerically confirmed by decomposing the field in azimuthal modes at a specific radial coordinate

$$\Psi(t, r, \varphi) = \sum_m \Psi_m(t, r) \cos(m\varphi), \quad (4.35)$$

where the coefficients  $\Psi_m$  are given by

$$\Psi_m(t, r) = \frac{1}{\pi} \int_0^{2\pi} \Psi(t, r, \varphi') \cos(m\varphi') d\varphi'. \quad (4.36)$$

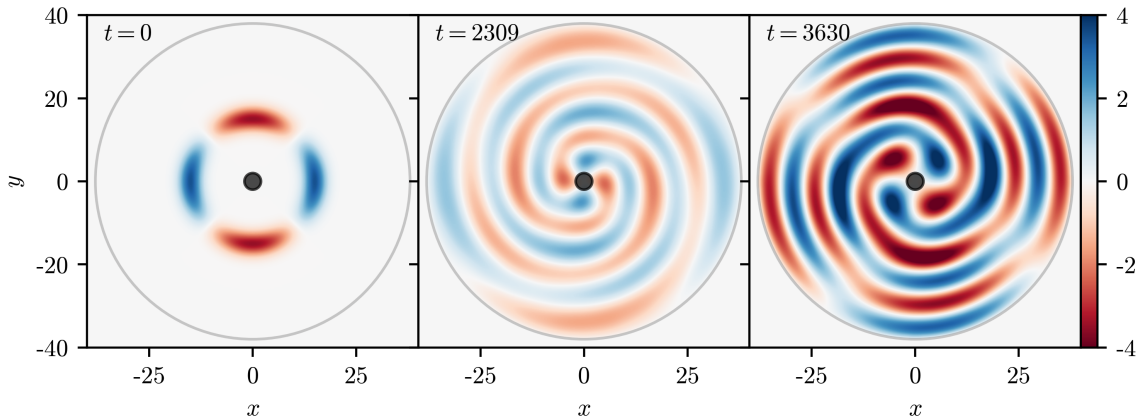


Figure 4.8: Snapshots of field configuration for three distinct simulation times for an initial Gaussian pulse of the form presented in (4.11) with the initial conditions presented in Table 4.1 (SA model). The cavity has a radius  $R_c = 38$  and the absorbing cylinder is rotating with constant angular velocity  $\Omega = 0.35$ . As explained in the text, the angular pattern corresponds to that of a quadrupolar  $m = 2$  mode, and the rotation of the cylinder excites predominantly a radial mode with overtone  $k = 5$  ( $k = 0$  is the fundamental mode), hence with six nodes, as can be seen in the radial profile.

The evolution of the Fourier coefficients  $\Psi_m$  are shown in figure 4.9 where the field components can be seen to grow exponentially in time,  $\Psi_m \sim e^{\gamma t}$ .

The azimuthal mode of the initial pulse is easily seen to dominate the dynamics throughout the simulation with a (numerical) growth rate  $\gamma$  that is in accordance with the analytical value for  $\omega_l^{\max}$  (see caption of figure 4.9).

The existence of higher harmonics cannot be completely mitigated due to the Cartesian nature of our numerical grid, but their low amplitude makes the lack of mode mixing evident. The growth rate of these modes agrees as well with the analytical values. Finally, and consistently with the results of figure 4.7 these lower  $m$  modes have larger instability rates and thus – even when triggered from noise – will eventually grow to dominate the dynamics.

The agreement of the real part of the numerically obtained frequency ( $\omega_R$ ) with the analytical one can also be tested by performing a late time Fourier analysis of the field displacement at a fixed point inside the cavity. This analysis is summarized in figure 4.10 where one can clearly see the superposition of the several cavity natural frequencies whose imaginary part is positive. Again, note that the fastest growing frequency is not the one closest to the superradiant threshold. In the particular scenario depicted, it corresponds to the 6th Bessel overtone. This can be confirmed visually in figure 4.8 by counting the number of nodes in the radial direction.

The growth rate of the energy density of the field inside the cavity, calculated from equation (4.12), is also easily seen to agree with the expected growth rate of  $\epsilon \sim e^{2\omega_l t}$ .

Similarly to what was observed in the model of chapter 3 (see section 3.3) and in the BH bomb scenario (see chapter 2 and reference [43]), a lower limit exists on the cavity size that allows the amplification of the field.

The exact value for this size can be obtained from the data of figure 4.7. However, a

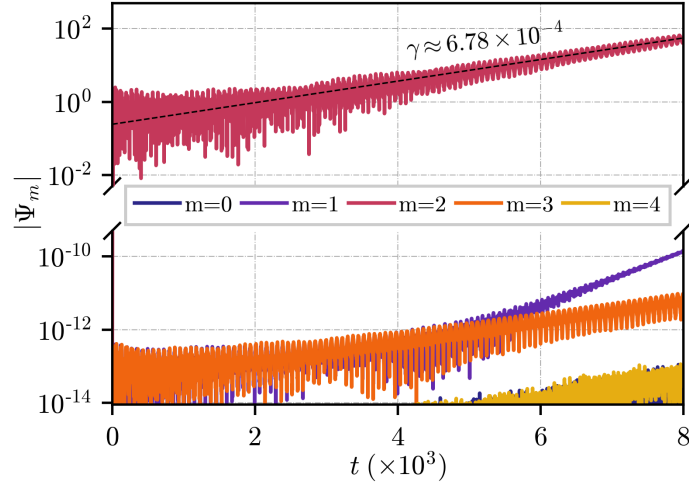


Figure 4.9: Mode decomposition of the field at a radius of  $r = 30$  for an initial Gaussian pulse of the form (4.11) with the parameters presented in Table 4.1 (SA model) in a cavity with radius  $R_c = 38$ . The absorbing cylinder is rotating with angular velocity  $\Omega = 0.35$ . The dashed black line depicts the analytically obtained growth rate of the fastest growing mode. The numerically obtained frequency of the field is  $\omega = 0.5560 + 0.000677i$ . See also figure 4.10.

rough estimate can be obtained by noting that the real part of the roots of  $G_m$  is very close to the roots of  $J_m(\omega R_c)$ , i.e., to the eigenfrequencies of an empty cavity. This implies that the threshold for amplification of the  $(m, k)$ -th mode is given by

$$R_c > \frac{j_{m,k}}{m\Omega}, \quad (4.37)$$

where  $j_{m,k}$  is the  $k$ th zero of the  $m$ -mode Bessel function of the first kind. Note that this condition is the same as the one obtained for the BH bomb, equation (2.50). For a given  $m$ , the absolute minimal value of  $R_c$  for amplification to occur is simply  $j_{m,0}/(m\Omega)$  and when  $R_c \gg R_a$  the excited modes inside the cavity essentially correspond to slightly perturbed empty cavity modes due to the presence of the small absorbing region.

## 4.4 Binaries and cavity resonances

For the BA model, no analytical expression exists for the eigenfrequencies, and we must resort solely to the numerical integration of the KG equation with the appropriate boundary conditions.

Figure 4.11 depicts the field configuration inside a cavity with a binary at three distinct simulation times. The initial conditions are similar to those used for the SA model in the previous section (see Table 4.1). We performed the same analysis as before, only now without a direct analytical comparison.

The azimuthal components of the field at a given radius, given by (4.36), are presented in figure 4.12. Like in the single absorbing region scenario, we observe amplification of the

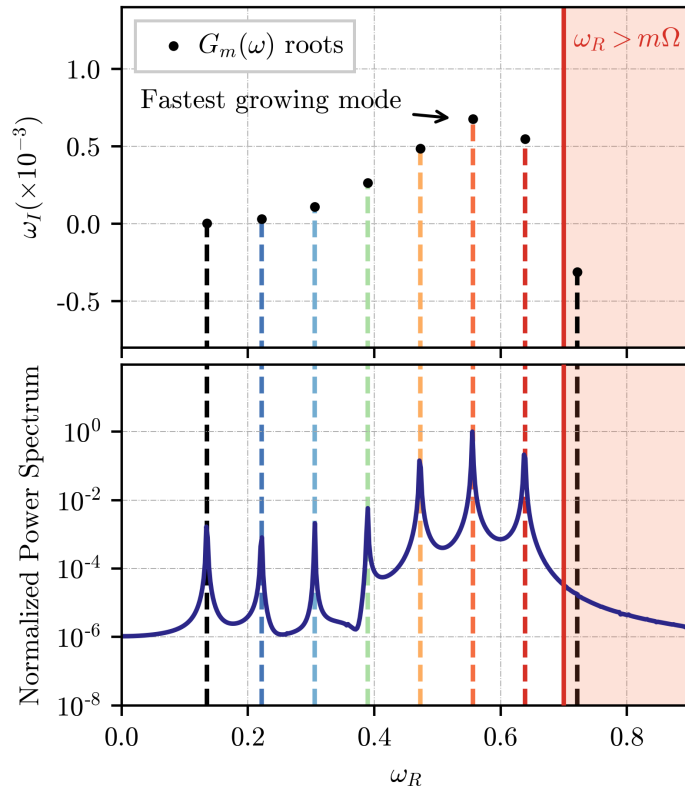


Figure 4.10: Comparison of the real part of the SA model eigenfrequencies with the numerical data for the simulation whose parameters are presented in Table 4.1 (SA model). The top plot represents the analytical eigenfrequencies in the complex plane. The bottom one depicts the Fourier analysis of the field displacement at  $r = 20$  for the time interval  $\Delta t = [3000, 4000]$ . Note that all roots with positive imaginary part lie below the superradiant threshold (red solid line).

field. This seems to be the first solid evidence of binary superradiant instabilities.

Like before, here as well the initial mode of the field  $m = 2$  is seen to dominate the dynamics of the system. However, the evolution of such mode is accompanied by equal-parity modes ( $m = 0, 4, \dots$ ) that grow on similar timescales. As before (see Sec. 4.3), the presence of higher odd harmonics cannot be fully mitigated. Despite this, their low amplitude makes it evident that only even modes get coupled to the initial pulse. This type of coupling is similar to what we explored in the asymmetric cylinder model of chapter 4. Although we have focused our analysis on initially quadrupolar ( $m = 2$ ) field configurations, simulations with an initially  $m = 1$  pulse also couple with equal parity modes ( $m = 3, 5, \dots$ ) and have typically higher growth rates than the even modes.

The dashed line in figure 4.12 corresponds to a linear fit to this mode at late times. The growth rate observed for the specific set of parameters depicted is  $\gamma \sim 1.32 \times 10^{-4}$  – an order of magnitude below the rate for a relatively fast spinning single absorbing region (see figure 4.9).

For a proper comparison of the two scenarios, however, we need to choose an appropriate set of parameters. Namely, with the aim of discussing astrophysical scenarios, it is

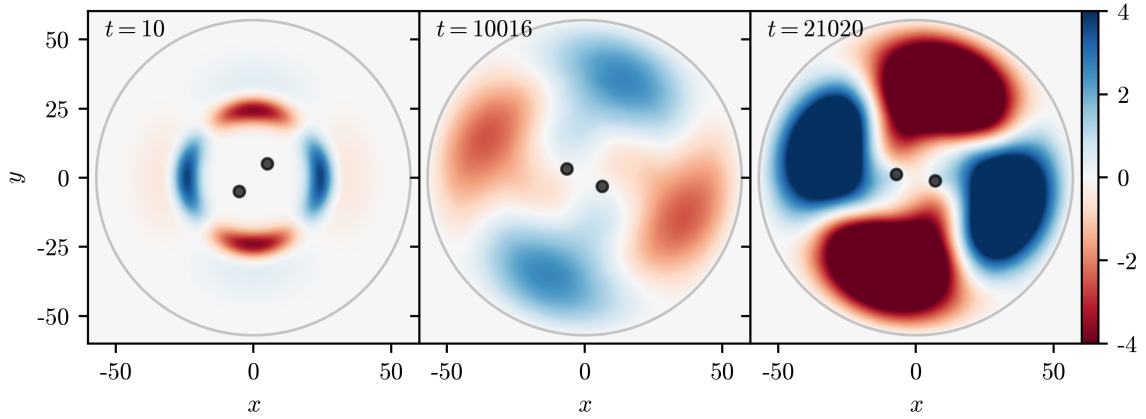


Figure 4.11: Snapshots of field configuration for three distinct simulation times for an initial Gaussian pulse of the form presented in (4.11) with the initial conditions presented in Table 4.1 (BA1). The cavity has  $R_c = 57$  and the two absorbing cylinders are in a circular orbit of radius  $R_0 = 7.15$ . The orbital period is  $T \approx 85$ . Note that one could expect frequencies close to  $\lesssim m\Omega$  to be excited and hence – based on figure 4.10 – that the fundamental mode is excited to higher amplitude. This expectation seems to be supported by the radial profile of the scalar field. See also the main text and Table 4.3.

particularly interesting to consider a single absorbing region with  $R_a = 4$  rotating with the same angular velocity as the binary and inside a cavity of the same size. The comparison of the eigenfrequencies for the two scenarios is shown in Table 4.3.

The real part of the field frequency  $\omega_R$  for both cases is very similar. In fact, both configurations excite the first fundamental mode of the cavity. A natural interpretation is that the excitation of a lower energetic cavity mode is mainly caused by a lower frequency of the driving perturber, and not necessarily by a different problem geometry. However, the relation between the radial separation of the binary (a measure of asymmetry) and its orbital velocity (4.9) makes this a subtle question to which we shall return at the end of this section.

The problem’s different geometry, nonetheless, seems to be evident when evaluating the growth rate of the modes. From Table 4.3, the growth rates differ by an order of magnitude. The binary system allows the excitation of the same low energy mode on much shorter timescales. Physically, for the same angular velocity, the large separation between the two

Table 4.3: Comparison of the  $m = 2$  eigenfrequencies for the BA and SA models (with  $R_a = 4$  for the latter, intended to describe astrophysical systems with the same total mass) inside a cavity of size  $R_c = 57$ , rotating with the same angular speed  $\Omega$ . For the binary,  $\Omega$  corresponds to  $R_0 = 7.15$ . The BA eigenfrequency was obtained numerically while the SA is obtained analytically by solving (3.39).

Model	$\Omega$	$\omega_R + i\gamma$
SA	0.07397	$0.0901 + (8.719 \times 10^{-6})i$
BA	0.07397	$0.0898 + (1.320 \times 10^{-4})i$

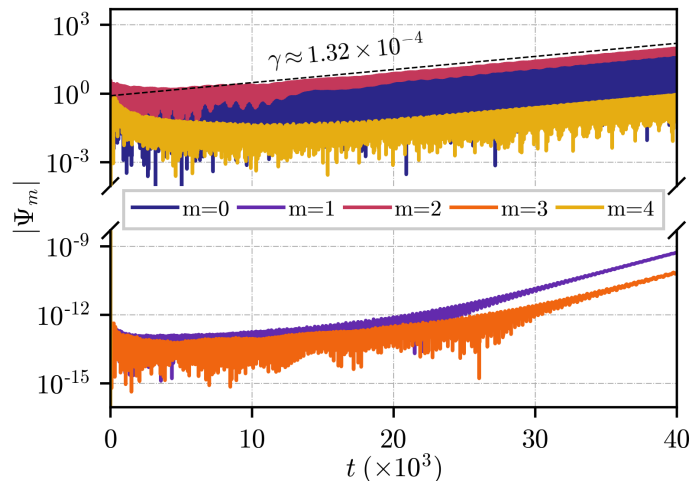


Figure 4.12: Mode decomposition of the field at a radius of  $r = 20.0$  for the simulation depicted in figure 4.11 (see Table 4.1 for initial configuration parameters). The initial field azimuthal mode is  $m = 2$ . The generation of higher, even-parity harmonics is observed from the first interaction with the binary. The dashed black is a linear fit to the  $m = 2$  curve at late times (shifted upwards). The initial interaction generates other harmonics with the same parity ( $m = 0, 4, \dots$ ) that seem to follow the same growth rate. Odd parity modes ( $m = 1, 3, \dots$ ) are also present but grow from the numerical noise and have growth rates larger than even modes.

absorbing regions allows the points within them to be moving much faster, hence allowing a larger angular momentum transfer between the binary and the field. This is the first feature where the geometry of the problem clearly affects the field configuration – larger growth rates for lower energetic field modes.

Figure 4.13 depicts the time fourier analysis of the field behaviour at a point inside the cavity with a binary. The left panel displays the spectrogram of the field while the right one displays the late time fourier analysis of the field. Unlike the single absorbing region scenario (see figure 4.10) we have no analytical eigenfrequencies, but as can be seen, the dominant frequency agrees with the natural cavity ones (represented by the dashed lines). The blue region represents the frequencies for which  $\omega > m\Omega$ , with  $\Omega$  the binary frequency. In the SA model scenario, this corresponded to the superradiant threshold for which no excitations existed. Here, contrarily, the usual threshold does not seem to represent a special value.

As already mentioned, the geometrical configuration of the system and the perturbation frequency due to the presence of an absorbing region are intrinsically connected, making the orbital frequency play a crucial but nontrivial role in the long term behaviour of the field's energy content.

To better understand the growth rate dependence on the orbital radius of the binary we performed a large number of simulations sweeping a range of orbital radii. The dependence can be seen in figure 4.14 for two cavity sizes  $R_c = 58$  and  $R_c = 95$ . The smaller cavity links with the simulation of figures 4.11, 4.12 and 4.13, for which an initially Gaussian  $m = 2$  pulse was used for the field's initial configuration. For the larger cavity, we took instead a

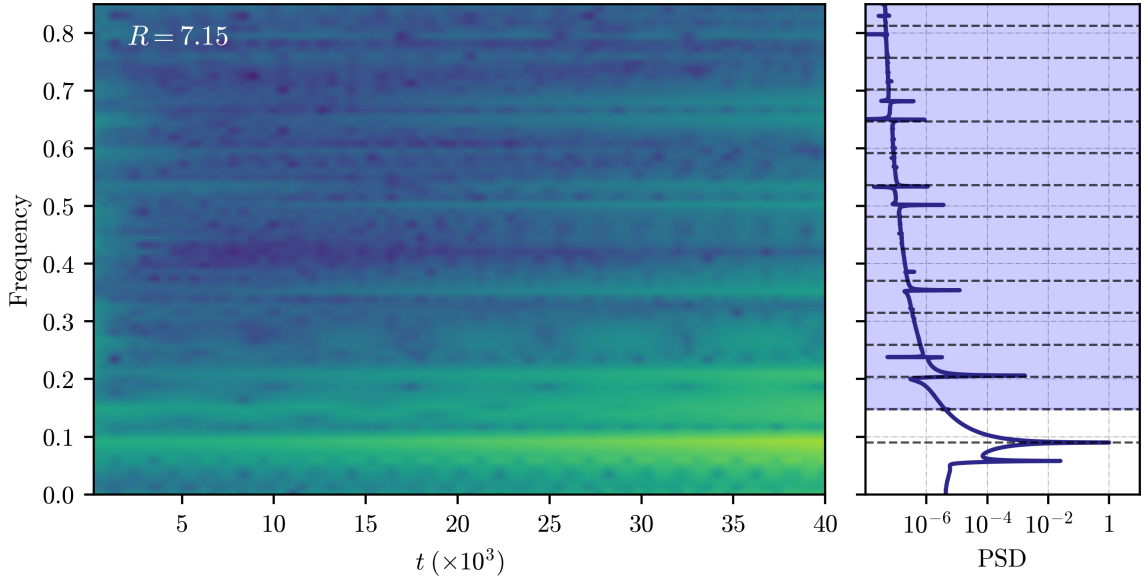


Figure 4.13: Fourier analysis of the field displacement at a radius of  $r = 20.0$  for the simulation of depicted in figure 4.11 (see Table 4.1 for initial configuration parameters). The initial field azimuthal mode is  $m = 2$ . The left panel depicts the spectrogram of the field while the right one represents the averaged power spectrum. The dashed lines represent the natural frequencies of the cavity  $j_{k,m}/R_c$  with  $m = 2$ . The blue region represents the frequencies above the superradiant threshold  $\omega > m\Omega$  with  $\Omega$  being the orbital Kepler frequency. The dominant mode corresponds to the lowest energetic mode of the cavity, but higher frequencies (above the usual threshold value) are also excited.

pulse with azimuthal number  $m = 1$ .

The dashed vertical lines correspond to the orbital radii for which the perturbing frequency  $2\Omega$  (note the symmetry of the problem), matches the natural cavity ones, i.e, for which  $2\Omega = j_{m,k}/R_c$ . Explicitly we have

$$R_{m,k} = \left[ 2 \left( \frac{2R_c}{j_{m,k}} \right)^2 \right]^{1/3}. \quad (4.38)$$

The smaller cavity scenario (bottom panel in figure 4.14) displays a very clean behaviour over the orbital values considered. As one approaches the resonant radius  $R_{2,2} \approx 7.15$ , the growth rate behaves in a oscillatory manner with overall larger amplification rates. This behaviour is not observed for the second resonant orbital value  $R_{2,1} \approx 9.95$ . Instead, the growth rate plunges towards zero as one approaches it from smaller (larger) orbital radii (frequencies). Remarkably, the  $R_{2,1}$  line roughly marks the transition between exciting the  $k = 1$  radial mode (for  $R_0 \lesssim R_{2,1}$ ) and exciting the fundamental  $k = 0$  mode (for  $R_{2,1} \lesssim R_0 \lesssim R_{2,0}$ ). For larger radii, the binary has a lower orbital frequency than the lowest cavity mode and the field never gets amplified.

This seemingly “clean” behaviour contrasts with the rather intricate dependence the same value has for a larger cavity (top figure). When  $R_c$  increases, Eq. (4.38) indicates

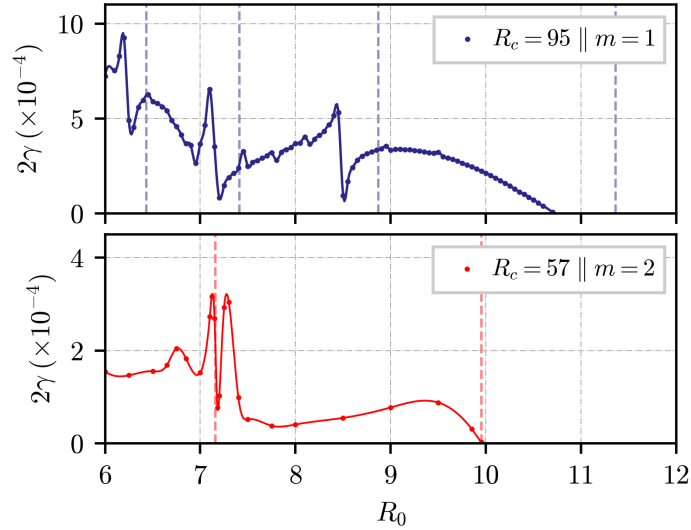


Figure 4.14: Energy growth rate dependence on the orbital radius of the two equal mass binary in a cavity of radius  $R_c = 57$  (note the factor two in the axis, since the growth rate should be twice as large as that of the field itself). Dots represent the numerically obtained energy growth rates, while the dashed line corresponds to a quadratic spline. The vertical lines represent the radii defined by Eq. (4.38). The initial pulse parameters are presented in Table 4.1. We used the BA1 (BA2) initial pulse parameters for the bottom (top) plot.

that more resonant orbits are expected to exist in a given interval of orbital radii. Small peaks in growth rate can be seen at the resonant radii, but a large increase in growth rate is not observed at the specified orbits but always at slightly smaller ones. Also, despite observing the excitation of higher  $k$ -modes as the orbit is shrunk, no clear transition exists as one crosses the resonances. The fundamental  $k = 0$  mode dominates the simulation at all timescales for almost all the probed range of radii. The exceptions seem to occur at the resonance orbits where in fact the associated mode seems to be excited. Table 4.4 contains the numerically obtained eigenfrequencies of the field for 3 distinct orbital radii. As just mentioned, the excitation of the most fundamental cavity mode for most orbital radii can be seen from the real part of the frequency.

Table 4.4: The  $m = 1$  eigenfrequencies, extracted from late time Fourier analysis for  $R_c = 95$ . Compare the real part of the frequencies with the first two cavity eigenfrequencies  $j_{1,0}/R_c = 0.040333$  and  $j_{1,1}/R_c = 0.738483$ . Note that  $R_0 = 7.1, 8.44$  excite the same cavity mode with  $j_{1,0}/R_c = 0.040333$ .

$R_0$	$2\Omega$	$\omega_R + i\gamma$
6.19	0.1837	$0.07390 + (9.503 \times 10^{-4})i$
7.10	0.1495	$0.04034 + (6.531 \times 10^{-4})i$
8.44	0.1154	$0.04034 + (5.475 \times 10^{-4})i$

It is also important to note that the rightmost resonance indicated in the plot at  $R_{1,2} \approx 11.36$  does not correspond to the lowest cavity eigenmode and thus, the growth rate falls

below zero much before we reach the limit imposed by (4.38).

The reason for this behaviour is not entirely clear but two things should be mentioned. First, the width of each peak is much smaller than the radius of the binary components ( $R_a = 2$ ) and thus the complex behaviour may be due to the interior freedom of the field in each region. Secondly, the excitation of the fundamental mode ( $k = 0$ ) for the larger cavity points to a nontrivial connection between different  $k$ -modes (as the fundamental mode may be draining energy from the more energetic ones). This last point may also relate to the geometry of the system, since different azimuthal modes are now coupled and, even if the frequency of the perturber matches that of the field, the positions of the regions with respect to the cavity mode profile may avoid its proper excitation.

Finally, perhaps the most important point to retain is the fact that growth rates are large and remain large even when the orbital radius varies by a factor two. This property could be important for astrophysical systems or for Earth-bound experiments.

## 4.5 Application to black hole physics

The main goal of our study is to make the connection of our simple model with relevant astrophysical scenarios, namely, to BHBs and other compact binary systems.

As previously mentioned, superradiance is intrinsically related to dissipative systems. BH binaries, just like single BHs, present us with an intrinsic dissipation mechanism in the form of an event horizon and so, the natural question arises: are BH binaries, even if composed of nonspinning BHs, prone to similar superradiant phenomena?

The nontrivial geometry of a BH binary and the radiation losses through gravitational-wave emission make the problem challenging to describe in its full generality [36, 68]. As a consequence, the question of if, how and when this phenomenon is relevant in actual astrophysical scenarios remains an unanswered one.

We would then like to use the just acquired knowledge about the behaviour of our toy model to dwell on BH systems. We will thus extrapolate our results to BH binaries by promoting  $\alpha \sim 1/M$  (see section 4.1). We should first mention that this substitution yields sensible results: for a single spinning absorbing body with  $\alpha = 10$ , angular velocity  $\Omega \sim 0.5$  in a cavity with radius  $R_c = 38$ , the typical amplification scales are of order  $\gamma \sim 10^{-3} - 10^{-4}$  (see figure 4.7). This rate is around one order of magnitude larger than the rate of a (3+1) BH bomb with similar cavity radius and BH spin with corresponding parameters (see chapter 2 and references [37, 43]).

A thorough comparison of the two models and its eigenfrequencies is out of the scope of this work (but see appendix E for the study of the (3+1) equivalent prescription of a single absorbing regions). Nevertheless, this quick-and-dirty comparison shows that the simple dissipative model considered reproduces, within an order of magnitude the correct timescales of a three-dimensional, spinning BH enclosed in a cavity. As mentioned in chapter 2, these instabilities may have short timescales – for a solar mass BH, these correspond to a few seconds while for very massive ones (like the one at the center of our galaxy) the timescales can be of the order of a few months.

As well mentioned in chapter 2 was the reason to consider our systems inside a cavity. Besides mimicking the natural behaviour of massive fields, the reflecting boundary condition may as well model the natural confining mechanism of anti-de Sitter spacetimes. The results here presented then, should find natural application in such setups, where single spinning black holes are known to be unstable to superradiant phenomena [46, 69, 70, 71, 24]. Our results indicate that so are binaries, but leave open the nonlinear evolution of such systems.

In an astrophysical context, one should worry about a few issues, one of them being the cavity size and orbital radii. We did not probe the dynamics of the field for orbital radii smaller than  $R_0 = 6.0$  since, even without an exact metric, the last stable orbit (LSO) of an equal mass BHB has been evaluated at 2PN order to be  $R_{LSO} \approx 5.718$  [49]. After crossing this point, the BHB plunges, making at most a few orbits and then merging into a rotating BH. In this late regime as well, we expect our model to not correctly model the physical system due to the high curvature of the spacetime near the binary. However, the presence of fields can, in principle, affect the late stage dynamics of a plunging BHB.

The LSO value of an equal mass BHB also places a constraint on the smallest possible cavity size for amplification to occur. In Sec. 4.4 we sought orbital radii that excited the fundamental modes of a fixed sized cavity. Our result was that of Eq. (4.38). Turning the question around, we can fix the orbital radius of the BA model and ask what are the cavity sizes for which amplification is enhanced. Like before, we equate the perturbing frequency to the cavity natural ones,  $j_{m,k}/R_c$ , to obtain

$$R_c^{m,k} = \frac{j_{m,k}}{2\Omega} = \frac{j_{m,k}}{2} \sqrt{\frac{R_0^3}{2}}. \quad (4.39)$$

The above expression represents (for a given orbital radius  $R_0$ ) the threshold cavity size for the amplification of the  $(m, k)$ -mode. The absolute threshold for the amplification of the fundamental  $m$ -mode is given by  $R_c > R_c^{m,0}$ .

For a BHB in the LSO, we have  $2\Omega \sim 0.2$  and the crude estimate allows us to say that no amplification is expected for cavities smaller than  $R_c \sim 24.7$ . Note that the threshold radius matches exactly the single BH threshold for the  $m = 2$  case.

Figure 4.15 displays the dependence of the growth rate on the cavity size for a fixed orbital radius of  $R_0 = 7.1$ . The dashed lines display the cavity sizes  $R_c^{m,k}$  for the  $m = 1$  mode.

The numerically obtained growth rates for the energy field show that in fact, when the frequency of the BHB model matches that of a cavity natural mode, these seem to be larger. It is also evident that our crude estimate of the smaller cavity size for amplification to occur matches the numerics. Note the mild dependence of the instability rate on the cavity size  $R_c$ : at large  $R_c$  the local peaks seem to behave as  $\sim 1/R_c$ , in agreement with the rate for a spinning BH enclosed in a cavity in (3+1) dimensions (see chapter 2).

The existence of superradiant instabilities in such systems is prone to leaving clear observational signatures in both statistical and dynamical studies. In the former class, the loss of energy due to superradiance may compete with that due to gravitational radiation. For equal mass binaries in a circular orbit, the rate at which the orbital energy  $E_{\text{orb}} = M^2/(2R_0)$

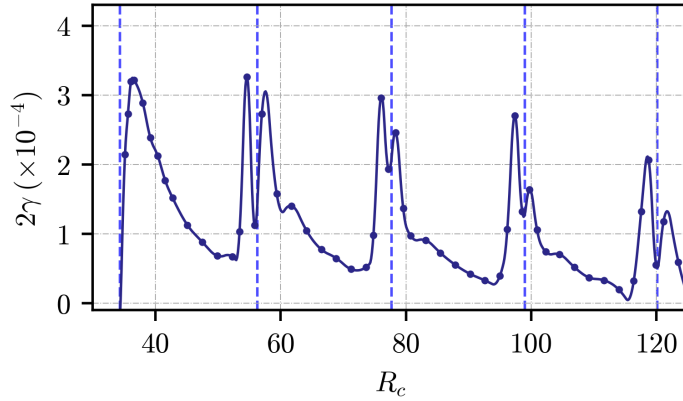


Figure 4.15: Energy growth rate dependence on the cavity radius for the BA with  $R_0 = 7.1$ . The vertical dashed lines correspond to the resonant cavity (4.39). The initial pulse parameters are given in Table 4.1. The envelope of the local peaks scale approximately as  $\sim 1/R_c$ . The local behavior has a steeper dependence. For example, around the first local peak, we find  $\gamma \propto R_c^{-5}$ . The initial pulse considered has the BA1 set of parameters presented in Table 4.1.

is radiated away is given by [72]

$$2M\gamma_{\text{grav}} = \frac{\dot{E}_{\text{grav}}}{E_{\text{orb}}} = -\frac{64}{10} \left( \frac{M}{R_0} \right)^4. \quad (4.40)$$

For a orbit of radius  $R_0 = 8.4$ ,  $2\gamma_{\text{grav}} = -1.29 \times 10^{-3}$ . For the same orbital radius, the growth rate of a scalar field with azimuthal number  $m = 1$  inside a cavity of size  $R_c = 95$  (top panel of Fig. 4.14), has an associated value of  $2\gamma = 5.2 \times 10^{-4}$  – a rate of comparable magnitude even in the late stages of inspiral.

Unlike what Eq. (4.40) implies, the behaviour of the energy loss to superradiance has a more complex dependence on the orbital radius  $R_0$  (see Fig. 4.14). The existence of radii for which the energy transfer between the binary and the scalar field is more effective, might lead to accelerated plunging of the BHB and give rise to a de-phasing of the GW signals observed when compared with the GW templates. The question of how this signature can be distinguished from other mechanisms (see, e.g., Refs. [73, 74, 75]) depends on the actual parameters and must be tackled on an individual basis.

The above effects may also lead to statistical features in the BHB population in our Universe and thus allow the placement of constraints on the mass of ultralight bosonic fields.

## 4.6 Outlook and future work

The results presented in this chapter serve as evidence that binary systems are also prone to robust superradiant scattering phenomena.

The binary model considered, albeit simple, retains the main geometrical features of astrophysical binary systems, such as BHs or compact stars, and is thus a good starting point to understand the signature left on a bosonic field interacting with such systems.

The model can also be used to describe many instruments or laboratory setups. It can, for example be used to describe the physics of spinning blades such as kitchen blenders, or physics associated with helicopter blades.

The two-dimensional model of a single absorbing region, discussed in Sec. 4.3 behaves in a similar manner to what is observed in actual  $(3 + 1)$  systems, such as rotating cylinders interacting with sound waves or electromagnetic waves [1, 76], or even a BH-bomb type scenario [43]. As pointed out before, the main difficulty in mapping the toy model to the actual scenario lies in choosing a “correct” value for the absorption parameter  $\alpha$ . Our analysis has shown that the amplification factor of the confined scalar field with a single absorbing region depends linearly on the absorption parameter  $\alpha$  (see figure 4.6). This behaviour is observed in other similar models [2] and allows one to extrapolate the results of our simulations with  $\alpha = 10.0$  to ones with a lower absorption parameter. Using this, the  $\alpha \sim 1/M$  substitution yields sensible results, corroborating its use to obtain meaningful timescales of astrophysical systems.

Our main result, however, is the observation of superradiant instabilities triggered by the presence of moving disconnected bodies inside a cavity. This fact, hits at the possibility that superradiant amplification can occur in BH binaries and possibly lead to instabilities. Not only that, but the formation and growth of such field configurations can itself radiate gravitationally.

The simulations performed show that BHBs naturally excite lower energetic modes, making these systems perfect targets for future GW detectors aimed at detecting low frequency GW signals [32]. One of the main scientific objectives of such detectors is the placement of strict constraints in the mass of ultralight bosonic fields and, although massless scalars were considered, the confining cavity is usually taken as a robust mean of modelling the natural size of scalar clouds around BHs (see chapter 2 and [77]).

The confinement of the field may also arise due to density gradients in the interstellar medium [47, 78]. In this scenario, the pressure exerted on the cavity walls (the interstellar medium) can play a crucial role in the dynamics of larger astrophysical systems and shape their evolution. The details of such interaction, however, require a better knowledge of the nature of the scalar matter and, refrain further comments, we mentioned it here as a possible line of future work.

Our findings lead inevitably to more questions that can (and perhaps should) be tackled in the coming future. The most natural step to take further would be to generalize the model to a  $3+1$  model. At the expense of longer simulation times, the mathematical setup of our problem makes this a simple task. The mathematical formulation chosen also makes it very natural to extend the system to non-symmetric systems and thus, considering different size regions with possible distinct absorption parameters could be a step to model non-equal mass binary BH systems and other physical setups.

Another natural question relates to the modelling of the confinement of a massive field by a reflecting cavity. Although the results of chapter 2 point at the conclusion that cavities give, in fact, the correct physical picture relating massive fields around rotating BHs, the same cannot be said with such certainty about binaries systems enclosed in a cavity.

Removing the cavity, the model could also be used to study the scattering of fields by

the binary system. Numerically, this could simply be done by considering a large cavity and studying the behaviour of the field after a single reflection. In this scenario, it is also easy to consider a massive field. The study of the scattering problem could be directly compared with the field approach taken in [35], that can be mapped to our model when one considers the absorbing regions as point-like absorbers.

On the more experimental side, our study also shows what sort of physical setups may lead to observable superradiant instabilities. The connection of the model of this chapter with that of chapter 3 (see appendix D) makes it possible to devise experiments for the detection of binary superradiance and establish it, just like it was done for superradiance, as an observable physical phenomenon.



## Chapter 5

# Conclusions

The master thesis here concluded explored the subject of superradiance in generic asymmetric systems. The question of whether or not such systems are bound to superradiant scattering or instabilities, although postulated, was in no way known to occur explicitly. We undoubtedly settled this question with an affirmative answer – Asymmetric systems can scatter in a superradiant fashion. Furthermore, if enclosed in a cavity, such systems can develop instabilities that grow exponentially in time.

These statements were seen to be true already in chapter 3. There, the generalization of the model studied in [1] to the asymmetric case allowed us to reach a set of complementary results about the original model as well as show that in fact the asymmetry of such system does not strongly quench the instability rates. It also showed us that the two-fold symmetry of the model couples equal parity modes, leaving a clear signature in the interacting medium

The main motivation for our study, however, was the possibility of applying the results obtained by exploring such systems to astrophysical scenarios. This was mainly achieved through the model explored in chapter 4 where a clear connection could be made.

We showed for the first time that disconnected bodies with asymmetric geometry do not quench superradiant instabilities and that these can have relatively high amplification rates. In fact, bridging the model to BH systems, we postulate that such instabilities can compete with gravitational wave emission at some stages of the binary inspiral. This is bound to impact the evolution of such systems possibly leading to signatures in dynamical and statistical studies of BHBs.

We also showed that moving disconnected bodies inside a cavity naturally excite lower energetic modes of a surrounding field. In astrophysical context, this makes binary systems perfect targets for future GW detectors aimed at detecting low frequency GW signals [32]. This could not only allow a better understanding of how such systems are formed but as well the placement of strict constraints in the mass of ultralight bosonic fields.

On the earth based experimental side, both our models make it easy to devise experiments for the detection of binary superradiance and establish it, just like it was done for superradiance, as an observable and well established physical phenomenon.

---

# Bibliography

- [1] V. Cardoso, A. Coutant, M. Richartz, and S. Weinfurtner, *Phys. Rev. Lett.* **117**, 271101 (2016), [arXiv:1607.01378 \[gr-qc\]](#) .
- [2] V. Cardoso, R. Brito, and J. L. Rosa, *Phys. Rev. D* **91**, 124026 (2015), [arXiv:1505.05509 \[gr-qc\]](#) .
- [3] A. Einstein, *Sitzungsber. Preuss. Akad. Wiss. Berlin (Math. Phys. )* **1915**, 778 (1915), [Addendum: *Sitzungsber. Preuss. Akad. Wiss. Berlin (Math. Phys.)* 1915, 799–801 (1915)].
- [4] C. M. Will, *Living Rev. Rel.* **17**, 4 (2014), [arXiv:1403.7377 \[gr-qc\]](#) .
- [5] B. P. Abbott *et al.* (LIGO Scientific, Virgo), *Phys. Rev. Lett.* **116**, 061102 (2016), [arXiv:1602.03837 \[gr-qc\]](#) .
- [6] J. de Swart, G. Bertone, and J. van Dongen, *Nature Astron.* **1**, 0059 (2017), [arXiv:1703.00013 \[astro-ph.CO\]](#) .
- [7] F. Zwicky, *Helv. Phys. Acta* **6**, 110 (1933).
- [8] W. Thomson, Baron Kelvin, *Baltimore Lectures on Molecular Dynamics and the Wave Theory of Light*, Cambridge Library Collection - Physical Sciences (Cambridge University Press, 2010).
- [9] I. Newton, *Philosophiæ Naturalis Principia Mathematica* (England, 1687).
- [10] W. Thomson and P. G. Tait, *Treatise on Natural Philosophy*, 2nd ed., Cambridge Library Collection - Mathematics, Vol. 1 (Cambridge University Press, 2009).
- [11] E. Hubble and M. L. Humason, *Astrophys. J.* **74**, 43 (1931).
- [12] V. C. Rubin and W. K. Ford, Jr., *Astrophys. J.* **159**, 379 (1970).
- [13] V. C. Rubin, W. K. Ford, Jr., and N. Thonnard, *Astrophys. J. Lett.* **225**, L107 (1978).
- [14] C. Alcock *et al.* (MACHO), *Astrophys. J.* **542**, 281 (2000), [arXiv:astro-ph/0001272](#) .
- [15] A. A. Penzias and R. W. Wilson, *Astrophys. J.* **142**, 419 (1965).
- [16] P. J. E. Peebles, *Nature Astron.* **1**, 0057 (2017), [arXiv:1701.05837 \[astro-ph.CO\]](#) .

- [17] G. Hinshaw *et al.* (WMAP), *Astrophys. J. Suppl.* **208**, 19 (2013), [arXiv:1212.5226 \[astro-ph.CO\]](#) .
- [18] R. D. Peccei and H. R. Quinn, *Phys. Rev. D* **16**, 1791 (1977).
- [19] S. Weinberg, *Phys. Rev. Lett.* **40**, 223 (1978).
- [20] L. Hui, J. P. Ostriker, S. Tremaine, and E. Witten, *Phys. Rev. D* **95**, 043541 (2017), [arXiv:1610.08297 \[astro-ph.CO\]](#) .
- [21] D. H. Weinberg, J. S. Bullock, F. Governato, R. Kuzio de Naray, and A. H. G. Peter, *Proc. Nat. Acad. Sci.* **112**, 12249 (2015), [arXiv:1306.0913 \[astro-ph.CO\]](#) .
- [22] A. Del Popolo and M. Le Delliou, *Galaxies* **5**, 17 (2017), [arXiv:1606.07790 \[astro-ph.CO\]](#) .
- [23] W. Hu, R. Barkana, and A. Gruzinov, *Phys. Rev. Lett.* **85**, 1158 (2000), [arXiv:astro-ph/0003365](#) .
- [24] R. Brito, V. Cardoso, and P. Pani, *Lect. Notes Phys.* **906**, pp.1 (2015), [arXiv:1501.06570 \[gr-qc\]](#) .
- [25] R. Penrose and R. M. Floyd, *Nature* **229**, 177 (1971).
- [26] A. Arvanitaki and S. Dubovsky, *Phys. Rev. D* **83**, 044026 (2011), [arXiv:1004.3558 \[hep-th\]](#) .
- [27] A. Arvanitaki, S. Dimopoulos, S. Dubovsky, N. Kaloper, and J. March-Russell, *Phys. Rev. D* **81**, 123530 (2010), [arXiv:0905.4720 \[hep-th\]](#) .
- [28] F. Pretorius, *Phys. Rev. Lett.* **95**, 121101 (2005), [arXiv:gr-qc/0507014](#) .
- [29] F. Pretorius, (2007), [arXiv:0710.1338 \[gr-qc\]](#) .
- [30] B. P. Abbott *et al.* (LIGO Scientific, Virgo), *Phys. Rev. X* **9**, 031040 (2019), [arXiv:1811.12907 \[astro-ph.HE\]](#) .
- [31] P. Amaro-Seoane *et al.* (LISA), (2017), [arXiv:1702.00786 \[astro-ph.IM\]](#) .
- [32] M. Armano, H. Audley, *et al.*, *arXiv e-prints* , [arXiv:1903.08924](#) (2019), [arXiv:1903.08924 \[astro-ph.IM\]](#) .
- [33] M. Maggiore *et al.*, *JCAP* **03**, 050 (2020), [arXiv:1912.02622 \[astro-ph.CO\]](#) .
- [34] V. Cardoso and R. Vicente, *Phys. Rev. D* **100**, 084001 (2019), [arXiv:1906.10140 \[gr-qc\]](#) .
- [35] L. K. Wong, *Phys. Rev. D* **100**, 044051 (2019), [arXiv:1905.08543 \[hep-th\]](#) .
- [36] L. Bernard, V. Cardoso, T. Ikeda, and M. Zilhão, *Phys. Rev. D* **100**, 044002 (2019), [arXiv:1905.05204 \[gr-qc\]](#) .

- [37] W. H. Press and S. A. Teukolsky, *Nature* **238**, 211 (1972).
- [38] D. C. Ribeiro, M. Zilhão, and V. Cardoso, (2022), [arXiv:2201.13407 \[gr-qc\]](#) .
- [39] S. W. Hawking, in *1st Oxford Conference on Quantum Gravity* (1975).
- [40] Y. B. Zel'Dovich, *Soviet Journal of Experimental and Theoretical Physics* **35**, 1085 (1972).
- [41] J. D. Bekenstein, *Phys. Rev. D* **7**, 2333 (1973).
- [42] J. M. Bardeen, B. Carter, and S. W. Hawking, *Commun. Math. Phys.* **31**, 161 (1973).
- [43] V. Cardoso, O. J. C. Dias, J. P. S. Lemos, and S. Yoshida, *Phys. Rev. D* **70**, 044039 (2004), [Erratum: *Phys.Rev.D* 70, 049903 (2004)], [arXiv:hep-th/0404096](#) .
- [44] S. A. Teukolsky and W. H. Press, *Astrophys. J.* **193**, 443 (1974).
- [45] E. Berti, V. Cardoso, and M. Casals, *Phys. Rev. D* **73**, 024013 (2006), [Erratum: *Phys.Rev.D* 73, 109902 (2006)], [arXiv:gr-qc/0511111](#) .
- [46] V. Cardoso and O. J. C. Dias, *Phys. Rev. D* **70**, 084011 (2004), [arXiv:hep-th/0405006](#) .
- [47] R. Vicente, V. Cardoso, and M. Zilhão, *Mon. Not. Roy. Astron. Soc.* **489**, 5424 (2019), [arXiv:1905.06353 \[astro-ph.GA\]](#) .
- [48] S. D. Majumdar, *Phys. Rev.* **72**, 390 (1947).
- [49] A. Buonanno and T. Damour, *Phys. Rev. D* **62**, 064015 (2000), [arXiv:gr-qc/0001013](#) .
- [50] K. Alvi, *Phys. Rev. D* **61**, 124013 (2000), [arXiv:gr-qc/9912113](#) .
- [51] W. G. Unruh, *Phys. Rev. Lett.* **46**, 1351 (1981).
- [52] S. F. Freitas, (2017), [10.13140/RG.2.2.13908.86407](#).
- [53] M. Croub, G. M. Gibson, E. Toninelli, M. J. Padgett, E. M. Wright, and D. Faccio, *Nature Phys.* **16**, 1069 (2020), [arXiv:2005.03760 \[physics.class-ph\]](#) .
- [54] S. M. Carroll, (1997), [arXiv:gr-qc/9712019](#) .
- [55] M. Visser, *Class. Quant. Grav.* **15**, 1767 (1998), [arXiv:gr-qc/9712010](#) .
- [56] M. Visser, C. Barcelo, and S. Liberati, *Gen. Rel. Grav.* **34**, 1719 (2002), [arXiv:gr-qc/0111111](#) .
- [57] M. Delany and E. Bazley, *Applied Acoustics* **3**, 105 (1970).
- [58] J. Bezanson, A. Edelman, S. Karpinski, and V. B. Shah, *SIAM review* **59**, 65 (2017).

- [59] D. C. Ribeiro, “Zilindroa solver,” (2022).
- [60] C. Rackauckas and Q. Nie, *Journal of Open Research Software* **5** (2017).
- [61] T. Torres, S. Patrick, A. Coutant, M. Richartz, E. W. Tedford, and S. Weinfurter, *Nature Phys.* **13**, 833 (2017), [arXiv:1612.06180 \[gr-qc\]](#) .
- [62] M. C. Braidotti, R. Prizia, C. Maitland, F. Marino, A. Prain, I. Starshynov, N. Westerbergh, E. M. Wright, and D. Faccio, *Phys. Rev. Lett.* **128**, 013901 (2022), [arXiv:2109.02307 \[physics.optics\]](#) .
- [63] J. Van Bladel, *Proceedings of the IEEE* **64**, 301 (1976).
- [64] D. C. Ribeiro, “Black hole absorption solver,” (2021).
- [65] Y. B. Zel’Dovich, *Soviet Journal of Experimental and Theoretical Physics Letters* **14**, 180 (1971).
- [66] C. F. B. Macedo, P. Pani, V. Cardoso, and L. C. B. Crispino, *Astrophys. J.* **774**, 48 (2013), [arXiv:1302.2646 \[gr-qc\]](#) .
- [67] C. F. B. Macedo, L. C. S. Leite, E. S. Oliveira, S. R. Dolan, and L. C. B. Crispino, *Phys. Rev. D* **88**, 064033 (2013), [arXiv:1308.0018 \[gr-qc\]](#) .
- [68] T. Ikeda, L. Bernard, V. Cardoso, and M. Zilhão, *Phys. Rev. D* **103**, 024020 (2021), [arXiv:2010.00008 \[gr-qc\]](#) .
- [69] V. Cardoso, O. J. C. Dias, G. S. Hartnett, L. Lehner, and J. E. Santos, *JHEP* **04**, 183 (2014), [arXiv:1312.5323 \[hep-th\]](#) .
- [70] P. M. Chesler and D. A. Lowe, *Phys. Rev. Lett.* **122**, 181101 (2019), [arXiv:1801.09711 \[gr-qc\]](#) .
- [71] P. M. Chesler, *Phys. Rev. D* **105**, 024026 (2022), [arXiv:2109.06901 \[gr-qc\]](#) .
- [72] P. C. Peters and J. Mathews, *Physical Review* **131**, 435 (1963).
- [73] V. Cardoso, S. Chakrabarti, P. Pani, E. Berti, and L. Gualtieri, *Phys. Rev. Lett.* **107**, 241101 (2011), [arXiv:1109.6021 \[gr-qc\]](#) .
- [74] E. Barausse, V. Cardoso, and P. Pani, *Phys. Rev. D* **89**, 104059 (2014), [arXiv:1404.7149 \[gr-qc\]](#) .
- [75] L. Annulli, V. Cardoso, and R. Vicente, *Phys. Rev. D* **102**, 063022 (2020), [arXiv:2009.00012 \[gr-qc\]](#) .
- [76] J. D. Bekenstein and M. Schiffer, *Phys. Rev. D* **58**, 064014 (1998), [arXiv:gr-qc/9803033](#) .
- [77] L. Hui, D. Kabat, X. Li, L. Santoni, and S. S. C. Wong, *JCAP* **06**, 038 (2019), [arXiv:1904.12803 \[gr-qc\]](#) .

## BIBLIOGRAPHY

---

- [78] V. Cardoso, W.-D. Guo, C. F. B. Macedo, and P. Pani, *Mon. Not. Roy. Astron. Soc.* **503**, 563 (2021), arXiv:2009.07287 [gr-qc] .
- [79] “1. finite difference approximations,” in *Finite Difference Methods for Ordinary and Partial Differential Equations*, pp. 3–11, <https://epubs.siam.org/doi/pdf/10.1137/1.9780898717839.ch1> .



# Appendix A

## Mathematica Notebooks

Several of the numerical and analytical methods used in this work have been implemented in Mathematica notebooks which are publicly available [here](#). Here we give a brief description of their contents:

- **Superradiance in Lab.nb**  
Contains the code for the calculation of the cavity eigenfrequencies of the uniform cylinder model of chapter 3. The notebook reproduces as well the results of reference [1].
- **Asymmetric cylinder scattering.nb**  
Contains the matrix truncation calculations for the scattering amplitudes of waves off the asymmetric cylinder of chapter 3
- **KG Absorbing Cylinder.nb**  
Contains the code for the calculation of the cavity eigenfrequencies of the absorbing model of chapter 4.

---

## Appendix B

# Bessel and Hankel Functions

Bessel functions are defined as the solutions to the second order differential equation

$$\frac{d^2y}{dx^2} + \frac{1}{x} \frac{dy}{dx} + \left(1 - \frac{n^2}{x^2}\right) y = 0 \quad (\text{B.1})$$

where  $n$  is usually taken to be an integer or an half-integer. This equation arises naturally in many scenarios when solving problems with cylindrical symmetry (integer  $n$ ) or spherical symmetry (half-integer  $n$ ). The former played a crucial role in the main text results. We thus present here some important results regarding the solutions of equation (B.1) and their properties.

### B.1 Power series solution

The two linearly independent solutions to the Bessel equation are called Bessel functions of the first and second kind denoted by  $J_n(x)$  and  $Y_n(x)$ , respectively. The first kind solution is non-singular at the origin and can thus be defined in terms of a power series

$$y = \sum_{k=0}^{\infty} A_k x^{k+r} . \quad (\text{B.2})$$

The expansion is particularly useful when evaluating long wave limits of the scattering amplitudes (see chapter 3 and appendix D) and so we present here a brief derivation of the exact expansion.

Plugging (B.2) into the bessel equation (B.1), we find

$$\sum_{k=0}^{\infty} A_k [(k+r)^2 - n^2] x^{k+r-2} + \sum_{k=0}^{\infty} A_k x^{k+r} = 0 \quad (\text{B.3})$$

that can be simplified by joining equal powers of  $x$  to

$$A_0(r^2 - n^2) + A_1[(1+r)^2 - n^2]x + \sum_{k=2}^{\infty} [A_k((k+r)^2 - n^2) + A_{k-2}]x^{k+r-2} = 0 . \quad (\text{B.4})$$

The above expression gives us a recursion relation for the coefficients  $A_k$ . Explicitly we have

$$\begin{aligned} A_0(r^2 - n^2) &= 0 \\ A_1[(1+r)^2 - n^2] &= 0 \\ A_k[(k+r)^2 - n^2] &= -A_{k-2}. \end{aligned} \quad (\text{B.5})$$

The first equation implies that, for  $A_0 \neq 0$  one must have  $r = \pm n$ . Plugging this condition in the second equation implies that  $A_1 = 0$  and so, due to the recurrence relation of the last equation,  $A_k = 0$  for all odd values of  $k$ . On the contrary, the even mode coefficients can all be written in terms of the first coefficient  $A_0$  by using

$$A_k = \frac{-1}{k(2n+k)} A_{k-2}. \quad (\text{B.6})$$

If we let  $k = 2q$  the above recursion reads

$$\begin{aligned} A_{2q} &= \frac{-1}{2q(2n+2q)} A_{2(q-1)} \\ &= -\frac{1}{4} \frac{1}{q(n+q)} A_{2(q-1)} \\ &= \left(-\frac{1}{4}\right)^2 \frac{1}{q(q-1)(n+q)(n+q-1)} A_{2(q-2)} \\ &= \dots \\ &= \left(-\frac{1}{4}\right)^q \frac{n!}{q!(n+q)!} A_0. \end{aligned} \quad (\text{B.7})$$

Since  $A_0$  is a free parameter we can choose it to be  $A_0 = 1/(2^n n!)$  so that we obtain the power series form of the bessel function of the first kind

$$J_n(x) = \sum_{k=0}^{\infty} = \frac{(-1)^k}{k!(n+k)!} \left(\frac{x}{2}\right)^{2k+n} \quad (\text{B.8})$$

For  $x \ll 1$ , the  $n$ -th order function behaves as

$$J_n(x) \sim \frac{1}{n!} \left(\frac{x}{2}\right)^n. \quad (\text{B.9})$$

## B.2 Transformed Bessel equation

A rather useful form of the Bessel equation (B.1) is obtained by defining  $y = x^\alpha J_n(\beta x^\gamma)$ . Doing so, the governing equation reads

$$\frac{d^2 y}{dx^2} - \frac{(2\alpha - 1)}{x} \frac{dy}{dx} + \left( \beta^2 \gamma^2 x^{2(\gamma-1)} + \frac{\alpha^2 - n^2 \gamma^2}{x^2} \right) y = 0, \quad (\text{B.10})$$


---

where the solutions take now the form

$$y(x) = x^\alpha [AJ_n(\beta x^\gamma) + BY_n(\beta x^\gamma)] . \quad (\text{B.11})$$

The altered form of the Bessel equation often appears in physical problems. Namely, the radial field equation for the model of chapter 3 is of the form (B.10) with

$$\alpha = \frac{1}{2} , \quad \beta^2 = \omega^2 , \quad \gamma^2 = 1 , \quad n = m . \quad (\text{B.12})$$

giving us the solutions (3.23). Similarly, the radial field equation of chapter 4 has the altered form but with  $\beta$  given by

$$\beta^2 = \omega^2 + i\alpha(\omega - m\Omega) . \quad (\text{B.13})$$

### B.3 Hankel functions

In the scattering problems of chapter 3 and chapter 4, we wrote our solutions in terms of the hankel functions of the first and second kind,  $\phi_m^+$  and  $\phi_m^-$ , defined as

$$\phi_m^+(x) = J_m(x) + iY_m(x) \quad \phi_m^-(x) = J_m(x) - iY_m(x) . \quad (\text{B.14})$$

These linear combinations of the Bessel functions represent two new linearly independent solutions to the Bessel equation with a particular behaviour. Namely, for large argument  $x$  these behave as

$$\phi_m^+(x) \sim \sqrt{\frac{2}{\pi x}} \exp \left[ i \left( x - \frac{m\pi}{2} - \frac{\pi}{4} \right) \right] \quad (\text{B.15})$$

$$\phi_m^-(x) \sim \sqrt{\frac{2}{\pi x}} \exp \left[ -i \left( x - \frac{m\pi}{2} - \frac{\pi}{4} \right) \right] ,$$

physically translating into travelling wavelike solutions. The Bessel functions of the first and second kind have similar asymptotic behaviour. For large argument they behave as

$$J_m(x) \sim \sqrt{\frac{2}{\pi x}} \cos \left( x - \frac{m\pi}{2} - \frac{\pi}{4} \right) \quad (\text{B.16})$$

$$Y_m(x) \sim \sqrt{\frac{2}{\pi x}} \sin \left( x - \frac{m\pi}{2} - \frac{\pi}{4} \right) .$$

These asymptotic forms allow us to relate solutions written in terms of different Bessel functions. Namely, given the two solutions to the problem of chapter 3, equations (3.18) and (3.19), it is straightforward to show that the amplitudes of both solutions are related by (3.22).

## B.4 Recurrence relation

All Bessel functions satisfy the recurrence relation

$$\frac{dZ_m(x)}{dx} = \frac{1}{2} [Z_{m-1}(x) - Z_{m+1}(x)] , \quad (\text{B.17})$$

where  $Z_m$  denotes any Bessel or Hankel function. This expression was used in chapters [3](#) and [4](#).

## Appendix C

# Numerical Methods and Convergence

The numerical study of the models of chapter 3 and 4 resumes itself to solving the wave equation in distinct coordinate systems and with the appropriate boundary conditions. For both problems we resort to similar code that implements the Method of Lines. The `Zilindroa` code used to solve the model of chapter 3 is freely available at [59]. Similarly, the `BhAbs Solver` code used in chapter 4 can be downloaded at [64].

### C.1 The Method of Lines

The method of lines (MOL) is a very general algorithm for the solution of partial differential equations (PDE's). The idea behind the method is to discretize all but the time coordinate and by doing so, ending up with a set of coupled linear equations that can be easily solved by a ordinary differential equation (ODE) solver. Mathematically, the method is applied to a differential equation of the type

$$\frac{\partial f}{\partial t} = \mathcal{L}f \quad (\text{C.1})$$

where  $\mathcal{L}$  is some differential operator that we will make discrete. As an example, consider the one dimensional Heat equation written as

$$\frac{\partial f(x, t)}{\partial t} = \frac{\partial^2 f(x, t)}{\partial x^2}. \quad (\text{C.2})$$

To solve it numerically we begin by discretizing space and hence the function  $f$  as

$$\mathbf{x} = [x_1, x_2, \dots, x_N]^T \quad \mathbf{f} = [f(x_1), f(x_2), \dots, f(x_N)]^T. \quad (\text{C.3})$$

Given the above discretization, the RHS spatial derivative can be approximated by means of Finite differences (see [79] for a very pedagogical discussion of the topic). Consider for example the first order approximation of the second order spatial derivative

$$\left( \frac{d^2 f}{dx^2} \right)_{x=x_i} \approx \frac{f(x_{i-1}) - 2f(x_i) + f(x_{i+1}))}{h_x^2}, \quad (\text{C.4})$$

where  $h_x = x_{i+1} - x_i$  is the grid spacing. In terms of the discretization vectors this can be written as a matrix equation

$$\begin{bmatrix} \partial_x f(x_1) \\ \partial_x f(x_2) \\ \partial_x f(x_3) \\ \partial_x f(x_4) \\ \vdots \end{bmatrix} = \frac{1}{h_x^2} \begin{bmatrix} -2 & 1 & & & \\ 1 & -2 & 1 & & \\ & 1 & -2 & 1 & \\ & & 1 & -2 & 1 \\ & & & \ddots & \ddots \end{bmatrix} \begin{bmatrix} f(x_1) \\ f(x_2) \\ f(x_3) \\ f(x_4) \\ \vdots \end{bmatrix} \quad (C.5)$$

The matrix above is precisely the discretization matrix of the linear differential operator  $\partial_{xx}$ . We shall call it  $[D_{xx}]$ . Other linear operators can be defined in a similar way, allowing the discretization of any PDE. The heat equation can thus be written as

$$\partial_t \mathbf{f} = [D_{xx}] \mathbf{f}, \quad (C.6)$$

which is just a set of coupled ODE's and can thus be solved by a simple ODE solver.

The method can be extended to solve 2 dimensional problems. Take again the heat equation, this time in two dimensions

$$\frac{\partial u(x, y, t)}{\partial t} = \frac{\partial^2 u(x, y, t)}{\partial x^2} + \frac{\partial^2 u(x, y, t)}{\partial y^2} \quad (C.7)$$

In this scenario, instead of a vector, the function  $f$  is discretized as an  $N \times M$  matrix

$$f(x, y) = \begin{bmatrix} f(x_1, y_1) & f(x_1, y_2) & \cdots & f(x_1, y_N) \\ f(x_2, y_1) & f(x_2, y_2) & \cdots & f(x_2, y_N) \\ \vdots & \vdots & \ddots & \vdots \\ f(x_M, y_1) & f(x_M, y_2) & \cdots & f(x_M, y_N) \end{bmatrix} \quad (C.8)$$

The discretization of both differential operators is not so trivial in this case but luckily, if we know how to discretize one-dimensional operators, we can easily write the higher dimensional versions. This is done by transforming out function matrix into a vector

$$\begin{bmatrix} f(x_1, y_1) & f(x_1, y_2) & \cdots & f(x_1, y_N) \\ f(x_2, y_1) & f(x_2, y_2) & \cdots & f(x_2, y_N) \\ \vdots & \vdots & \ddots & \vdots \\ f(x_M, y_1) & f(x_M, y_2) & \cdots & f(x_M, y_N) \end{bmatrix} \longrightarrow \begin{bmatrix} f(x_1, y_1) \\ \vdots \\ f(x_M, y_1) \\ f(x_1, y_2) \\ \vdots \\ f(x_M, y_2) \\ \vdots \\ f(x_M, y_N) \end{bmatrix} \quad (C.9)$$

and constructing the 2 dimensional operators from the lower dimensional ones. For example,

the 2D counterpart of the  $[D_{xx}]$  operator is given by

$$D_{xx}^{2D} = \begin{bmatrix} D_{xx} & 0 & \cdots & 0 \\ 0 & D_{xx} & \cdots & 0 \\ \vdots & \vdots & \ddots & \vdots \\ 0 & 0 & \cdots & D_{xx} \end{bmatrix} = \mathbb{I}_{N \times N} \otimes D_{xx} \quad (\text{C.10})$$

Similarly, the operator that acts on the second variable can be written as:

$$D_{yy}^{2D} = D_{yy} \otimes \mathbb{I}_{M \times M} \quad (\text{C.11})$$

This is the generic procedure for creating higher dimensional operators from lower dimensional ones.

The above example considered the heat equation in cartesian coordinates since it makes the introduction of the method simple. We could, however, have considered other coordinate systems where the RHS operators would have to be discretized differently.

## C.2 The wave equation

The wave equation can similarly be solved by using the MOL. Generically, the wave equation reads

$$\frac{\partial^2 \psi}{\partial t^2} = \nabla^2 \psi \quad (\text{C.12})$$

where the  $\nabla$  operator depends on the coordinate system. This leads to different discretization scheme depending on the problem we try to solve. The above equation is, however, second order in time. We can turn it into a first order equation by writing

$$\frac{\partial \psi}{\partial t} = \pi, \quad (\text{C.13})$$

$$\frac{\partial \pi}{\partial t} = \nabla^2 \psi. \quad (\text{C.14})$$

The numerical study of the models presented in chapters 3 and 4 solve slightly altered versions of the above equation (see below). For the first model we used the `Zilindroa` numerical package while for the second one we used the `BhAbs` numerical package. Both codes are written in the Julia programming language and implement the method of lines with second-order accurate operators. The time integration is performed with a fourth order Runge-kutta scheme provided by the `DifferentialEquations.jl` Julia package [60].

### C.2.1 Impedance Cylinder Model

The `Zilindroa` code used to study the cylinder model of chapter 3 solve the set of equations

$$\frac{\partial \phi}{\partial t} = \pi, \quad (\text{C.15})$$

$$\frac{d\pi}{dt} = \frac{\partial^2 \phi}{\partial r^2} + \frac{1}{r^2} \frac{\partial^2 \phi}{\partial \varphi^2} + \frac{\phi}{4r^2}. \quad (\text{C.16})$$

on a uniform polar grid with the boundary condition

$$\frac{\partial \phi}{\partial t} = Z \left[ \frac{\partial \phi}{\partial r} - \frac{\phi}{2r} \right] - \Omega \frac{\partial \phi}{\partial \varphi}. \quad (\text{C.17})$$

at the cylinder's radius and a vanishing one  $\phi = 0$  at the cavity radius.

### C.2.2 Absorption model

The numerical study of the absorption model of chapter 4 was similarly integrated using the `BhAbs` numerical package. The code solves the set of equations

$$\frac{\partial \psi}{\partial t} = \pi, \quad (\text{C.18})$$

$$\frac{d\pi}{dt} = \nabla^2 \psi - \alpha(\mathbf{x}, t) (\pi + \Omega \partial_\varphi \psi) \quad (\text{C.19})$$

on a uniform Cartesian grid. This means that the two operators  $\nabla^2$  and  $\partial_\varphi$  are actually written as

$$\nabla^2 \psi = \frac{\partial^2 \psi}{\partial x^2} + \frac{\partial^2 \psi}{\partial y^2}, \quad (\text{C.20})$$

$$\partial_\varphi \psi = x \frac{\partial \psi}{\partial y} - y \frac{\partial \psi}{\partial x}. \quad (\text{C.21})$$

Unlike in the impedance cylinder model, here we only have one boundary condition to impose at the cavity radius  $\psi = 0$ .

### C.3 Convergence analysis

Solving the problem numerically, we expect our found solution to become better as we increase the simulation resolution. Namely, the finite difference methods employed for the simulations should approximate the continuum solution of the problem with an error that depends polynomially on the grid spacing  $h$ ,

$$f = f_h + Ch^n + \mathcal{O}(h^{n+1}), \quad (\text{C.22})$$

where  $n$  is the convergence order. Using the above expression we can define the  $Q$ -factor as

$$Q = \frac{f_{h_c} - f_{h_m}}{f_{h_m} - f_{h_f}} = \frac{(f - Ch_c^n) - (f - Ch_{h_m}^n)}{(f - Ch_{h_m}^n) - (f - Ch_{h_f}^n)} = \frac{h_c^n - h_m^n}{h_m^n - h_f^n} \quad (\text{C.23})$$

where  $h_c$ ,  $h_m$  and  $h_f$  refer to three distinct resolutions. The subscripts chosen stand respectively for coarse, medium and fine grid resolutions.

Since we use 2nd-order accurate operators, we expect to see 2nd order convergence. This can be easily tested by running the same configuration for three different resolutions and calculating the  $Q$ -factor. Both models presented in the main text were tested by running the same initial simulation for three distinct grid resolutions and evaluating the evolution of the energy content of the field inside the cavity.

Figure C.1 displays the convergence analysis for the impedance cylinder model of chapter 3. Specifically, it displays the convergence analysis the simulation displayed in the right panel of figure 3.11. The same simulation was run with several radial resolutions  $h_c = 0.14902$ ,  $h_m = 0.09524$  and  $h_f = 0.07436$ . The angular resolution was fixed to  $h_\varphi = 0.04947$ . The expected  $Q$ -factor for second order resolution with these values is of  $Q \simeq 3.71$ . The left panel displays refers to the energy content in the integration domain while the right one its growth rate. Both figures show consistency with second order convergence.

The same analysis was performed for the absorbing model of chapter 4. This is displayed in figure C.2. It displays the convergence analysis for the simulation presented in figure 4.11. The resolutions considered were  $h_c = 0.4013M$ ,  $h_m = 0.3008M$  and  $h_f = 0.24048M$ , giving an expected convergence  $Q$ -factor of  $Q \simeq 2.16$ . Since the integration grid is now Cartesian, we considered equal resolutions for the  $x$  and  $y$  coordinates. The plot shows agreement with second order convergence.

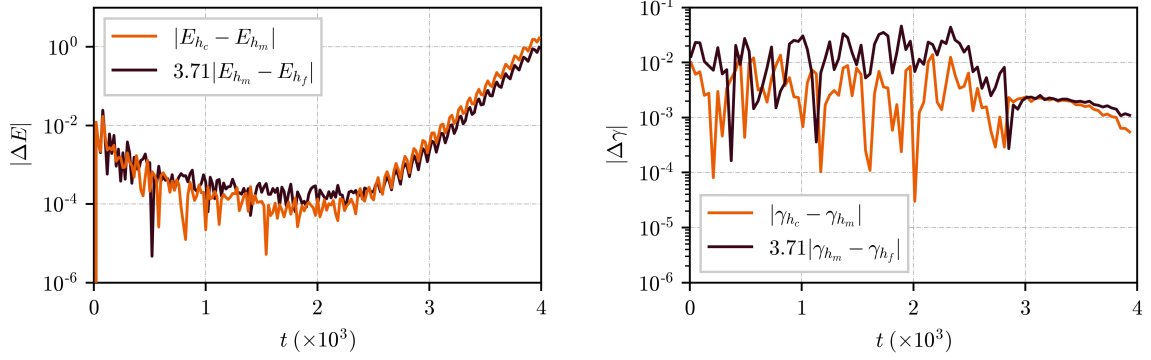


Figure C.1: Convergence analysis of the simulation shown in figure 3.11. The left plot displays analysis of the energy density inside the cavity according to expression (C.23). The right panel shows the same analysis for the energy growth rate averaged over  $\Delta t = 20$ . The multiplying factor corresponds to the  $Q$ -factor. The results are consistent with 2nd order convergence.

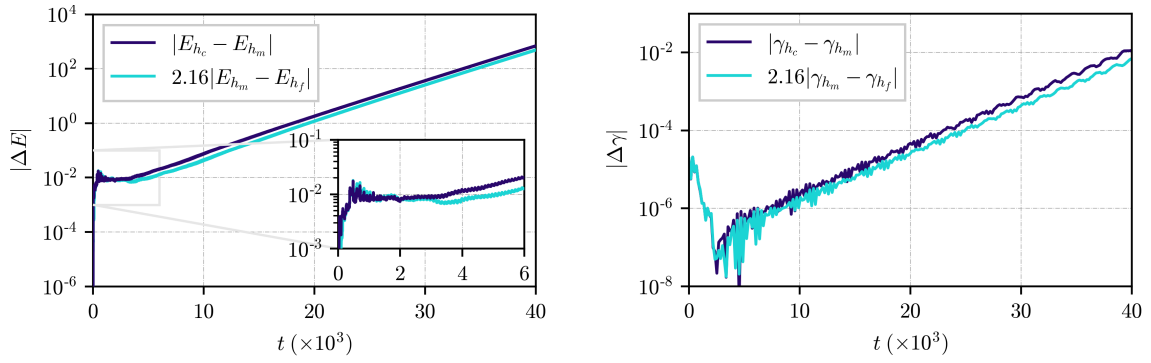


Figure C.2: Convergence analysis of the simulation shown in figure 4.11. The left plot displays analysis of the energy density inside the cavity according to expression (C.23). The right panel shows the same analysis for the energy growth rate. Results are consistent with 2nd order convergence.

## Appendix D

# The Toy Model Connection

Albeit similar in their construction, the connection between the two models considered is not straightforward. We can, nonetheless, bridge the gap between them by comparing their scattering spectra.

For the impedance cylinder model of chapter 3, the relative scattering amplitudes where given by

$$\frac{|\mathcal{A}_+|^2}{|\mathcal{A}_-|^2} = \left| \frac{(1 - 1/\sigma)\phi_m^- - iZ(\phi_m^-)'}{(1 - 1/\sigma)\phi_m^+ - iZ(\phi_m^+)'} \right|^2, \quad (\text{D.1})$$

where  $Z = Z_0/(\rho c)$ ,  $\sigma = \omega/m\Omega$  and the prime denotes differentiation with respect to  $y = \omega r/c$ . For the absorbing cylinder model of chapter 4, similarly, the amplification factors read

$$\left| \frac{\mathcal{A}_+}{\mathcal{A}_-} \right|^2 = \left| \frac{(\phi_m^-)(J_m^\alpha)' - (\phi_m^-)'(J_m^\alpha)}{(\phi_m^+)(J_m^\alpha)' - (\phi_m^+)'(J_m^\alpha)} \right|^2, \quad (\text{D.2})$$

where, unlike in (D.1), the prime denotes differentiation with respect to  $r$  and  $J_m^\alpha = J_m(\beta_\alpha r)$  with  $\beta_\alpha$  defined through

$$\beta_\alpha^2 = \omega^2 + i\alpha(\omega - m\Omega). \quad (\text{D.3})$$

The above expressions describe the scattering spectrum of the two models. From an experimental point of view then, if the two models display the same scattering amplitude for a given field frequency  $\omega$ , one cannot tell the difference between the two. With this approach, by comparing both expressions we see that the two models are equivalent as long as

$$\frac{Z}{\rho\omega} \left( \frac{\sigma}{\sigma - 1} \right) = -\frac{i}{\beta_\alpha} \frac{J_m^\alpha}{(J_m^\alpha)'}. \quad (\text{D.4})$$

The derivatives are to be taken with respect to the Bessel argument  $x = \beta_\alpha r$ .

The above expression allows the direct connection between the absorption model and the impedance one. For a model with a given  $\alpha$  we can immediately find the impedance  $Z$  of a cylinder that, for a given field frequency  $\omega$ , scatters waves in the same manner an absorbing region

One could also wish to make the opposite relation, i.e, given a cylinder with impedance  $Z$ , what would be the associated absorption parameter  $\alpha$ . The dependence on the Bessel

---

functions makes it impossible to write a closed form expression. We can, however, find a relatively expression for when  $x = \beta_\alpha r \ll 1$ . In this scenario, the RHS of equation (D.4) can be approximated as

$$\frac{J_m^\alpha}{(J_m^\alpha)'} \approx \frac{x}{m} + \frac{x^3}{2m^2(1+m)} + \mathcal{O}(x^4). \quad (\text{D.5})$$

Plugging this in the original equation, the relation now reads

$$\frac{Z}{\rho\omega} \left( \frac{\sigma}{\sigma-1} \right) = -\frac{i}{\beta_\alpha} \left[ \frac{\beta_\alpha R}{m} + \frac{\beta_\alpha^3 R^3}{2m^2(1+m)} \right]. \quad (\text{D.6})$$

Using the definition of  $\beta_\alpha$ , this can be reordered to read

$$\alpha = i\omega + \frac{2m^2(m+1)}{\omega R^3} \left[ \frac{Z}{\rho\omega} \left( \frac{\sigma}{\sigma-1} \right) + i\frac{R}{m} \right]. \quad (\text{D.7})$$

Although this is only an approximate expression, it shows how the two models can be connected in both directions.

# Appendix E

## Absorbing sphere inside cavity

The single absorbing region model considered in section 4.3 can be easily extended to the 3 dimensional scenario. This is done by considering a spherical region where a dissipative term is added to the KG equation and using a spherical coordinate system  $(r, \theta, \varphi)$ .

### E.1 Spherical wave equation

Outside the absorbing region, the field is governed by the massless KG equation  $\square\psi = 0$ . In spherical coordinates this equation reads explicitly

$$\frac{\partial^2\psi}{\partial t^2} = \frac{1}{r^2} \left( r^2 \frac{\partial\psi}{\partial r} \right) + \frac{1}{r^2 \sin\theta} \frac{\partial}{\partial\theta} \left( \sin\theta \frac{\partial\psi}{\partial\theta} \right) + \frac{1}{r^2 \sin^2\theta} \frac{\partial^2\psi}{\partial\varphi^2} . \quad (\text{E.1})$$

A set of independent solutions is easily found by considering the field ansatz

$$\psi = \frac{\phi(r) S_l^m(\theta)}{r} e^{-i\omega t + im\varphi} . \quad (\text{E.2})$$

Plugging this in the governing equation, it separates into an angular one for  $S_l^m(\theta)$

$$\frac{1}{\sin\theta} \frac{\partial}{\partial\theta} \left[ \sin\theta \frac{\partial S_l^m(\theta)}{\partial\theta} \right] + \left[ \mathcal{A}_{lm} - \frac{m^2}{\sin^2\theta} \right] S_l^m(\theta) = 0 , \quad (\text{E.3})$$

and a radial one for  $\phi(r)$

$$\frac{\partial^2\phi}{\partial r^2} + \left[ \omega^2 - \frac{\mathcal{A}_{lm}}{r^2} \right] \phi = 0 . \quad (\text{E.4})$$

The separation constant  $\mathcal{A}_{lm}$  is obtained by solving the angular equation with appropriate boundary conditions. It has the value  $\mathcal{A}_{lm} = l(l+1)$ , where  $l$  is some positive integer that satisfies  $l \geq |m|$ . The solutions to the angular equation is obtained by noting that the variable transformation  $t = \cos\theta$  turns the angular equation into the Legendre equation, whose solutions are the associated Legendre polynomials  $P_l^m(\cos\theta)$ .

The solutions to the radial equation can also be written down easily by noting that

equation (E.4) has the form of the altered Bessel equation (B.10) with

$$\alpha = \frac{1}{2} \quad , \quad \beta^2 = \omega^2 \quad , \quad \gamma^2 = 1 \quad , \quad n = \left( l + \frac{1}{2} \right) . \quad (\text{E.5})$$

The solutions to the radial equation  $\phi(r)$  take then the form

$$\phi(r) = \sqrt{r} [AJ_{l+1/2}(\omega r) + BY_{l+1/2}(\omega r)] . \quad (\text{E.6})$$

Where  $J_{l+1/2}$  ,  $Y_{l+1/2}$  represent the Bessel functions of the first and second kind, respectively, of order  $l + 1/2$ .

In spherically symmetric problems, it is common practice to use the spherical Bessel functions  $\mathcal{J}_l$  and  $\mathcal{Y}_l$  defined as

$$\mathcal{J}_l(\omega r) = \frac{J_{l+1/2}(\omega r)}{\sqrt{r}} \quad \text{and} \quad \mathcal{Y}_l(\omega r) = \frac{Y_{l+1/2}(\omega r)}{\sqrt{r}} , \quad (\text{E.7})$$

respectively. In terms of these new functions, the field  $\psi$  has the general solution

$$\psi(t, r, \theta, \varphi) = [A\mathcal{J}_l(\omega r) + B\mathcal{Y}_l(\omega r)] S_l^m(\theta) e^{-i\omega t + im\varphi} . \quad (\text{E.8})$$

## E.2 Adding dissipation

Inside the rotating absorbing region, the KG equation takes the form

$$(\square - \mu^2)\Psi = \alpha \left[ \frac{\partial \Psi}{\partial t} + \Omega \frac{\partial \Psi}{\partial \phi} \right] , \quad (\text{E.9})$$

where  $\alpha$  is the absorption parameters and  $\Omega$  the angular velocity of the sphere. By the same separation of variables procedure, the radial equation reads now

$$\frac{\partial^2 \phi}{\partial r^2} + \left[ \omega^2 + i\alpha(\omega - m\Omega) - \frac{\mathcal{A}_{lm}}{r^2} \right] \phi = 0 . \quad (\text{E.10})$$

The general solution of the field  $\psi$  in this region is then easily seen to be

$$\psi(t, r, \theta, \varphi) = [A\mathcal{J}_l(\beta_\alpha r) + B\mathcal{Y}_l(\beta_\alpha r)] S_l^m(\theta) e^{-i\omega t + im\varphi} , \quad (\text{E.11})$$

with  $\beta_\alpha^2 = \omega^2 + i\alpha(\omega - m\Omega)$ . The whole domain solution can thus be written as

$$\psi_{m,l}(r) = \begin{cases} [A\mathcal{J}_l(\beta_\alpha r) + B\mathcal{Y}_l(\beta_\alpha r)] S_l^m(\theta) e^{-i\omega t + im\varphi} , & \text{for } 0 \leq r \leq R_a \\ [C\mathcal{J}_l(\beta_0 r) + D\mathcal{Y}_l(\beta_0 r)] S_l^m(\theta) e^{-i\omega t + im\varphi} , & \text{for } R_a < r \leq R_c \end{cases} . \quad (\text{E.12})$$

The above expression for the field solution is entirely analogous to the one found in chapter 4 for the cylindrical case. The main difference comes from the existence of a new integer  $l$  and the angular function  $S_l^m(\theta)$ . This, however, does not change the procedure by which one

obtains the eigenvalues of a cavity nor the scattering amplitudes associated with a reflected wave.

Like before then, the general solution must be regular at the origin, be continuously differentiable on the whole domain, and vanish at the cavity radius. From the first constraint, we immediately have that  $B = 0$  since the spherical Bessel function of the second kind  $\mathcal{Y}_l$  blows up at the origin. The last constrain forces the field to take a particular set of natural frequencies.

### E.3 Cavity eigenfrequencies

The procedure to find these frequencies is exactly the same as before and we thus obtain the eigenvalue equation

$$G_{l,m}(\omega) = 0. \quad (\text{E.13})$$

with  $G_{l,m}(\omega)$  defined as

$$G_{l,m}(\omega) = \frac{\mathcal{J}_l(\beta_0 R_a)}{\mathcal{J}_l(\beta_\alpha R_a)} + \left(\frac{D}{C}\right) \frac{\mathcal{Y}_l(\beta_0 R_a)}{\mathcal{Y}_l(\beta_\alpha R_a)} - \frac{\mathcal{J}'_l(\beta_0 R_a)}{\mathcal{J}'_l(\beta_\alpha R_a)} - \left(\frac{D}{C}\right) \frac{\mathcal{Y}'_l(\beta_0 R_a)}{\mathcal{Y}'_l(\beta_\alpha R_a)} \quad (\text{E.14})$$

where  $(D/C)$  is

$$\frac{D}{C} = -\frac{\mathcal{J}_l(\beta_0 R_c)}{\mathcal{Y}_l(\beta_0 R_c)}. \quad (\text{E.15})$$

and the primes denote derivative with respect to the radial coordinate  $r$ . Solving the above equation gives us the allowed frequencies of the field for a given set of parameters  $(R_a, R_c, \Omega, \alpha, m)$ .

### E.4 Scattering Problem

Removing the boundary condition at the cavity radius, one can also study the scattering of waves off the rotating sphere. This amounts to looking at solutions that behave

$$\psi(r \rightarrow \infty) \sim \frac{\mathcal{A}_+ e^{i\omega r} + \mathcal{A}_- e^{-i\omega r}}{r}, \quad (\text{E.16})$$

This is easily seen by taking the limit of the radial equation (E.4) when  $r$  goes to infinity. The solutions with this behaviour are the spherical hankel functions of the first and second kind, defined as respectively as

$$\mathcal{H}_l^+ = \mathcal{J}_l + i\mathcal{Y}_l \quad \text{and} \quad \mathcal{H}_l^- = \mathcal{J}_l - i\mathcal{Y}_l. \quad (\text{E.17})$$

These have the desired wave-like behaviour at spatial infinity. Imposing continuity at the sphere's surface we can relate the amplitude of the incoming and outgoing wave like we did

for the model of chapter 4

$$\left| \frac{\mathcal{A}_+}{\mathcal{A}_-} \right|^2 = \left| \frac{(\mathcal{H}_l^-)(\mathcal{J}_l^\alpha)' - (\mathcal{H}_l^-)'(\mathcal{J}_l^\alpha)}{(\mathcal{H}_l^+)(\mathcal{J}_l^\alpha)' - (\mathcal{H}_l^+)'(\mathcal{J}_l^\alpha)} \right|^2, \quad (\text{E.18})$$

where primes stand for derivative with respect to the radial coordinate and the functions  $\mathcal{J}_l^\alpha = \mathcal{J}_l(\beta_\alpha r)$  and  $\mathcal{H}_l^\pm = \mathcal{H}_l^\pm(\omega r)$  are evaluated at the boundary radius  $R_a$ .

Comparing the above equation with the corresponding lower dimensional one, equation (3.36), we see the clear similarities. In fact, writing the above expression in terms of the usual Bessel and Hankel functions (see appendix B) it reads

$$\left| \frac{\mathcal{A}_+}{\mathcal{A}_-} \right|^2 = \left| \frac{(\phi_{l+1/2}^-)(J_{l+1/2}^\alpha)' - (\phi_{l+1/2}^-)'(J_{l+1/2}^\alpha)}{(\phi_{l+1/2}^+)(J_{l+1/2}^\alpha)' - (\phi_{l+1/2}^+)'(J_{l+1/2}^\alpha)} \right|^2. \quad (\text{E.19})$$

The only difference from the lower dimensional expression is the replacement of the Bessel function order  $m \rightarrow l + 1/2$ . Note that this substitution is not to be made to the argument of the Bessel function  $J_{l+1/2}^\alpha$ .

The above expression makes it clear that the superradiant condition  $\omega < m\Omega$  for the existence of superradiance comes solely from the parameter  $\beta_\alpha$  in the argument of the bessel functions. It is also evident that, like in the lower dimensional model, all  $(l, m)$  modes are decoupled.

Figure 4.2 displays the amplification factor  $\mathcal{A}_{\omega ml} = |\mathcal{A}_+/\mathcal{A}_-|^2 - 1$  in terms of the parameter  $\varpi = \omega/m\Omega$  for two  $l = m$  modes and several rotation speeds. For all frequencies below the superradiant condition ( $\varpi < 1$ ) this amplification factor is positive. The scattering amplitudes display not only the same functional behaviour on the field frequency but also the same magnitudes, corroborating the idea that nothing intrinsic exists about lower dimensional scattering problems.

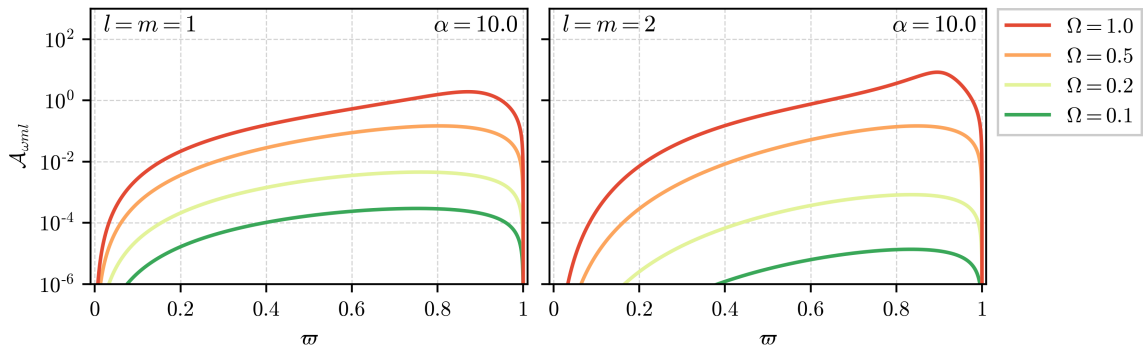


Figure E.1: Amplification factor  $\mathcal{A}_{\omega ml} = |\mathcal{A}_+/\mathcal{A}_-|^2 - 1$  for the absorbing sphere for  $l = m = 1$  (left plot) and  $l = m = 2$  (right plot), absorption parameter  $\alpha = 10.0$  and several rotation speeds. The curves are presented in terms of the frequency parameter  $\varpi = \omega/m\Omega$ . Compare with the 2D equivalent results in figure 4.2.

